TERRESTRIAL LASER SCANNING (TLS) OBSERVATIONS

OF EREBUS VOLCANO, ANTARCTICA:

INSIGHTS INTO THE NEAR-SURFACE MAGMATIC SYSTEM

by

Laura K Z Jones

Submitted in Partial Fulfillment

of the Requirements for the Degree of

Master of Science in Geology

New Mexico Institute of Mining and Technology

Socorro, New Mexico

December, 2013

ABSTRACT

A Terrestrial Laser Scanner (TLS) was used to image the Main Crater at Erebus volcano on Ross Island, Antarctica in December 2008, 2009 and 2010. The primary objective of the study was to map the active lava lake and to observe changes in the lake surface and the associated deformation within the Inner Crater. The single and continuous high-resolution TLS scans (coupled with a pulse generator) offer a unique view into both the short-term and long-term evolutions of the Erebus magmatic system.

The analysis of the TLS data revealed not only variations in the location, size and elevation of the lava lake from year-to-year but also minute-scale cyclic oscillations in lake level. Approximately 8 and 13-minute cycles were observed in 2009 and 2010, respectively, during which the lava lake surface would rise and fall 0.5-1.5 meters. These cycles remained generally constant during the entirety of the scans, except for an eruption and 2 degassing events during the 2010 scans. The oscillatory behavior seen in the lake level is consistent with viscosity-driven segmental flow which results in the episodic flux of volatile-rich magma into the lava lake. We also suggest that pressurization plays a large role in the overall stability of the system, sustaining the steady-state dynamics of the lava lake through decades of documented Strombolian eruptions.

The entire Inner Crater was scanned in 2010 and when combined with a 2001 Airborne Laser Scanner (ALS) survey provided measurements of ground surface deformation within the Erebus summit crater. Subsidence of between 6-40m was recorded with the largest subsidence observed along the Inner Crater walls and in the "active zones" (i.e. the lava lake and active vents) on the Inner Crater floor – equating to a net volumetric change of -875,200m^3 within the Main Crater. The observed pattern of subsidence is consistent with the deflation of 2 distinct magma bodies: one on the NE side of the Inner Crater (below the lava lake) and one on the SW side of the Inner Crater (below the "Werner" vent system). The underlying mechanism responsible for the depressurization and subsequent deflation of the near-surface magma system is proposed to be a decrease in magma flux from the deep reservoir.

TABLE OF CONTENTS

LIST OF FIGURES

LIST OF TABLES

CHAPTER 1 – INTRODUCTION

Volcanic activity is considered to be the surface expression of magma flow within the crust and consists of a wide-range of well-studied phenomena, from ground deformation and gas emissions to lava flows and explosive eruptions (e.g., *Hon et al.,* 1994; *Puglisi et al.,* 2001*; Oppenheimer and Kyle*, 2008; *Dibble et al.*, 2008). The style of volcanic activity is chiefly controlled by the fluid dynamics of magma ascent within the volcanic plumbing system – largely influenced by conduit geometry, magma rheology, crystal and volatile content, bubble growth and nucleation and degassing (*Carrigan*, 2000; *Gonnermann and Manga*, 2007; *Molina et al.*, 2012). Unfortunately, since direct observations of magma flow dynamics (and the processes that govern them) are difficult, most volcanoes are monitored primarily by the measurement of the results of magma flow, i.e. volcanic activity (*Gilbert and Lane*, 2008). In order to fully recognize and predict volcanic behavior, it then becomes critical to understand the connection between these surface manifestations and their underlying source. This study aims to directly measure the dynamics of magma flow through the observation of an active lava lake, allowing for the direct comparison between flow dynamics and surface signals.

Lava lakes are volcanic features that generally occur at basaltic volcanoes and are characterized as being either "inactive" or "active" (*Swanson et al.*, 1972; *Harris et al.*,

1999). Inactive lava lakes are very common, generally created through the ponding of lava flows and not connected to a magmatic system at depth. Conversely, active lava lakes are rare and are believed to represent the exposed top of shallow convecting magmatic systems (*Tilling*, 1987; *Tazieff*, 1994). They are fed by buoyant volatile-rich magma rising up the conduit from larger deeper magma chambers and then, after degassing and cooling, sinking under gravity back down the conduit. Lava lakes are considered windows into the lower (unseen) magmatic system and are able to offer unprecedented views into the shallow fluid dynamics of a volcano.

Long-lived, persistent lava lakes are even rarer and exist at very few volcanoes – most notably Nyiragongo (Democratic Republic of Congo), Erta 'Ale (Ethiopia), and Erebus volcano (Ross Island, Antarctica) (*Harris et al.*, 1999). In recent years a lava lake has also been present in Halemaumau crater at Kilauea volcano in Hawaii (*Carbone et al.*, 2013; *Edmonds et al.*, 2013). Steady, well-developed magma flow between the lava lake, conduit, and reservoir are necessary to insure the longevity of the lava lake (*Tazieff*, 1994; *Oppenheimer and Francis*, 1998; *Harris et al.*, 2005). This stability is due to convection within the conduit which is most likely driven and sustained by density contrasts that result from degassing and cooling at the lava lake surface, whereby dense cool degassed magma sinks through the conduit and buoyant hot volatile-rich magma rises to replace it (*Huppert and Hallworth,* 2007). This convection allows the lava lake to remain molten and the gas, thermal, and mass fluxes to be sustained over tens to hundreds of years (*Francis et al.*, 1993; *Oppenheimer et al.*, 2004; *Harris et al.*, 2005).

This paper focuses on the research made over 3 field seasons in the Austral summers of 2008, 2009 and 2010 using a Terrestrial Laser Scanner (TLS) to survey the

Main Crater of Erebus volcano on Ross Island, Antarctica. The primary objective of the

study was to image and map the active lava lake as well as to remotely observe the

continuous changes in the lake surface and the associated deformation within the Inner

Crater. The single and continuous high-resolution TLS scans coupled with GPS and

Airborne Laser Scanner (ALS) data from 2001 (*Csatho et al.,* 2008) offer a unique view

into both the short-term and long-term evolution of the Erebus magmatic system.

CHAPTER 2 – BACKGROUND

"Erebus not only commands a view of incomparable grandeur and interest, but is in itself one of the fairest and most majestic sights that Earth can show" (Shackleton, 1909).

Erebus is a large (~2000 km^3) alkaline stratovolcano located on Ross Island, Antarctica (77°32' S, 167°10' E), with a summit elevation of 3,794m (*Esser et al.*, 2004). Ross Island is also host to two extinct basanite volcanoes, Mount Bird (3262 m, ~470 km^3) and Mount Terror (3262 m, ~1700 km^3), which flank Erebus to the north-northwest and east, respectively (Figure 1; *Kyle et al.*; 1992). ^{40}Ar/^{39}Ar dating has estimated that over the last ~4 Ma, greater than 4500 km^3 of volcanic material has been erupted on Ross Island (*Esser et al.*, 2004). This extensive volcanism can be attributed to the crustal thinning and extensional faulting associated with intercontinental rifting of West Antarctica. Ross Island is located above 19-27 km thick continental crust at the southernmost end of the Terror Rift, in the western margin of the West Antarctic Rift System (*Finotello et al.*, 2011). Seismic studies (*Watson et al.*, 2006) also show a significant thermal anomaly beneath Ross Island, consistent with claims of a hot spot or mantle plume directly underneath Erebus volcano (*Kyle et al.*, 1992).

The summit region of Erebus volcano (> 3200m) is a plateau nearly 4 km in diameter, representing the remnants of two episodes of caldera collapse that occurred between 80-24 ka and 25-11ka which was then subsequently filled with younger lava (*Harpel et al.,* 2004; *Kelly et al.,* 2008a). Currently, this summit plateau also contains two craters: the active Main Crater (~550m in diameter) and the inactive (though actively geothermal) Side Crater (~250m in diameter) (*Csatho et al.*, 2008). The Inner Crater (lying within the Main Crater) plays host to the persistently active phonolite lava lake as well as many fumarolic vents. Several studies have provided evidence that the phonolite lava is a 25% residual melt resulting from the fractional crystallization of a mantle-derived parental basanite magma (e.g., *Kyle et al.*, 1992; *Sims et al.*, 2008; *Kelly et al.*, 2008b).
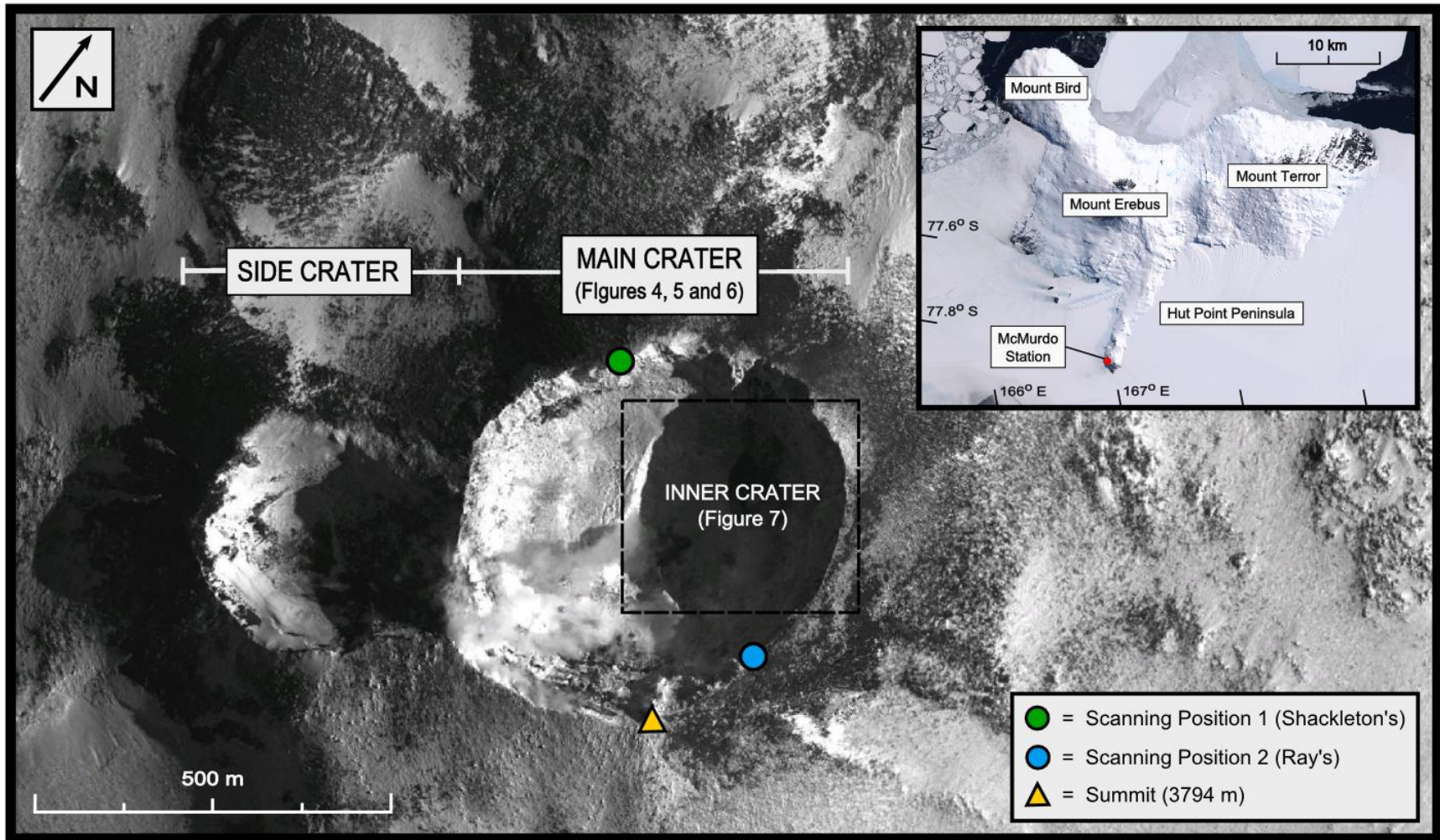
Figure 1 – Map of the Erebus summit cone (orthorectified pan sharpened Quickbird image; from the Polar Geospatial Center) showing the locations of the Main, Inner and Side Craters as well as the terrestrial laser scanning positions. Inset is a map of Ross Island (LIMA - Landsat Image Mosaic of Antarctica; NASA Landsat Program, 1999) showing the location of Mount Erebus, its flank volcanoes (Mount Terror and Bird), Hut Point Peninsula and McMurdo Station.

The geochemistry of this unique anorthoclase-bearing phonolite lava has remained remarkably stable (both chemically and isotopically) since systematic observations began in the 1970s (*Giggenbach et al.*, 1973; *Kelly et al.*, 2008b; *Sims et al.*, 2008). This long-term stability is another distinctive characteristic of the Erebus volcanic system that has been documented in several other studies, including: the continuous and geochemically monotonous plume of gases and aerosols emitted from the lava lake (*Zreda-Gostynska et al.*, 1997; *Oppenheimer and Kyle*, 2008; *Oppenheimer et al.*, 2011), the steady 15±8 MW radiant heat flux from the lava lake (as observed between 2001 and 2006 by satellite infrared measurements; *Wright and Pilger*, 2008) and the consistency of the very long period (VLP) signals from year-to-year and throughout hundreds of eruptions (*Aster et al.*, 2003). The only perturbations to the system are short-term and are created by intermittent Strombolian eruptions (*Gerst et al.*, 2013) that are capable of completely emptying the lava lake (*Dibble et al.*, 2008; *Oppenheimer et al.*, 2009). *Aster et al.* (2013) suggests that the stability of the VLP signals, the persistence and longevity of the lava lake and the rapid refilling of the lake after large eruptions are evidence for a near-summit magmatic system. Recent active source seismic studies have provided evidence of a large shallow magma chamber approximately 500m NW of the Inner Crater and 500m below the topographic surface, as well as propose a highly complex near-summit conduit system consisting of multiple side lobes, multiple surface threads, constrictions, highly inclined elements and fracture interconnections (*Chaput et al.*, 2012; *Zandomeneghi et al.*, 2013) .

The volcanic activity on Erebus has been extensively monitored since the early 1980s; however, over the past 25 years only two geodetic surveys have been performed

to monitor ground deformation. The first survey recorded measurements annually from December 1980 to December 1985 using precise triangulation, trilateration and tilt-leveling surveys (*Otway et al.*, 1994). The observed deformation appeared to be relatively minor with a total of 50±20 mm of extension over 5 years and occurred in 2 pulses, one in 1982 and the other in 1984. This deformation was localized around the Main Crater and occurred along an axis oriented 139°, perpendicular to a linear alignment of major faults, fumaroles, collapse features, and craters interpreted to be the surface expression of an underlying rift system. In this same study, a separate experimental survey model of the Inner Crater floor was created which indicated ~90-180 mm of subsidence in 1983 (*Otway et al.,* 1994). The second and more recent ground deformation survey was performed from 2002-2006 using a continuous GPS measurements. The only significant deformation, which was observed at several stations, was 10-20 mm of annual variation in the vertical. These measurements of ground deformation provide evidence for underlying fluid motion and are consistent with a shallow magma chamber beneath Erebus (*Murray et al.,* 2006). However, in order to more fully understand the shallow fluid dynamics on Erebus we performed repeated TLS scans of the Main Crater that allowed us to observe meter to centimeter-scale changes in the active Inner Crater floor and lava lake.

In addition to measuring ground deformation, monitoring changes associated with the lava lake provides further insight into the inner fluid dynamics of the volcano. Every December since 2004, thermal imagery of the lava lake and FTIR spectroscopy of gas emissions have been continuously and synchronously recorded (*Calkins et al.*, 2008; *Oppenheimer et al.,* 2008; *Sweeney et al.*, 2008; *Oppenheimer et al.,* 2009; 2011). In

2004, image-matching software was also used on the thermal images in order to estimate the rates of surface motion by following moving cracks across the lava lake surface (*Calkins et al.*, 2008). The analysis of these surface velocities combined with the gas and thermal data revealed short-term cycles with corresponding modal periods of between 8 and 18 minutes (*Oppenheimer et al.,* 2009; *Clive Oppenheimer*, *pers. comm.*). These cycles consisted of two distinctive end-members – (1) low surface velocity, low radiant heat flux, low SO_2/CO_2, H_2O, HCl and HF; (2) high surface velocity, high radiant heat flux, high SO_2/CO_2, H_2O, HCl and HF. *Oppenheimer et al.* (2009) interpreted this observed cyclic behavior to be the manifestation of a flow instability that developed due to bi-directional core-annular magma flow in the conduit.

CHAPTER 3 – TLS DATA COLLECTION AND PROCESSING

Terrestrial Laser Scanning (TLS), based on time-of-flight *li*ght *d*etection *a*nd *r*anging (lidar) technology, is a rapidly evolving technique that has the ability to offer unprecedented views into complex geologic systems. Current TLS systems are capable of imaging meter to kilometer-scale areas with centimeter to sub-centimeter precision. Today, high resolution TLS surveys are used in a wide range of geologic investigations, from landslide hazard assessment (e.g., *Jaboyedoff et al.*, 2010; *Salvini et al.,* 2013) to the detailed mapping of outcrops and fault scarps (e.g., *Jones et al.*, 2009; *Hodgetts*, 2013). Furthermore, repeat TLS surveys allow for the measurement of surface changes over time in order to understand currently active processes, including soil and cliff erosion (e.g., *Perroy et al.,*2010; *Young et al.,*2010), post-seismic slip (e.g., *McCaffrey et al.,* 2009), mass and ice flow (e.g., *Avian et al.,* 2009; *Finnegan et al.,* 2010), and volcanic deformation (e.g., *Pesci et al.,* 2008; *Favalli et al.,* 2010). This paper describes the use of TLS measurements to monitor volcanic deformation at time-scales ranging from minutes to decades.

3.1. Instrumentation and Data Collection

TLS surveys of the Main Crater on Erebus Volcano were acquired from 2008-2010 using an Optech ILRIS-3D ER (Extended Range) lidar. This instrument uses a 1535 nm wavelength (near infrared) laser and has a sampling frequency of 2.5-3.5 kHz (Optech, 2009). The ILRIS-3D ER has a 40° field of view in both the horizontal and vertical plane with a scanning range of 3 to 1700 m. For this survey, the ILRIS-3D was also equipped with a pan-tilt base, allowing it to have a scanning field of 360° in the horizontal and 90° in the vertical. The data recorded for each point by the scanner consisted of a Cartesian x, y, and z coordinate relative to the scanner's bolt hole reference point; normalized (0-255) backscatter intensity; and time (in seconds) since the scanner was powered on. For the lava lake scans, in order to achieve an accurate time series, a pulse generator was used to apply a relative time stamp onto each laser shot. Furthermore, the ILRIS-3D ER can be programmed to collect either the first or last reflection of the laser pulse. For these surveys, the last reflected pulse was collected in order to minimize the number of returns recorded from the persistent gas and aerosol plume.

The nominal one standard deviation range accuracy of the ILRIS-3D ER is 7mm at 100m (Optech, 2009). In addition, other factors that cannot be easily controlled contributed significantly to the total measurement error. One such significant factor is the error associated with the laser beam width, which has a linear relationship to the scanning distance (Eq. 1); the greater the beam diameter, the higher the maximum error.

$$D_f = x \cdot \tan \theta + D_i \qquad\qquad (1)$$

where D_i and D_f are the initial and final beam diameters, respectively (D_i = 1.2 cm for the ILRIS-3D), x is the scanning distance (in the same units as D) and θ is the beam divergence angle (0.00974° for the ILRIS-3D) (*Petrie and Toth*, 2008; *Abellán et al.*, 2011). The actual position of the measured reflection can exist anywhere within the beam, meaning that the actual angular position of the measurement may be biased by up to half of the beam diameter (*Pesci et al.*, 2011). This error is usually taken into account when reporting the spatial resolution of the instrument – which has been shown by several authors to not only depend on the chosen sampling step but also on the laser beam width (*Lichti and Jamtsho*, 2006; *Zhu et al.*, 2008; *Pesci et al.*, 2011). This resolution measurement can aid in selecting the most appropriate sampling step (one that is at least two-thirds the size of the beam) and minimize oversampling.

Another significant factor to the total measurement error on Erebus is the inconsistent presence of volcanic plume gases within the scanning window. The volcanic plume rises off of the degassing lava lake (sometimes filling the entire crater) and consists of varying proportions of gaseous H_2O, CO_2, CO, SO_2, HF, HCl and OCS; small particles of volcanic ash (glass and minerals); and liquid water and ice crystals, which develop as the plume rises and cools in the cold ambient Antarctic air (*Oppenheimer and Kyle,* 2008; *Oppenheimer et al.,* 2009). All of these characteristics have an effect on measurement error, such as scattering, beam reflection (off of silicate particles and ice crystals), refraction (as the beam passes through different temperature/density layer) and absorption (in liquid water).

Other factors that may also contribute to the uncertainty of the TLS data are pointing error (e.g., the vibration of the scanner, causing repeat shots to strike at slightly

different positions on the target area; *Boehler et al., 2003*), the reflectivity of the various materials being imaged (*Boehler et al., 2003*) and weather (particularly the wind – scans were not typically performed in strong persistent winds due to the presence of blowing dust and ice within the scanning window). Apart from the beam diameter, the other sources of error are difficult to quantify. Therefore we assessed the cumulative impacts of these errors (the overall accuracy of our measurements) through the examination the distribution of repeat measurements over a single target area throughout the scanning period (see Appendix A).

The lava lake TLS surveys were performed in December of 2008, 2009, and 2010. All scans were made from scanning position 1 (Figure 2). The 2008 scan was collected over a 4-hour period, with a temporal resolution of 1.5 minutes and a spatial resolution of 2.6 cm. Both the 2009 and 2010 scans were collected over 8 hour time periods, with temporal resolutions of 1 minute and spatial resolutions of 3.1 cm. The full crater was surveyed in December 2010, in which 14 scans were taken at irregular intervals over a period of 7 days. Scans were taken from 2 scanning positions (scanning positions 1 and 2; Figure 2) on opposite sides of the crater rim in order to capture all angles of the crater. The scans had a mean spatial resolution of 3.6 ± 1.5 cm and were collected with at least 10% (4°) of overlap in order to lower alignment errors (*Bellian et al,* 2005). The measurement error associated with the scanner was measured during the 2009 field season and found to be: $RMSE_x = 4.0$cm, $RMSE_y = 3.3$cm and $RMSE_z = 2.1$cm (see Appendix A).

In addition to the TLS surveys performed for this study, an Airborne Laser Scanning (ALS) survey was flown over the summit plateau of Erebus volcano in 2001,

providing the first high-resolution Digital Elevation Model (DEM) of the summit and

Main and Inner Crater (*Csatho et al.*, 2008). The DEM was computed using a grid size of

2m x 2m and had an estimated RMS_z error of $\pm$ 0.49m (calculated using 12 independent

ground-based GPS measurements). The data collected during the 2001 ALS survey

proved to be useful for our study, not only because it was used to georeference all the

TLS data, but it also provided a comparison elevation model to allow for the examination

of decadal-scale changes in the summit crater.
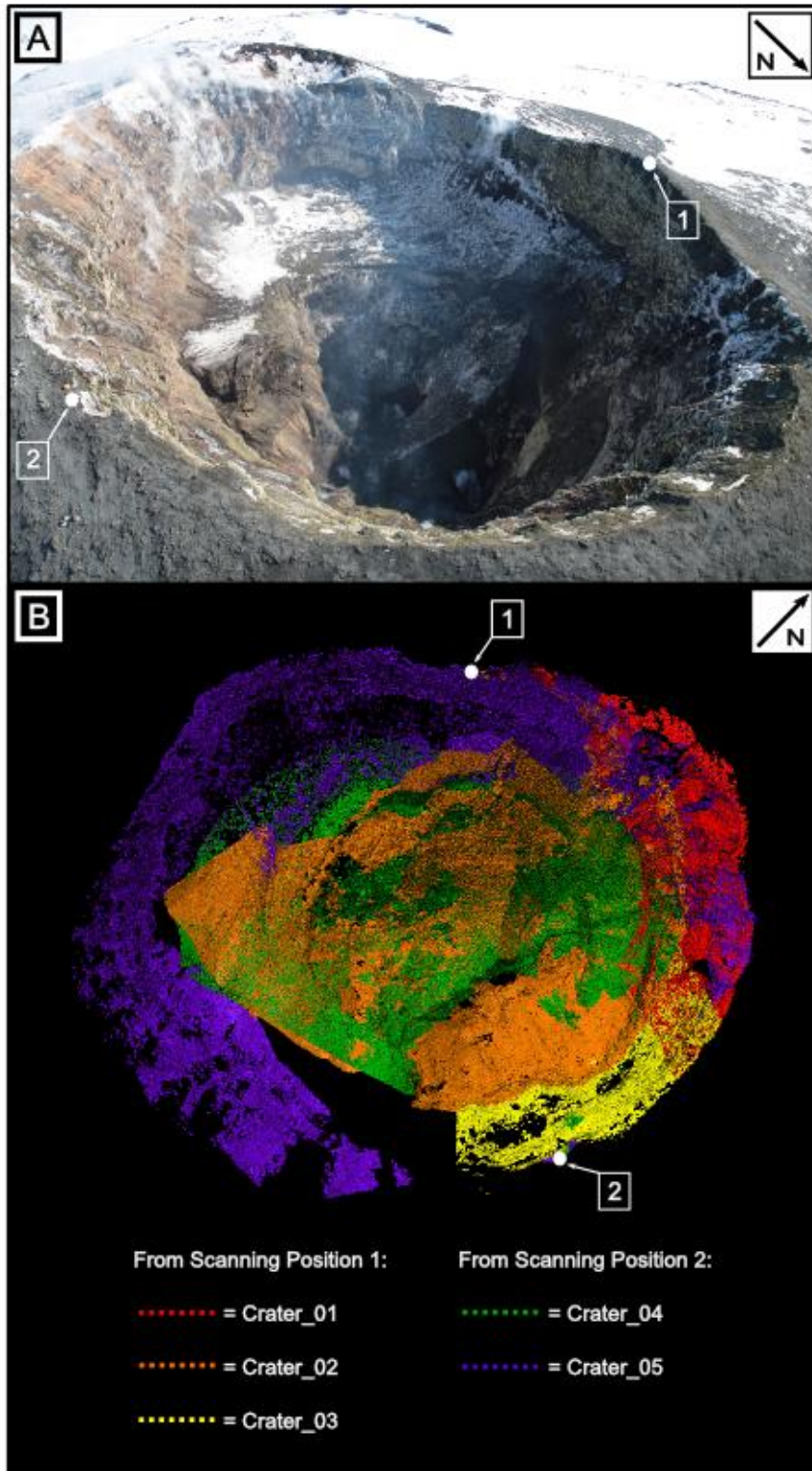
Figure 2 – (a) Aerial photo of the Erebus summit Main Crater and (b) Aerial view of the point clouds (from the 2010 Erebus crater scans) showing their positions relative to each other. The boxed 1 and 2 represent scanning positions 1 ("Shackleton's Cairn") and 2 ("Ray's"), respectively. These scanning positions can also been seen in Figure 1.

3.2. Scan Registration

All TLS and ALS point clouds were visualized, registered and analyzed using the PolyWorks v11.0 software (*InnovMetric*, 2010). Each TLS scan is collected in a unique scanner centered coordinate system, however in order for any comparisons between scans to take place, all the scans had to be transformed into a global coordinate system (i.e. merged into a single reference system). Due to the limited physical access into the interior of the summit crater, placement of reference targets within the scanning area was impossible. Therefore, registrations were performed using the Best-Fit alignment tool in PolyWorks IMAlign. This tool uses an iterative algorithm, similar to the Iterative Closest Point algorithm described by Besl and McKay (1992), to minimize the 3D distances between overlapping scans (e.g. *Abellán et al.*, 2011). All scans collected during a single field season were registered to each other and then registered as a single rigid group to the previous year's data. The 2010 TLS scans were registered to the 2001 ALS DEM (*Csatho et al, 2008*), which was used as a fixed reference. The surface-matching algorithm was only applied to parts of the crater that appeared to be stable between scans. Dynamic feature such as the lava lake, blowing ice and dust and areas affected by mass movements were manually excluded.

The horizontal coordinates of the final aligned data are in WGS 84 (UTM zone 58S) and the elevations are ellipsoid heights (WGS-84). This height is measured relative to the reference ellipsoid (a mathematical representation of the Earth's surface) in contrast to the heights usually recorded on traditional maps which are orthometric heights, commonly referred to as "Mean Sea Level" (MSL) heights, which are measured from the geoid (a surface of equal gravitational potential). The conversion from ellipsoid

to orthometric heights, and visa-versa, can be easily preformed using open source

calculators such as can be found at: http://sps.unavco.org/geoid/ (*Csatho et al.,* 2008*).*

3.3. Data Extraction

The scans of the lava lake (from 2008, 2009 and 2010) were manually extracted

from the point cloud and an average lava lake elevation and surface area were computed.

Distinct sampling regions were also isolated in order to independently examine the

elevation changes on different regions of the lake. The density of the data as well as the

geometry of the lake determined the size and location of the sampling regions. Since one

of the main goals of this study was to quantify the minute-scale changes across the lava

lake surface, the data density had to be adequate throughout the entire scanning

(temporal) period. This was problematic due to the fluctuating plume gases, which led to

highly variable visibility (and therefore data density) throughout the scanning window.

All the points within the newly sampled regions were collapsed into a 1-dimensional

elevation time series by discarding the x and y coordinate of each point within the region.

Multiple region sizes were tested to determine its effect on the time series (i.e. no

sampling bias) – the smallest possible sampling region was chosen which was adequately

sampled (both spatially and temporally) for an accurate time series.

Unfortunately the data collected in 2008 did not have adequate data density for

extracting a time series. The 2009 data was split into 8m-by-8m sampling regions;

however only a region in the northern and the eastern section of the lake had dense

enough data to extract a time series. The 2010 data, on the other hand, was very well

sampled both spatially and temporally, allowing for 5 2m-by-2m sampling regions (in the

northern, southern, eastern, western and central portions of the lake) to be extracted

(Figure 3).
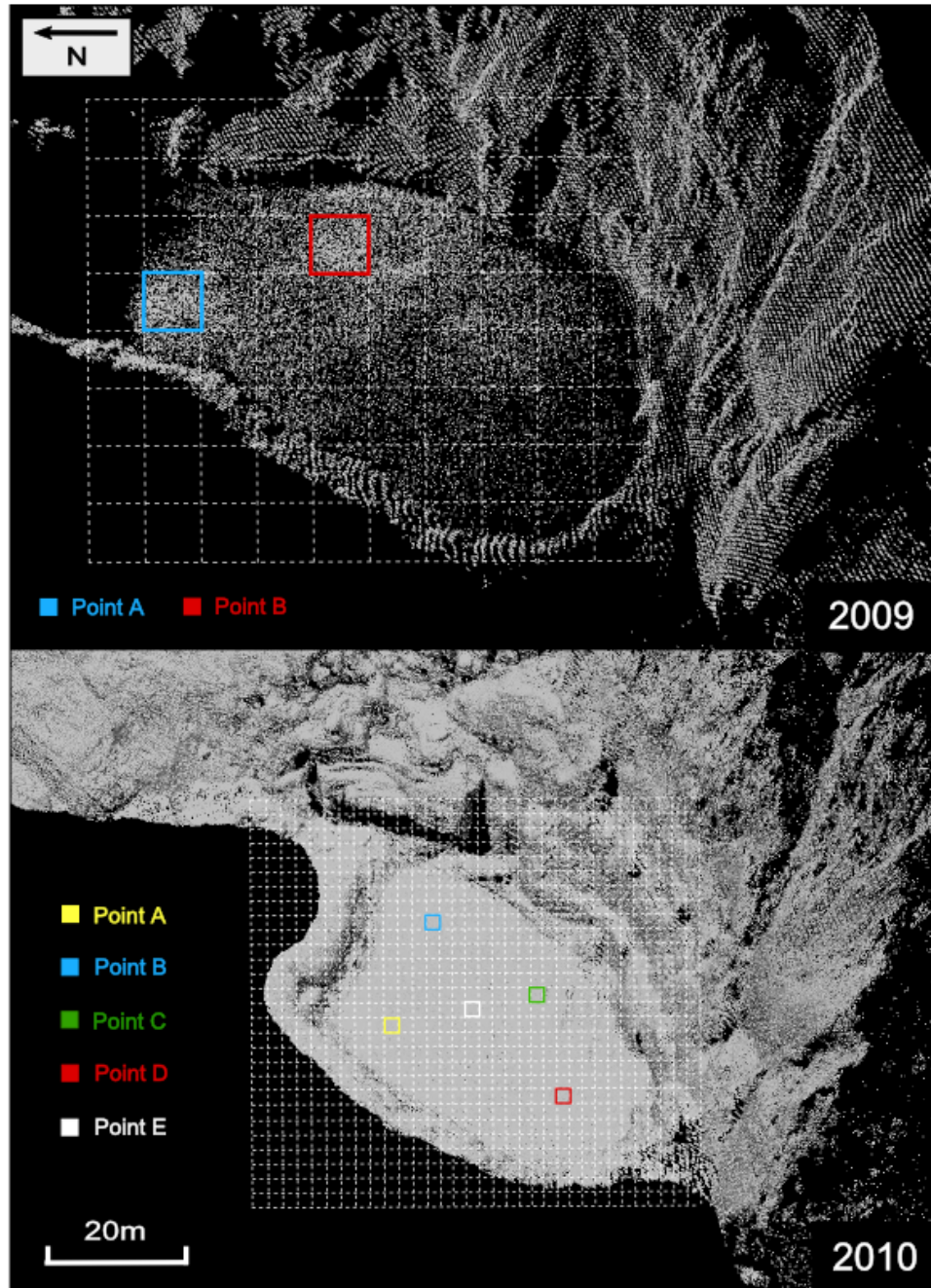
Figure 3 – Side views of the lava lake point clouds from 2009 (top) and 2010 (bottom). The boxes correspond to the areas where points were extracted in order to create the surface elevation time series. The 2009 data was split into 8m-by-8m sampling regions and the 2010 data was split into 2m-by-2m sampling regions.

3.4. 3D Data Visualization

In order to analyze and understand the morphology of the crater, it is essential to first create terrain classification maps using topographic attributes such as elevation and slope. To create such maps a Digital Elevation Model (DEM) of the crater was generated from the point cloud. A DEM is a grid of z-values at regularly spaced intervals in the x and y directions. For this survey a DEM using a grid spacing of 0.25m-by-0.25m was created in order to visualize and analyze the morphology of the crater. A DEM was also created with a grid spacing of 2m-by-2m (chosen based on the spacing of the DEM generated from the 2001 ALS dataset) in order to allow for a comparison between the 2 datasets. A Triangulated Irregular Network (TIN) was also generated in order to create a true 3D visualization of the surface, unlike the 2.5D DEMs. A TIN is a surface mesh in which discreet points are connected through a series of triangles, each triangle having its own slope and aspect – in this case it was computed using the screened Poisson surface reconstruction method (*Kazhdan and Hoppe*, 2013). The resolution of this generated surface is variable and directly depends on the density of the point cloud.

CHAPTER 4 – DATA RESULTS AND ANALYSIS

4.1 *Morphology of the Summit Main Crater*

Current knowledge of the morphology of the summit crater is limited to yearly

ground observations (during the austral summer) as well as to a single 2001 ALS survey

– which provided the first complete measurements of crater geometry as well as

quantitative descriptions of its main features (*Csatho et al., 2008*). Due to the expense

and limited availability of airborne lidar, it is not capable of providing the immediate and

continuous scanning necessary in order to monitor this continuously active volcano in

such a difficult environment. The generation of a DEM and TIN of the summit crater

from the 2010 TLS survey allowed for unprecedented accuracy (+/- 0.25m) in the

visualization of features within the summit crater (see the shaded relief representation of

the crater – Figure 4). DEMs also provide a means to extract and map important terrain

characteristics – such as the contoured elevation map seen in Figure 5. Using this

information, along with elevation profiles, detailed examinations and measurements of

the major features within the summit crater were made.
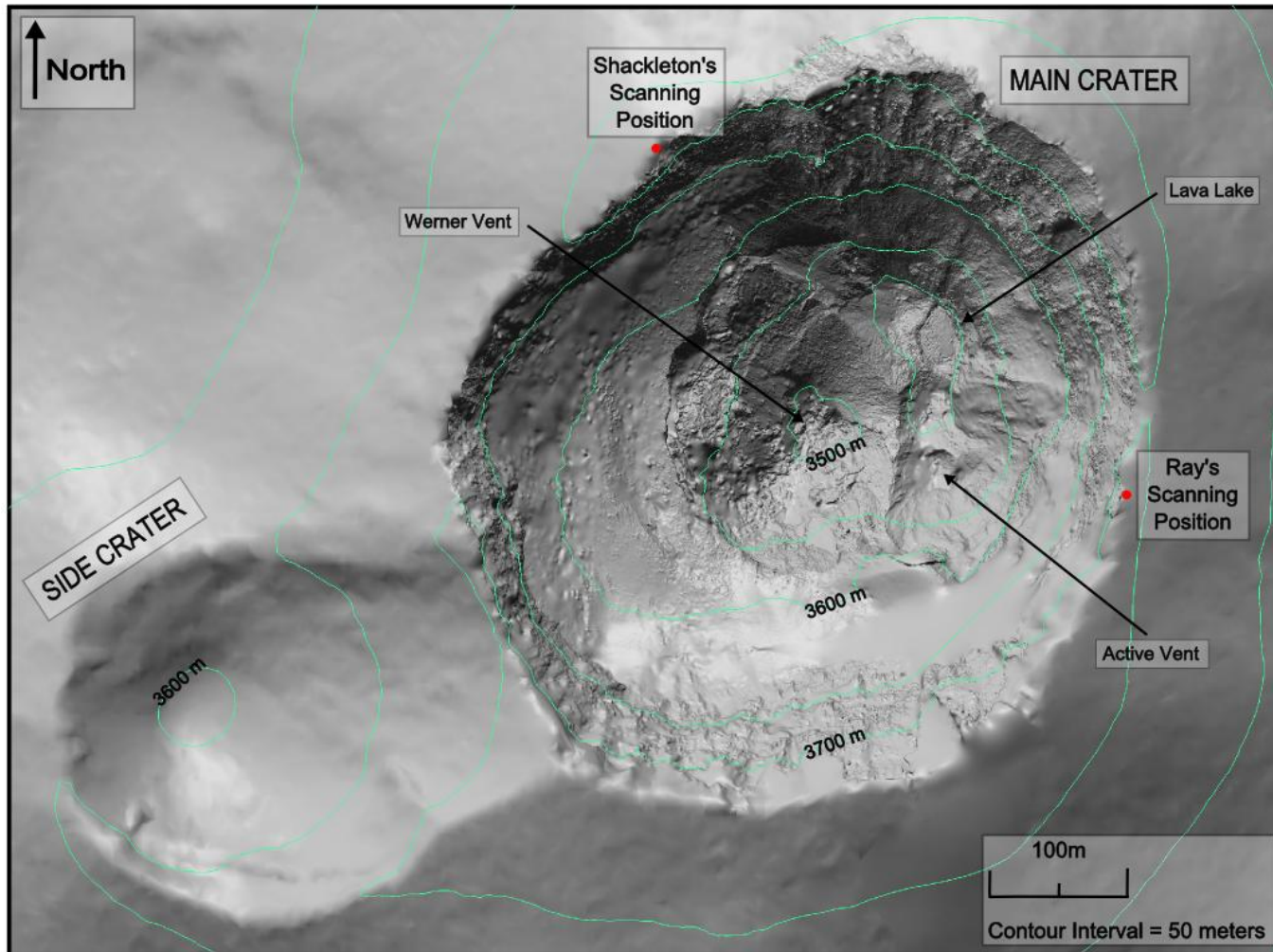
Figure 4 – Visualization of the morphology of the Erebus summit through a shaded relief map created by merging the 2001 ALS 2x2m DEM (which covers the entire summit region; *Csatho et al.,* 2008) and the 2010 TLS TIN (which covers only the Main Crater). 50m contour lines have been overlain and the scanning locations and some of the major features within the Main Crater have been labeled (including the lava lake, Werner vent and the active vent).
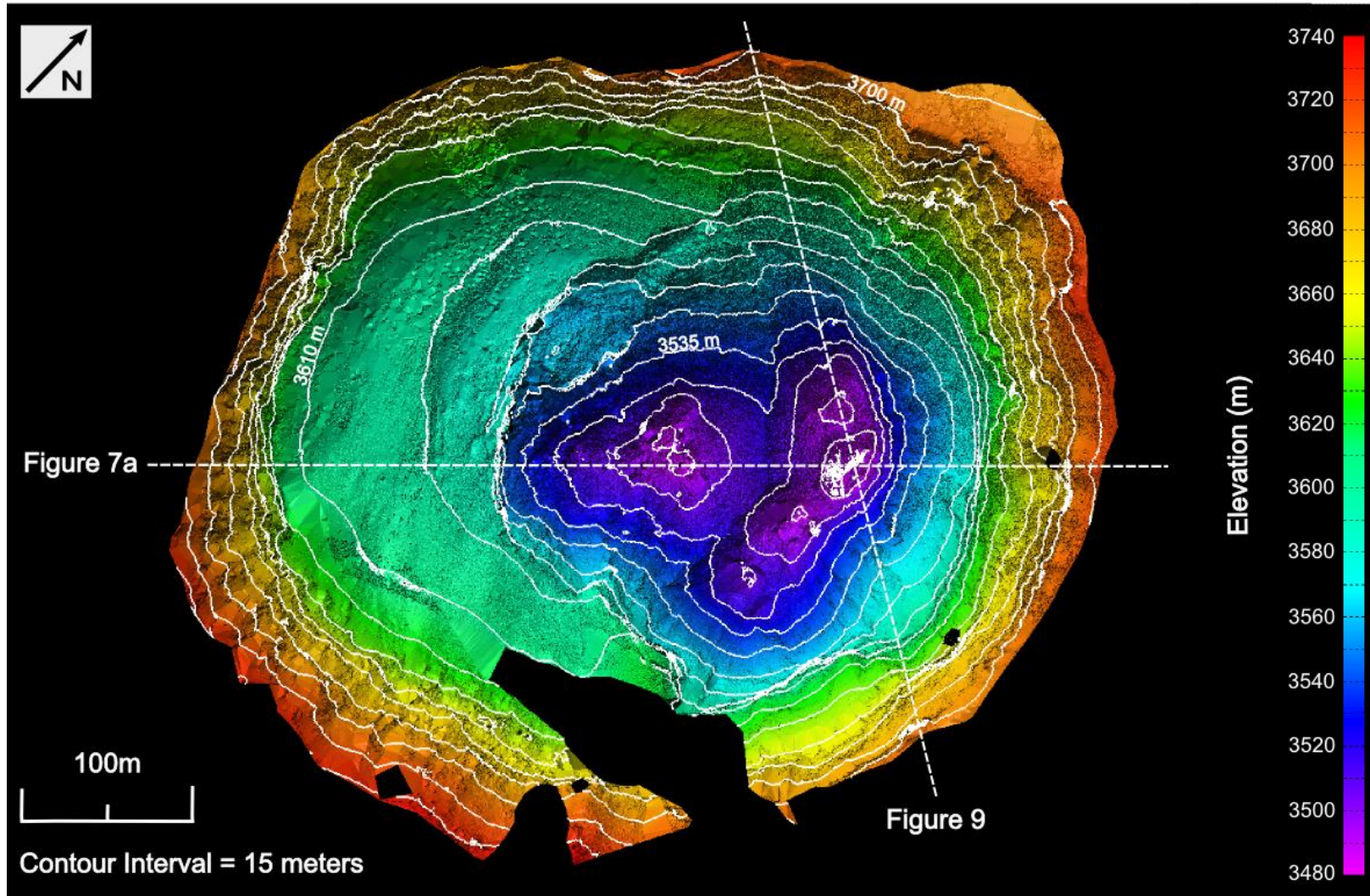
Figure 5 – A contoured elevation map overlain on the shaded relief map of the 0.25x0.25m DEM with 2 lines marking the location of an extracted elevation profile (see Figure 7a) and of extracted lava lake cross sections (see Figure 9). The elevations are ellipsoid (WGS-84).
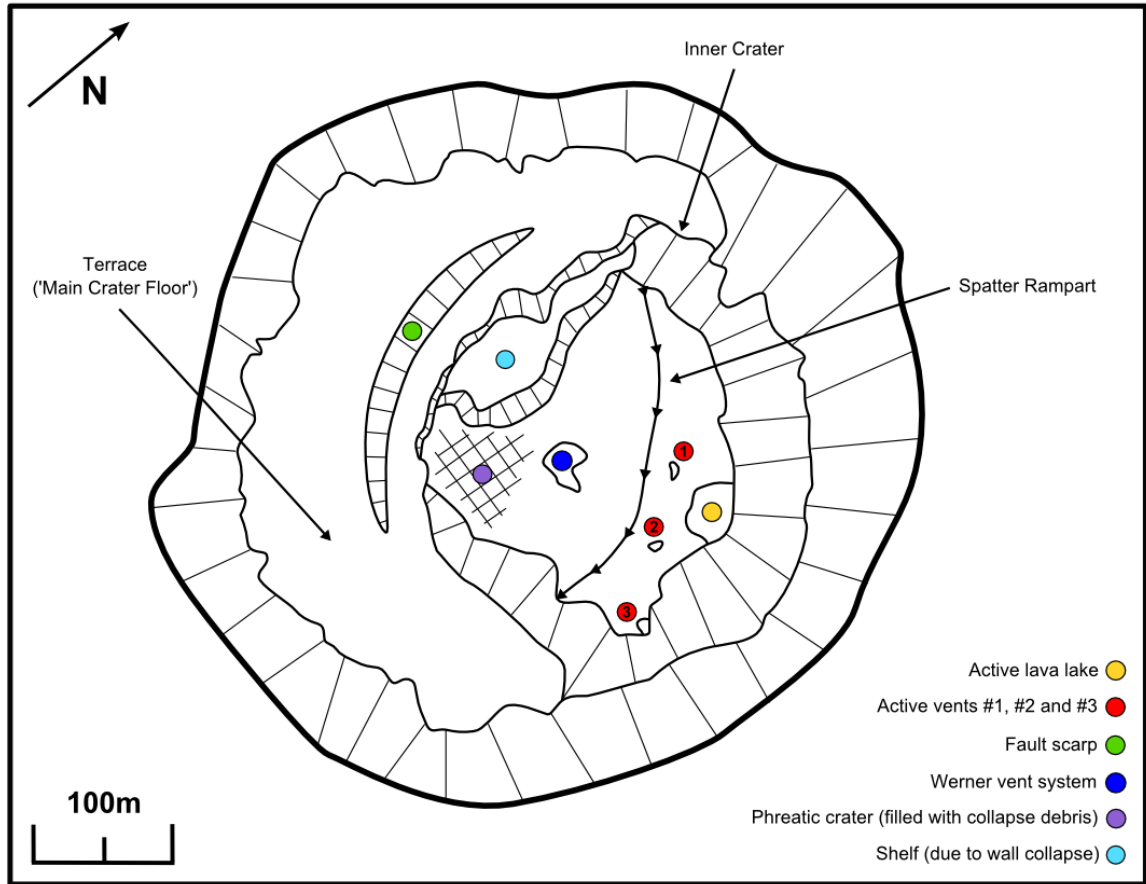
Figure 6 – Schematic map of the 2010 Main Crater with the main components and morphological features labeled; including the Inner Crater, terrace ('Main Crater Floor'), fault scarp, active lava lake, Werner vent, spatter rampart, phreatic crater and active vents.

The Main Crater rim forms an elongate ellipse 600 x 470m in diameter (long axis oriented NE). On the SW side of the Main Crater there is a dipping terrace (referred to as the Main Crater floor), which has a footprint of 265 sq m and lays an average of 135m below the crater rim. The terrace has an average slope of 14 degrees, dipping in a roughly Easterly direction towards the Inner Crater. However, the slope of the terrace decreases to 2 degrees towards the center of the terrace and increases up to 36 degrees towards the Main Crater wall. This increase is generally caused by the buildup of loose volcanic material which is the result of collapse events that commonly occur along the Main

Crater wall. Collapse events are also common along the Inner Crater wall, which cuts the terrace on the NE side. In fact, the entire northeastern edge of the terrace appears to be a zone of brittle failure with scarps cutting across the surface. A significant collapse can be seen in the elevation map along the western edge of the Inner Crater wall; the collapsed material is significantly higher in elevation (at an average of 3558m) from surrounding Inner Crater floor (which ranges from ~3520-3540m in that area). The "Phreatic Crater" is a remnant of 2 major phreatic eruptions on October 19th, 1993 that were responsible for widening the Inner Crater by approximately 80m to the SW (*Dibble et al.,* 1994). The crater is no longer a major feature within the crater – as observed in the 2001 ALS survey (*Csatho et al.,* 2008). This is likely due both to the accumulation of wall collapse material as well as the filling of volcanic material from large Strombolian eruptions.

The Inner Crater lies on the NE side of the Main Crater and forms a 260 x 320m diameter elongate ellipse (long axis oriented NE) and is 75m deep (at the deepest point) from the Main Crater Floor. All surface manifestations of volcanism within the summit crater are contained within the Inner Crater, including the active lava lake as well as many other active vents and fumaroles. The geometry of these features can be seen in the elevation map (Figure 5) and a SW-NE elevation profile across the crater (Figure 7a). The Inner Crater consists of 2 distinct zones of depression (where the volcanic activity is concentrated), separated by an 80m wide ridge of built-up volcanic material (which has an average elevation of 3517m). The depression to the NE consists of the main lava lake (known as the "Ray Lava Lake") as well as 3 active vents, while the depression to the SW consists solely of the "Werner Vent" system (which periodically has had short-lived lava lakes and lava flows, such as in the austral summers of 2004 and 2013; *Calkins et*

al., 2008; *Philip Kyle, pers. comm.*). In 2010, the "Ray Lava Lake" lay at an average

elevation of 3490m and had a surface area of 862m^2. The active vents (labeled #1 - #3 in

Figure 6) had average elevations of 3493m (#1), 3491m (#2) and 3508m (#3) and surface

areas of approximately 112 m^2 (#1), 89 m^2 (#2) and 147 m^2 (#3). The Werner Vent

system had an average elevation 3492m and a surface area of approximately 635 m^2.
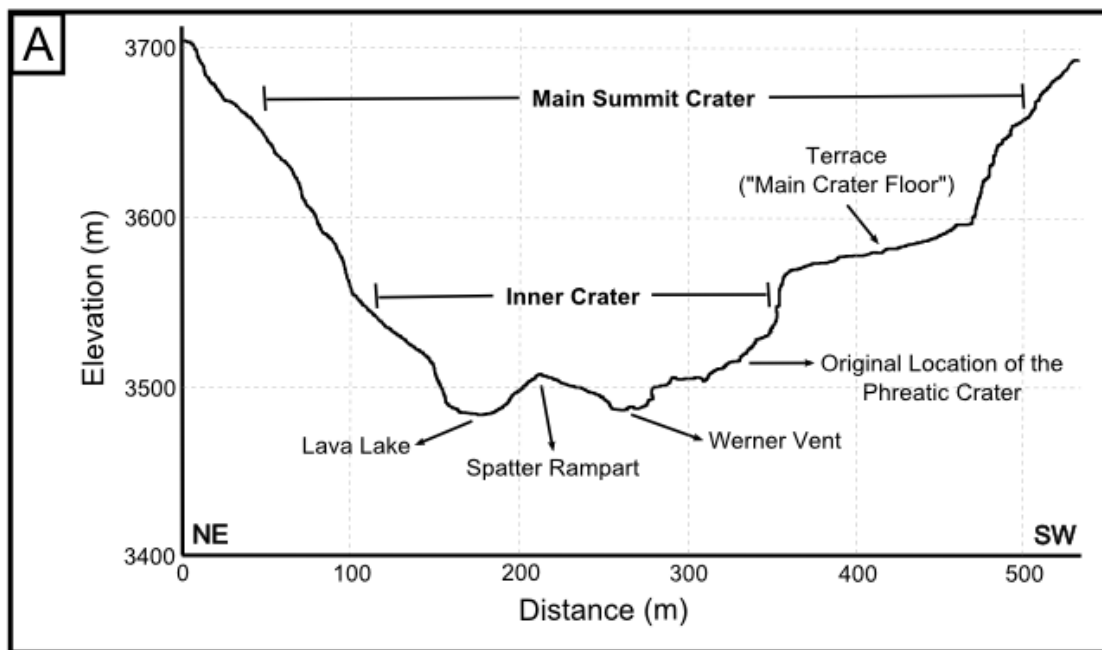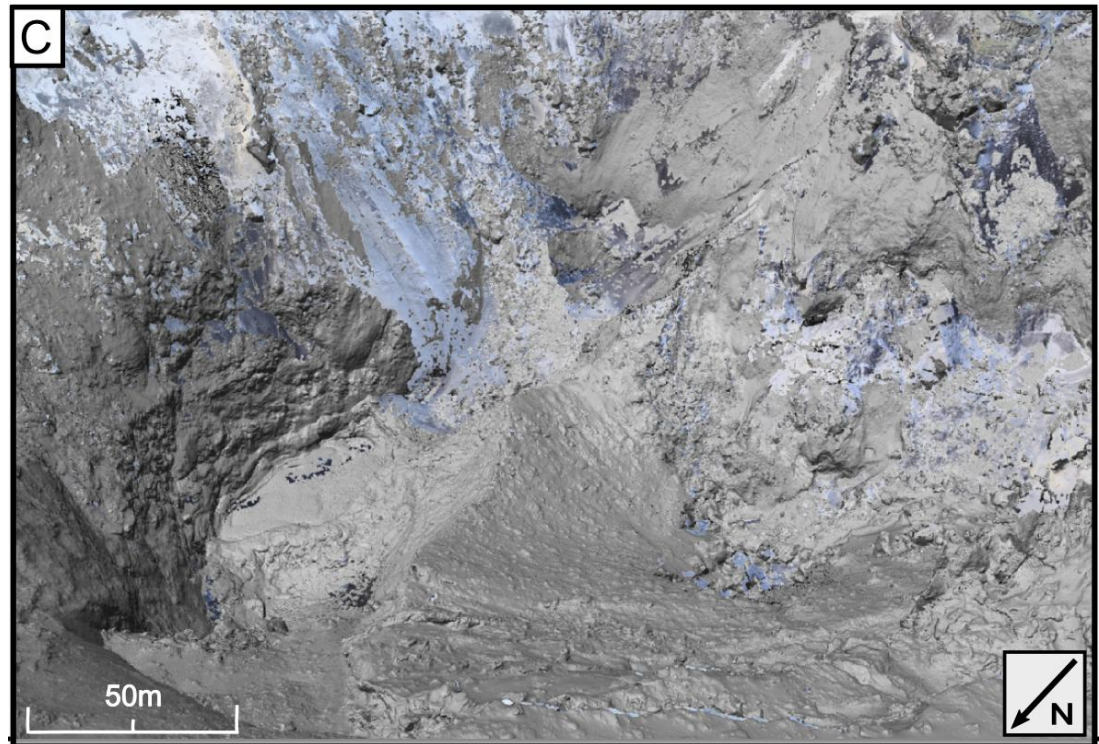
Figure 7 – (A) Elevation profile across the Main Summit Crater showing the main morphological features within the Inner Crater. The location of the profile can be seen in Figure 5. (B) A picture (taken from the Shackleton's Cairn scanning position) of the Inner Crater in 2010 with the main volcanic features labeled and (C) the point cloud of the Inner Crater overlain on picture seen in part B.

4.2 Analysis of Temporal Changes to the Main Summit Crater and Lava Lake

The previous section discussed the average elevations and surface areas of the main features of the summit crater from the 2010 field season. Due to the active and unstable nature of the crater, the characteristics of these features are in a constant state of flux and can change dramatically on time scales ranging from minutes to years. Until now, this change has been almost impossible to quantify (or even to observe) since it was based only on aerial photographs, visual observations and a single airborne lidar survey (*Csatho et al., 2008*; *Dibble et al., 2008*; *Smithsonian Institution*, *2013*). Now with the addition of 3 years of TLS datasets we can quantify the temporal evolution of not only the lava lake but of the entire summit crater.

4.2.1 Decadal-Scale Deformation of the Inner Crater

We are able to examine the morphological changes that occurred in the Main Crater over 10 years (2001-2010) by comparing the 2001 ALS survey to the 2010 TLS crater survey. These morphological changes were quantified through changes in elevation, which were calculated by subtracting the Z coordinate of each grid cell in the 2001 ALS DEM from the equivalent grid cell Z coordinate in the 2010 TLS DEM. In order to calculate the elevation changes accurately between the 2 surveys a second DEM of the 2010 survey with a grid spacing of 2x2m was created (same spacing as the 2001 ALS DEM). Elevation changes were computed for every grid cell location and can be seen in Figure 8 overlain over the 2010 TLS shaded relief map. The error associated with these computations is a combination of the error of both DEMs (0.52m). As was previously

mentioned, the volcanic activity is concentrated within the Inner Crater and therefore it is of no surprise that the majority of deformation over the past 10 years occurred there as well. Minor elevation changes can also be noted along the Main Crater wall as well as the Main Crater floor and these can be associated with wall collapse events and the subsequent accumulation of collapse material.

The entire depression on the NE side of the Inner Crater lowered an average of 23.7m, with the vents lowering an average of 24.2m and the Ray lava lake lowered an average of 27.1m. The dramatic drop in elevation (of up to 39.2m) seen on the SE side of the lava lake is associated with a collapse of the Main Crater wall and a widening of the depression zone by approximately 20m. The Werner vent system lowered an average of 23.8m, very comparable with all the active vents in the NE depression. The collapse along the Inner Crater wall, which was described previously in the crater elevation map, can also be seen clearly in the map of elevation change (Figure 8). The collapse area is on the western edge of the Inner Crater wall and caused an average total drop in elevation of 26.4m. One small area on the SW edge of the crater rose 5.3m in elevation and represents the accumulation of material and filling of the Phreatic Crater. The remaining floor of the Inner Crater (excluding all previously mentioned zones) lowered an average of 6.1m. This collective subsidence equates to a net volumetric change of $-875,200m^3$ within the Main Crater between 2001 and 2010.
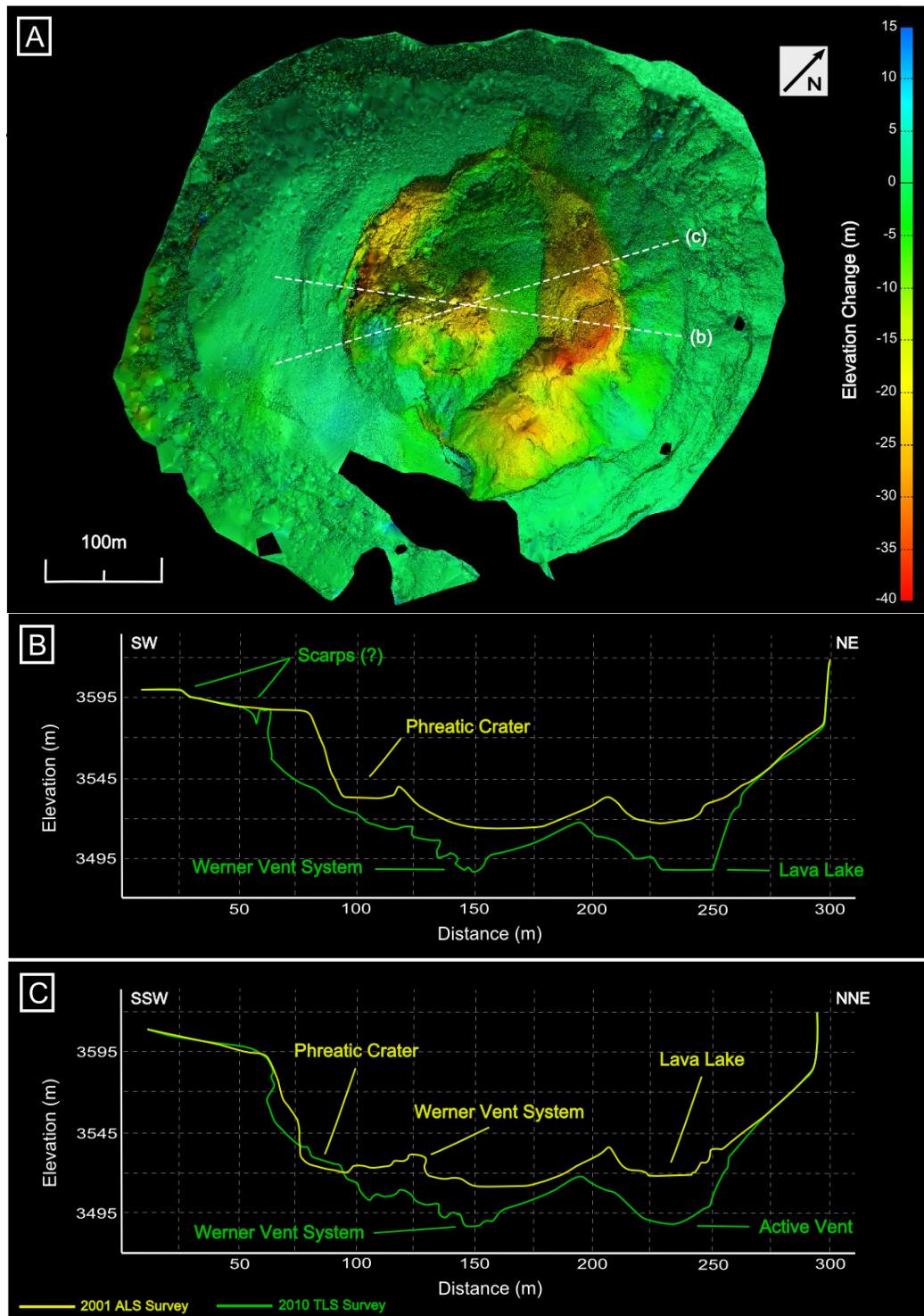
Figure 8 – (a) A map of the elevation changes that occurred between the 2001 ALS survey and the 2010 TLS survey overlain on the shaded relief map of the 0.25-by-0.25m DEM (b) A SW-NE transect and (c) A SSW-NNE transect across the Inner Crater which include elevation profiles of the 2001 and 2010 dataset with major feature labeled. The map indicates several dramatic changes in elevation over the past decade – including a general lowering of elevations within the Inner Crater (focused particularly in the active zones) as well as the erosion of the western Inner Crater wall and "Phreatic Crater." The elevations are ellipsoid (WGS-84).

4.2.2 Annual Changes in Lava Lake Morphology

Focused scans of the lava lake surface and the immediate surrounding areas were performed in 2008, 2009 and 2010 allowing for the annual monitoring of lava lake level, size and position within the Inner Crater. These results were also compared with the lava lake statistics derived from the 2001 ALS survey for a longer term examination of changes to lake morphology (Table 1). In 2001, the lava lake had a maximum length of 36m, a maximum width of 21m and a total surface area of 535 m^2. By 2008, when the first TLS survey was performed, the lake had dramatically increased in size to a maximum length of 71m, a maximum width of 38m and a total surface area of 1709m^2. There was minimal change between 2008 and 2009 with the maximum length remaining the same, the maximum width decreasing to 36m and the total surface area decreasing to 1699m^2. In 2010, the lava lake shrunk notably in size to a maximum length of 45m, maximum width of 26m and total surface area of 862m^2.

Table 1 – A summary of lava lake characteristics for every TLS survey year

Year	Max Length (m)	Max Width (m)	Surface Area (m^2)	Lava Lake Center Point		
				UTM Southing (m)	UTM Easting (m)	Elevation (m)
2001	36	21	535	1393469	552181	3517
2008	71	38	1709	1393468	552191	3497
2009	71	36	1699	1393466	552192	3494
2010	45	26	862	1393458	552202	3490

The location and elevation of the lava lake also varied from year-to-year. The average surface elevation of the lake was 3517m in 2001, 3497m in 2008, 3494m in 2009

and 3490m in 2010 (Figure 9). Since lidar-monitoring began in 2001, there appears to have been a period of deflation with the lava lake decreasing in elevation every year at a rate of ~ 3m/year. Also, over the same 9 year period, the center point of the lava lake migrated a total of 24 meters to the SE. The center of the lake was located at 1393469mS (UTM Southing) and 552181mE (UTM Easting) in 2001; 1393468mS and 552191mE in 2008; 1393466mS and 552192mE in 2009; 1393458mS and 552202mE in 2010.This southeasterly migration of lava lake can be seen in the cross-sections extracted along an approximate NE-SW transect of the lava lake scans (Figure 9).
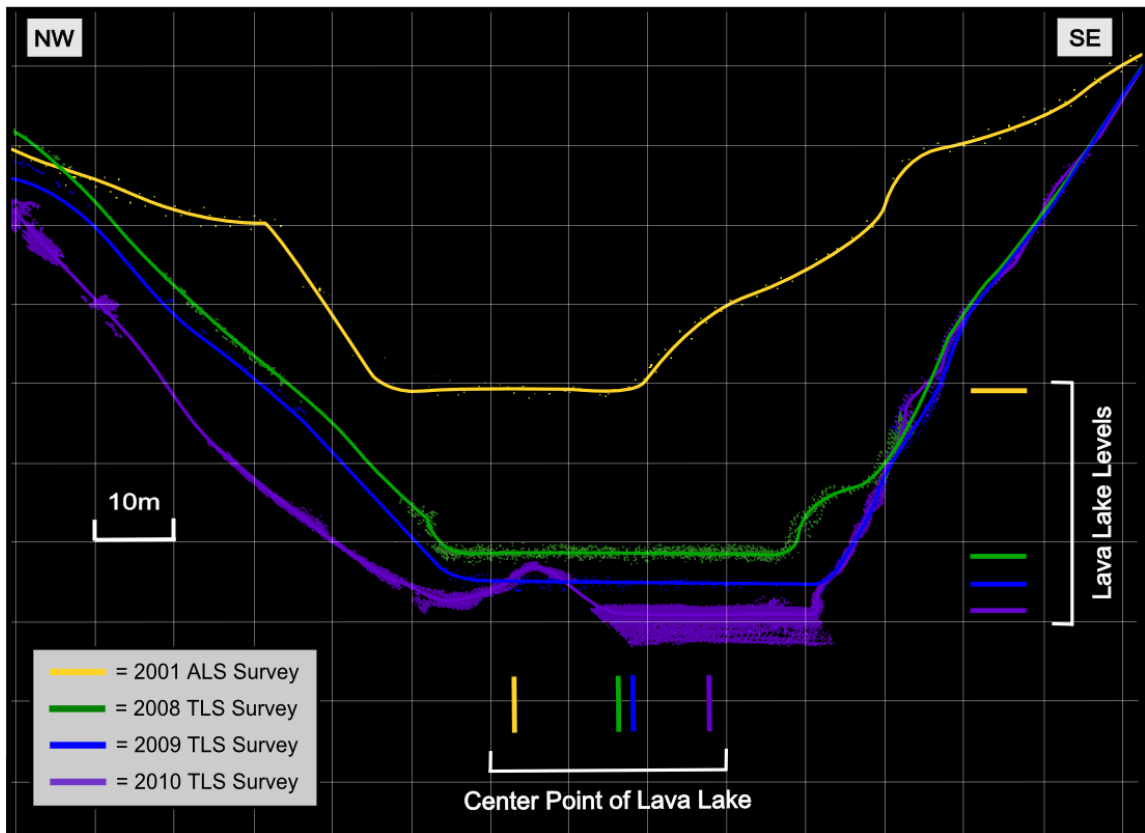
Figure 9 – Extracted cross sections from all the acquired lidar point clouds through the surface of the lava lake (the location of the cross-sections is shown in Figure 5). The results indicate an average yearly decrease in the elevation of the lava lake surface of ~3m/year. Note that lines have been drawn over the point clouds in order to better visualize the average top surface and that the vertical scatter seen in the 2010 point cloud is due primarily to the Strombolian eruption which partially evacuated the lava lake during the scanning.

4.2.3 Time Series of Lava Lake Surface Elevation

Continuous lidar scanning, coupled a pulse generator, allowed for a time series of the lava lake to be extracted for 2009 and 2010. These time series revealed clearly identifiable cycles in the elevation of the lava lake surface (Figures 10 and 11). In order to better visualize the cycles seen in the lava lake surface a one-minute running average filter was first run on all of the extracted locations in order to smooth out background noise (the temporal resolution of the scans was 1 minute). All of the points were then averaged at each minute in order to create a single time series with any point-to-point (3D) differences across the lava lake surface removed (Figures 10b and 11b).

In 2009, a time series of 151 minutes in length was able to be extracted from 2 points on the lake surface (Points A and B – on Figure 3). In timing the extracted series exhibit relatively synchronous cyclical behavior, however small amplitude differences can also be observed between the points, with the extracted elevations at Point B being on average 0.2m lower than those extracted from Point A. The cycles remained fairly consistent within the scan time with roughly symmetric lead and lag times. The cycle periods ranged from ~8 to 21 minutes with an average period of 16.2 ± 4.1(1ϭ) minutes. The largest change in surface elevation occurred at 96 minutes into the scan time, with a rise in elevation of ~1.5 meters (equating to a magma flux of ~2550 m^3 into the lava lake) over a period of 12 minutes. The average change in surface elevation (amplitude) per cycle is 0.91± 0.34(1ϭ) meters.

In 2010, a time series of 350 minutes in length was able to be extracted from 5 points across the lava lake surface (Points A through E – on Figure 3). Unlike the 2009

data, which remained consistent throughout the scanning period, the 2010 data can be split into 3 distinct segments (Figure 11b). The first segment (0-66 minutes) and third segment (212-350 minutes) exhibit relatively continuous cyclical behavior, comparable with that seen in the 2009 time series. In these 2 segments, all of the extracted points display good correlation in terms of the timing of the cycles, though in terms of amplitude two locations stand out from the rest. The elevations extracted from Point C lay ~0.15m above the point average and the elevations extracted from Point D lay ~0.3m below the point average. The cycles remain fairly consistent within each segment with roughly symmetric lead and lag times, although due to the 146 minute gap between the segments their average periods and amplitudes were calculated separately. The cycle periods ranged from ~4 to 18 minutes with an average period of $10.5 \pm 4.6(1\sigma)$ minutes for segment 1 and $13.6 \pm 1.7(1\sigma)$ minutes for segment 3. The largest change in surface elevation occurred at 289 minutes into the scan time, with a rise in elevation of ~1.2 meters (equating to a magma flux of ~1225 m^3 into the lava lake) over a period of 9 minutes. The average change in surface elevation (amplitude) per cycle is $0.60 \pm 0.17(1\sigma)$ meters for segment 1 and $0.73 \pm 0.30(1\sigma)$ meters for segment 2.

In contrast to the "steady-state" cyclic activity observed in the first and third segments, the second segment (66-215 minutes) documented a period of eruptive activity. Between 66 and 78 minutes, instead of observing the expected next cycle and subsequent rise in lake surface the elevation of the lake instead dropped an average of 0.35m (and a maximum of 1.2m at Point E) over 10 minutes. This was then immediately followed by a medium Strombolian-style eruption at 78 minutes, in which the lava bombs were thrown into the surrounding Inner Crater (however the lake was not fully evacuated). The scans

indicate that the eruption dropped the lake level an average of 3.23m over a one minute period, which is equivalent to an ejection of ~2780m^3 of magma from the lava lake. Over the next 6 minutes the lake steadily filled back up to its original level before the eruption, however instead of resuming "steady-state" behavior a bubble started to form on the surface (corroborated through visual observation) causing a further 1.1m observed rise in surface elevation over the next 4 minutes. At 92 minutes the bubble burst, a large plume of gas was released and the lake deflated ~1.69m over the next 8 minutes. This degassing cycle was then repeated over the ensuing 55 minutes with a 1.5m rise and bubble accumulation (over 29 minutes), a bubble burst and subsequent 1.61m deflation (over 9 minutes). Lastly, there was a 57-minute long "quiescent" period before the steady cyclic activity resumed. This period was considered "quiescent" because the averaged time series displays minimal variations in lake surface elevation; however this interpretation changes when examining the extraction locations separately as well as taking into account visual observations taken during this period.

Documented observations from the crater rim show that after the last bubble burst the activity on the lake surface diminished and minimal convection was seen, particularly on the North side of the lake which appeared to have developed a solidified crust. This is corroborated by the single point time series in which no cyclicity is seen at extraction point B (the northern-most location); minor cyclicity is seen at extraction points A, C and E; and strong cyclicity is seen at extraction point D (the southern-most location).
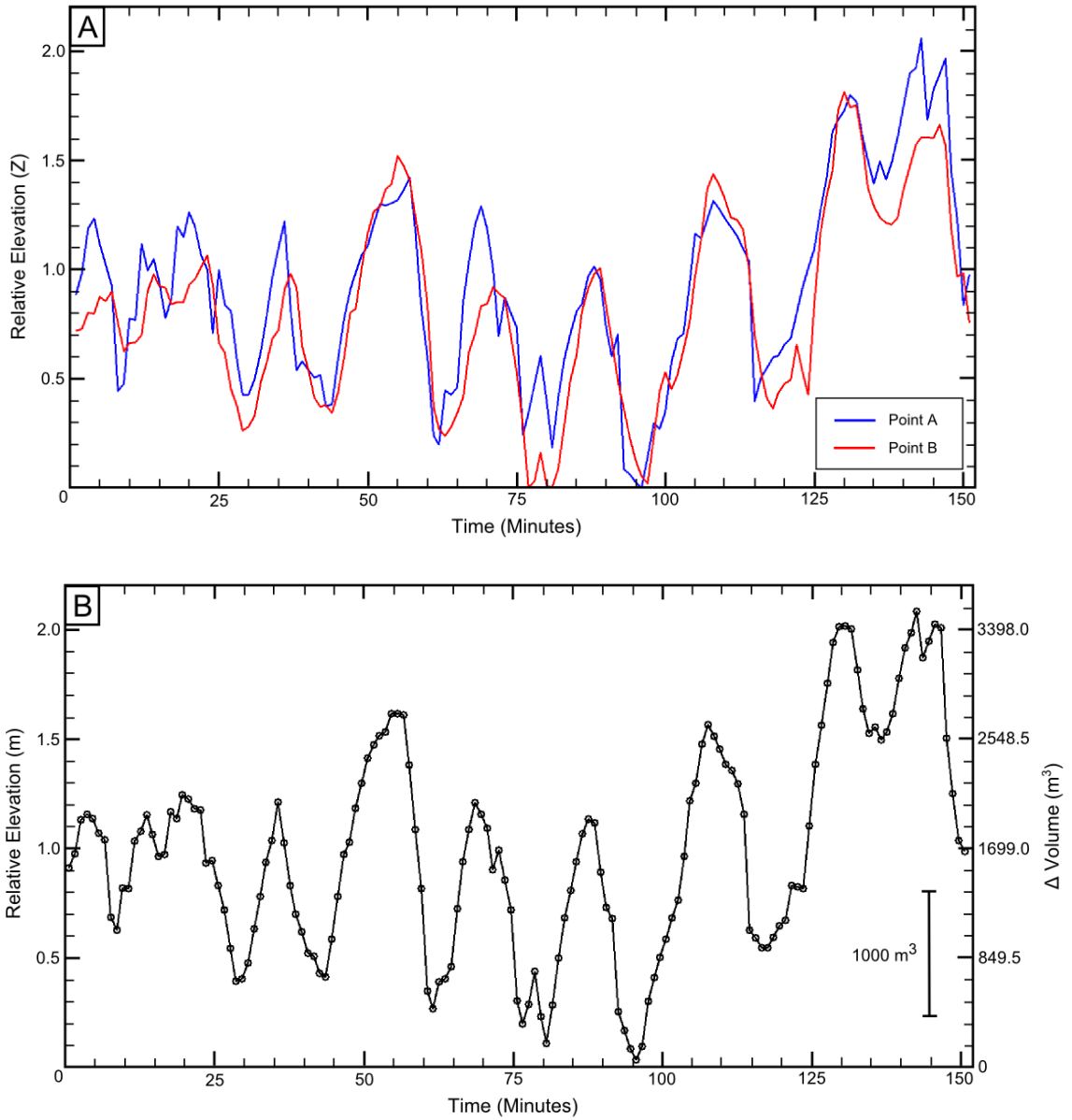
Figure 10 – The surface elevation time series extracted from the 2009 TLS dataset – (a) the raw data extracted from Points A and B on the lava lake surface (see Figure 3 for the extraction point locations) and (b) the point-averaged time series – which not only plots the relative elevation of the lava lake surface versus time but also plots the estimated volume flux of magma in and out of the lava lake, estimated using the surface area of the lake.
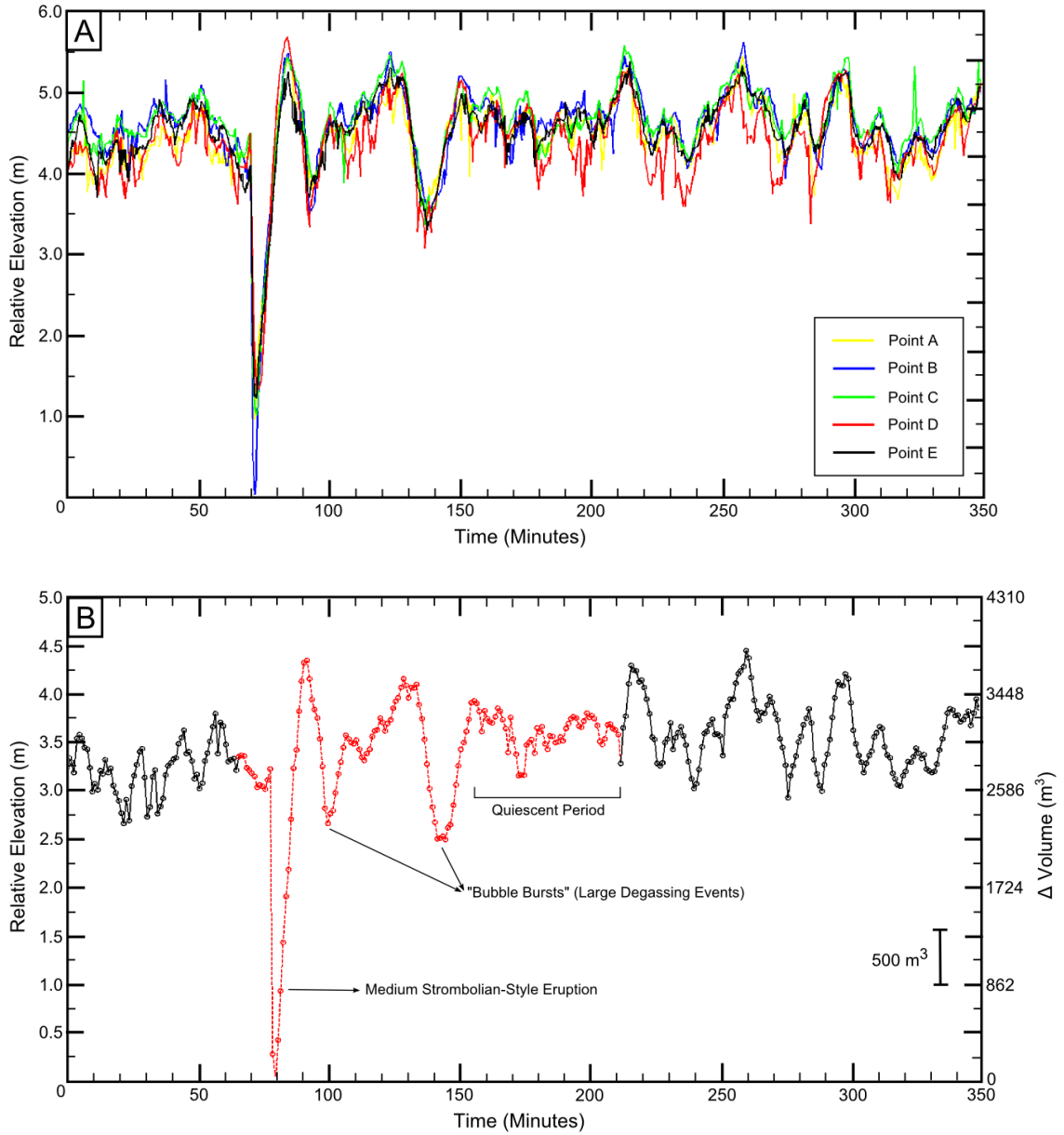
Figure 11 – The surface elevation time series extracted from the 2010 TLS dataset – (a) the raw data extracted from Points A, B, C, D and E on the lava lake surface (see Figure 3 for the extraction point locations) and (b) the point-averaged time series – which not only plots the relative elevation of the lava lake surface versus time but also plots the estimated volume flux of magma in and out of the lava lake, estimated using the surface area of the lake. The second eruptive segment, which will be removed from periodicity calculations, is highlighted in red with the main events labeled. These events include a medium Strombolian-style eruption at 78 minutes, two large "bubble burst" degassing events at 92 and 134 minutes as well as a 57-minute long "quiescent" period following the activity.

The initial estimates of cycle periodicity were based on simple trough-to-trough measurements of the point-averaged time series. However, in order to more accurately analyze the periodicity, power spectral analysis was utilized in the form of the Fast Fourier Transform (FFT) in order to derive a statistical distribution of frequencies in the power spectrum and to thereby identify the dominant frequencies (or periods) within the lava lake time series. Before the FFT analysis the data had to be preconditioned because the averaged time series still contained high frequency uncorrelated random noise. So in order to minimize these variations a 0-0.4Hz anti-alias low-pass filter was applied to the time series. Also, the eruptive period in the 2010 time series (Figure11b) was removed before any spectral analysis was performed.

The periodogram for the 2009 time series exhibits a prominent peak (i.e. dominant period) at 18.88 minutes (Figure 12). Three separate periodograms were generated for the 2010 time series, using the data: before the eruption (BE), after the eruption (AE) and both before and after the eruption (BAE). No dominant cycle period could be resolved in the BE periodogram, possibly because there is not enough data to resolve it or due to instabilities that occurred in the lava lake before the eruption. The AE and BAE periodograms, on the other hand, exhibit prominent peaks at 13.20 and 13.44 minutes, respectively (Figure 13).
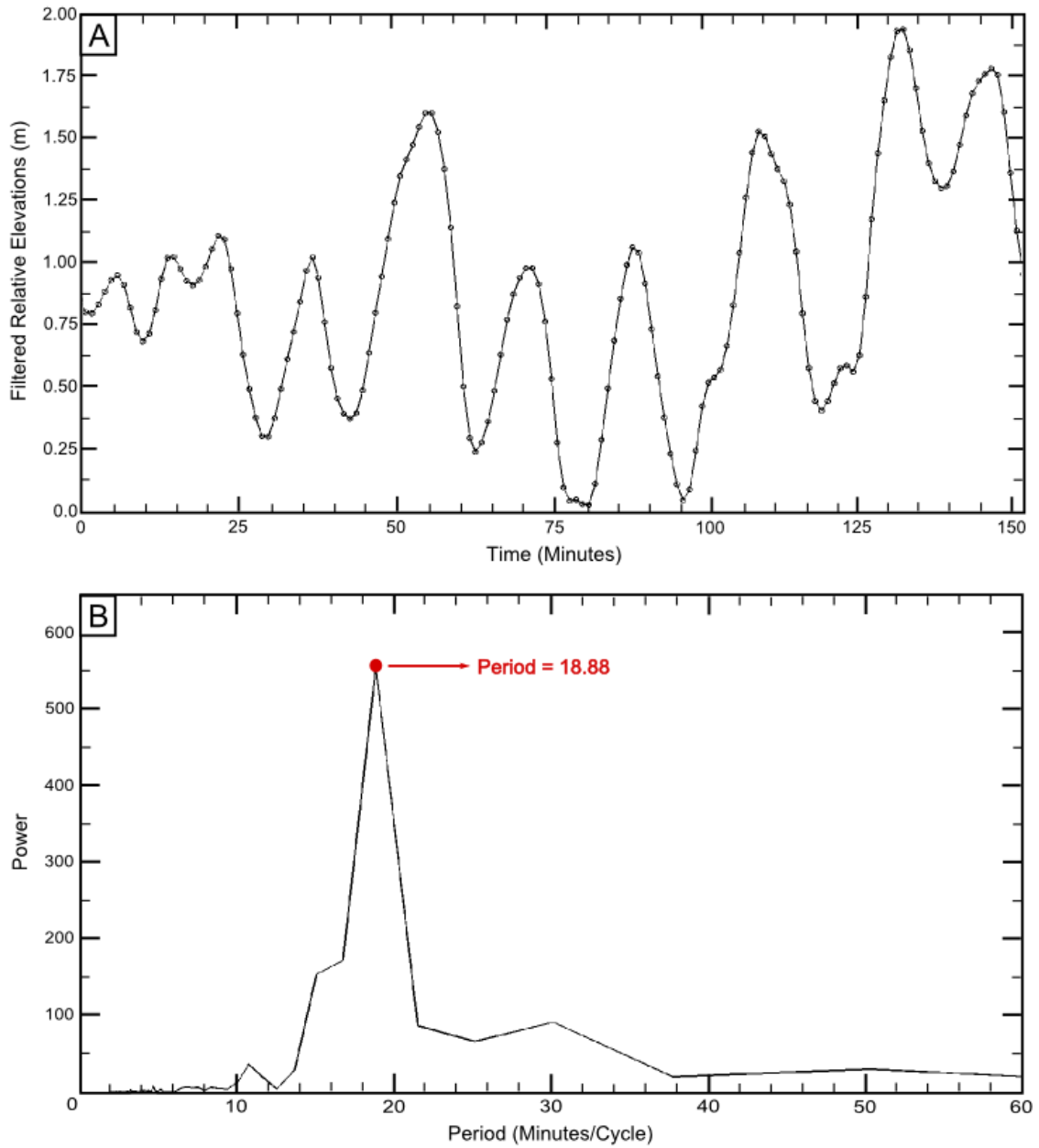
Figure 12 – (a) The 2009 low-pass filtered time series used in periodicity calculations. (b) A periodogram of the 2009 time series which displays a prominent peak (i.e. dominant period) at 18.88 minutes.
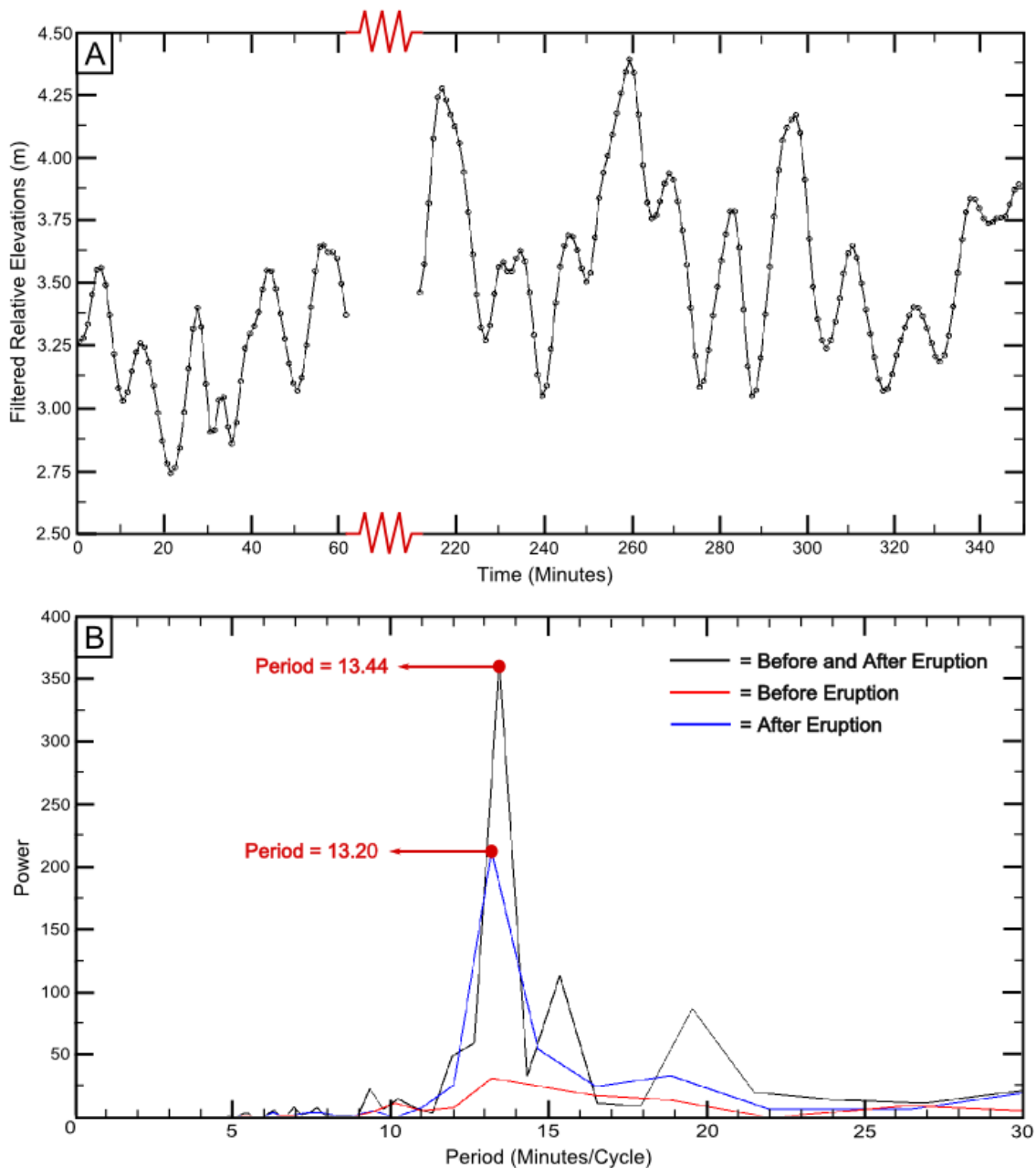
Figure 13 – (a) The 2010 low-pass filtered time series used in periodicity calculations – the eruptive period from 66 to 215 minutes has been removed. (b) Periodograms of the 2010 time series calculated using the data before the eruption (red line), the data after the eruption (blue line) and all the data (black line). No dominant cycle period could be resolved for the data before the eruption; however the data after the eruption shows a prominent peak at 13.20 minutes. When taking into account both the data before and after the eruption, the periodogram shows an even stronger peak at 13.44 minutes.

4.3 Computation of Volumetric Flow Rates

In addition to periodicity, volumetric flow rates were calculated from the lava lake time series data using the following equation:

$$Q = V \times A = \left(\Delta x / \Delta t \right) \times A \tag{2}$$

where Q is volumetric flow rate, V is velocity, A is cross-sectional area, Δx is displacement (i.e. the peak-to-trough and trough-to-peak changes in elevation measured on the time series data) and Δt is the time interval over which Δx was measured. Previous studies have observed that the lava lake was conical in shape (which would change the above equation), however during the 2010 eruption, when the lava lake was partially evacuated, it was observed that the top 4-5m of the lava lake had equivalent spatial extents (that is to say there were no significant changes in surface area at the highest and lowest observed lake levels). Therefore the surface areas measured from the point cloud and summarized in Table 1, 1699 m^2 in 2009 and 862 m^2 in 2010, will be sufficient in the computation of the volumetric flow rate using Equation 4. Also, the flow rates when the lake was rising (the "upwelling rates") were computed separately from the flow rates when the lake was dropping (the "downwelling rates") in order to differentiate any possible trends in the results.

Initially the volumetric flow rates associated with the steady cyclic upwelling and downwelling magma were computed (see Table 2) from the point-averaged data (Figures 11b and 12b). For 2009, the average upwelling flow rate was 3.2 ± 0.6 m^3/s and average downwelling flow rate was 3.9 ± 1.4 m^3/s. In 2010 these rates dropped and the average

upwelling flow rate was 1.8 ± 0.8 m^3/s and average downwelling flow rate was 1.9 ± 1.0

m^3/s. The outliers in these measurements consist of a few very large flow rates, primarily

in the downwelling rates. The 3 largest downwelling rates (6.4 m^3/s in 2009, 6.1 m^3/s in

2009 and 5.0 m^3/s in 2010), correspond to observations of "small" (~2-3 m large) bubbles

bursting at the surface of the lake.

Table 2 – Computed volumetric flow rates (m^3/s) of the upwelling and downwelling magma associated
with the cyclic fluctuations in lake level

	2009 Time Series		2010 Time Series	
	Upwelling Rates*	Downwelling Rates	Upwelling Rates	Downwelling Rates
	2.3	3.0	2.9	1.7
	3.0	2.7	1.5	1.4
	3.3	2.8	2.1	5.0
	2.8	6.4	1.2	1.4
	3.8	3.6	1.9	1.2
	4.1	4.4	3.6	1.7
	3.6	3.2	1.6	1.9
	3.2	3.4	1.5	1.4
	2.8	6.1	1.7	2.1
			1.7	2.2
			2.7	2.4
			1.1	2.1
			1.0	1.1
			1.4	0.6
Average:	3.2	3.9	1.8	1.9
Standard Deviation:	0.6	1.4	0.8	1.0

* Volumetric flow rate was computed using the following equation: $Q = V \times A = (\Delta x / \Delta t) \times A$

Additionally the volumetric flow rates associated with the eruptive activity, in

2010, were also calculated (Table 3), but were separated from the cyclic measurements

(and excluded from the computation of the yearly averages) since the underlying mechanisms which control them are likely very different.

The small Strombolian eruption drained the lava lake at a rate of 46.3 m^3/sec and after the eruption the lake refilled at a rate of 5.2 m^3/sec. The first and second large degassing events (which corresponded to the bursting of bubbles ~5-10m in diameter on the lake surface) had downwelling (drainage) rates of ~3.0 m^3/sec and upwelling (refilling) rates of ~1.9 m^3/sec, respectively.

Table 3 – Computed volumetric flow rates (m^3/s) of the upwelling and downwelling magma associated with the eruptive events of the 2010 field season

2010 Eruptive Events	Downwelling Rate	Upwelling Rate
Small Strombolian Eruption	46.3	5.2
First Degassing Event	3.0	1.9
Second Degassing Event	2.9	1.9

CHAPTER 5 – DISCUSSION

5.1 Geomorphology of the Erebus Summit Region

The measurement of ground deformation at active volcanoes has proven to be a very effective tool in the monitoring of subsurface magma movements and through the deformation patterns observed on the surface we are able to gain insights into the structure and plumbing of the volcano (e.g., *Lu et al.,* 2010; *Bonaccorso et al.*, 2011*)*. The combined analysis of the 2010 TLS survey with the 2001 ALS survey provided the first complete measurements of ground surface deformation within the Erebus summit crater. Previous ground deformation studies on Erebus (using tilt-leveling, trilateration and GPS measurements; *Otway et al.,* 1994*; Murray et al.,* 2006) showed little to no deformation along the summit flanks and the measurements in this study are in agreement with those findings. The subsidence we observed at the summit was confined to the Inner Crater with the largest subsidence focused along the walls and in the "active zones" (i.e. the lava lake and active vents) on the Inner Crater floor. The sub-circular pattern of deformation is suggestive of a ring fault system (*Gudmundsson,* 2007; *Holohan et al.,* 2011) whose surface expression defines the extent of the Inner Crater. The current subsidence is accommodated by slip along these curved faults and fractures and leads to the development of steep and in some cases overhanging walls which eventually

destabilize and collapse (*Pavez et al.,* 2006). These wall collapse events have been observed on Erebus for over 50 years, and combined with the continuous changes to the features and extent of the Inner Crater suggests that ground deformation has occurred (constantly or episodically) over this same period (Figure 14).
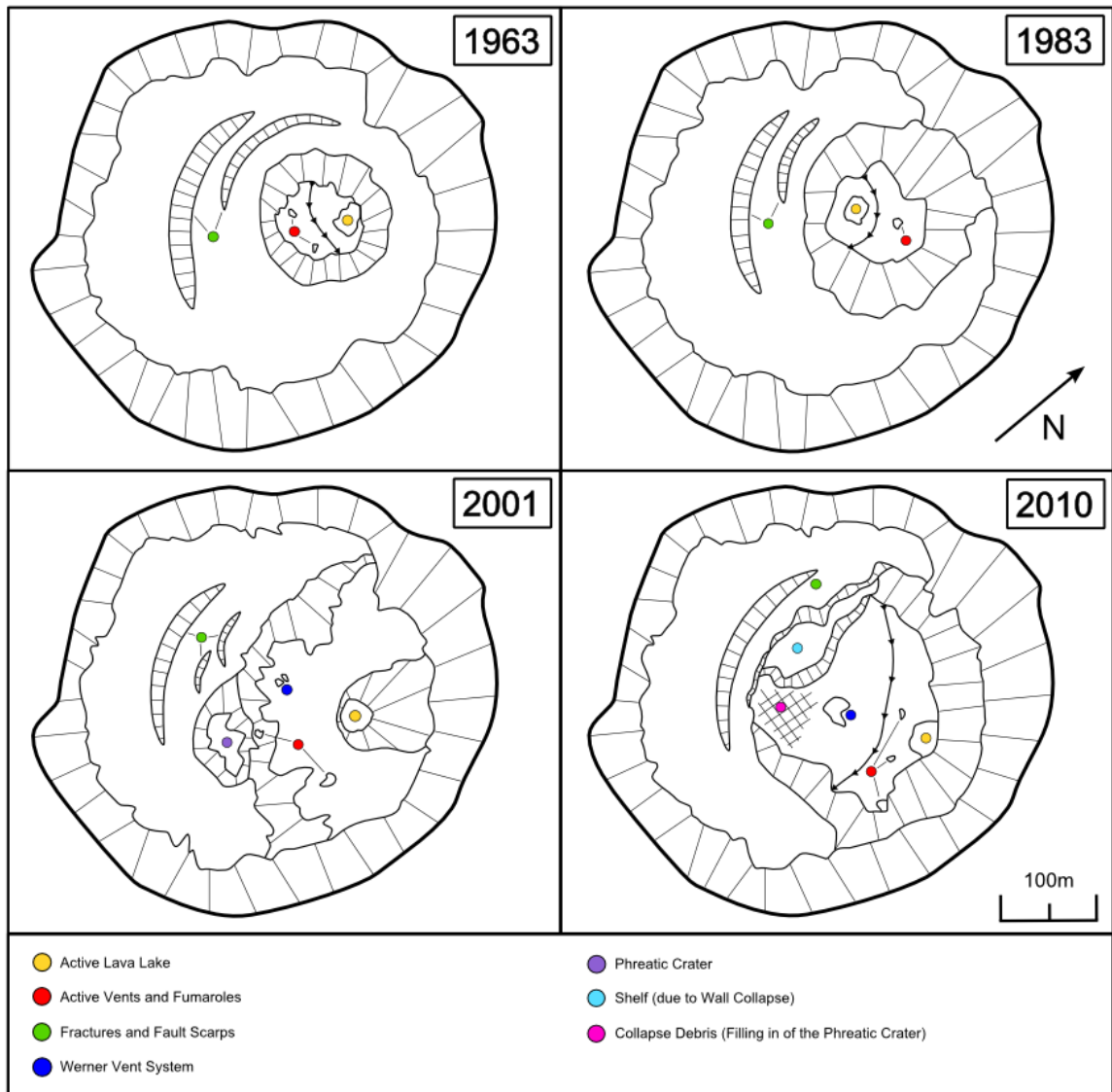
Figure 14 – Schematic maps of the Main Crater from (a) 1963, (b) 1983, (c) 2001 and (d) 2010 illustrating the continuous changes that have occurred to the features and extent of the Inner Crater over the past 50 years (information was compiled using aerial photographs from USARC, United States Antarctic Resource Center, as well as the following references: *Lyon and Giggenbach*, 1974; *Kyle and McIntosh*, 1978; *Kyle et al.*, 1982; *Blick*, 1987; *Csatho et al.*, 2008; *Philip Kyle*, pers. comm.).

Unfortunately the limited measurements available do not allow us to further constrain the timing of the deformation.

The pattern of subsidence observed on Erebus is consistent with the deflation of a magma body directly below the Inner Crater (*Pavez et al.,* 2006; *Gudmundsson*, 2012). However several recent Erebus studies conclude that the primary shallow magma chamber on Erebus exists ~500m WNW of the Main Crater (*Aster et al.,* 2003; 2008; *Zandomeneghi et al.*, 2013), meaning that it could not be the principal deflating source responsible for the observed deformation. It then becomes clear that a separate near-surface magma body or bodies must exist beneath the Inner Crater. A complex near-surface magma system with multiple side lobes (Figure 15) would also explain the inconsistencies observed in the spatial distribution of the deformation, i.e. the small-scale differences seen in the degree of deformation across the Inner Crater floor. Had a single deflating magma chamber existed beneath the crater then the entire region would have subsided to approximately the same degree. Instead the decrease in elevation in the "active areas" (e.g., the lava lake and vent systems) was an average of 6 times larger than the decrease observed in the central (spatter rampart) zone. This geometry could be resolved through the presence of 2 distinct magma bodies – one on the NE side of the Inner Crater (below the lava lake) and one on the SW side of the Inner Crater (below the Werner vent system).

The presence of a complex near-surface magma system would also explain the following behaviors observed in this and other studies:

(1) VLP preruptive bubble coalescence times (*Aster et al.*, 2003), vesicularity modeling (*Dibble et al*, 1994) and the lack of upwelling in the lava lake prior to the 2010 Strombolian eruption (Figure 10b) all indicate a shallow source for the coalescence of gas slugs (within 10s of meter).

(2) The comparable elevations and degree of subsidence between the lava lake and Werner vent system suggest that they are in magmastatic equilibrium and interconnected at depth, however there are distinct differences between the 2 systems. Though numerous lava flows, a short-lived lava lake (in 2004) and the 1993 phreatic eruption have existed in the Werner vent region no Strombolian eruption has ever been observed there (*Aster et al.*, 2003; *Philip Kyle, pers. comm.*) which indicates a pathway for gas and magma transport however a lack of adequate geometries for slug formation. This indicates a certain degree of isolation between the 2 systems which is corroborated through open-path FTIR spectroscopy of gas emissions performed in the austral summer of 2004. The measurements of gas emissions from the Werner lava lake showed a more "evolved" gas with a higher H_2O/CO_2 ratio and HF content then those emitted from the Ray lava lake (*Oppenheimer and Kyle,* 2008). This suggested that either the Werner vent system was being fed by a shallow offshoot of the main conduit, where the CO^2-rich preferentially travels through the main conduit which supplies the Ray lava lake, or that the Werner magma had gone through a more complete degassing as a result of cooling and/or decompression-induced crystallization.

(3) Across the Inner Crater surface there exists a large system of continuously changing vents, some of which sporadically host magma (Figure 5; *Giggenbach et al.*, 1973; *Oppenheimer et al.*; 2008). This is suggestive of a near-surface fracture system which

allows for a continually changing network of pathways to transport gases and

intermittently magma to the surface.
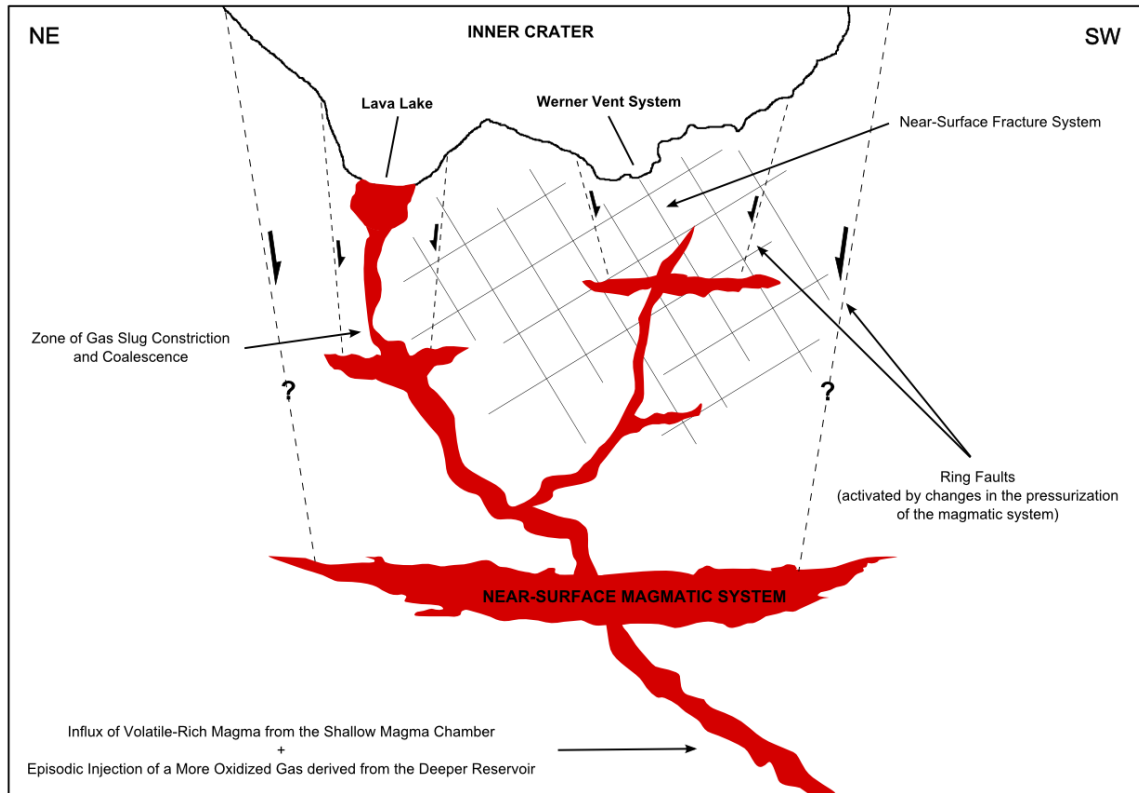
Figure 15 – Conceptual model of the near-surface magma system underlying the Inner Crater of Erebus volcano. The spatial pattern of deformation within the Inner Crater suggests the presence of 2 distinct magma bodies – one on the NE side of the Inner Crater (below the lava lake) and one on the SW side of the Inner Crater (below the Werner vent system). There is also evidence for the presence of a shallow coalescence zone for gas slugs as well as a near-surface fracture system which allows for a continually changing network of gas and magmatic pathways to be formed.

The question still remains as to the underlying mechanism that is responsible for

the depressurization and subsequent deflation of the near-surface magma system.

Generally the deflation of a magma body is attributed to the imbalance between to the

inflow and outflow of magma – where the outflow dominates due to magma intrusion or

increased eruptive activity (*Gudmundsson*, 2012). However, both geodetic and TLS

measurements suggest that no endogenous growth is occurring around the summit region

thereby making intrusions an unlikely reason for the depressurization. In addition, the 2008-2010 field seasons marked a very low eruptive period with only small Strombolian eruptions occurring a few times a week, suggesting that deflation due to eruptive magma loss is also unlikely. The extracted time series data showed a significant decrease in the volumetric flow rate to the lava lake of 3.2 m^3/sec to 1.8 m^3/sec between 2009 and 2010 which corresponded as well to a decrease in the surface area of the lava lake from 1699 to 862 m^2. This decrease in flow rate and lava lake size suggests the continuing depressurization of the near-surface magmatic system despite a lack of eruptive activity.

All current models of the Erebus magmatic system suggest that volatile content and degassing govern the flow dynamics of the conduit and lava lake as well as the style and amplitude of the eruptive activity (*Molina et al.*, 2012; *Oppenheimer et al.*, 2008; 2011). Gas emissions from the lava lake have 2 distinct signatures – a shallow-derived gas which characterizes the passive degassing and a deeply-sourced and more oxidized gas which characterizes the Strombolian activity. *Oppenheimer et al.* (2011) proposed that this more deeply-sourced gas is the result of the intermittent injection of parental basanite from a deep reservoir which leads to an increase in volatile content and the creation of gas slugs which in turn would spur eruptive activity. I propose that the rate and size of the basanite injections are ultimately responsible for the deformation seen in the Inner Crater. Many studies have shown that increases in volatile content, bubble content and bubble size (as was seen in association with the basanite injections; *Oppenheimer et al.,* 2011) will cause a buildup of internal fluid pressure and consequently an increase in the pressurization of the magma body (*Sparks,* 1978; 2003; *Pinkerton et. al.,* 2002; *Woods and Hubbert,* 2003). Therefore any changes in the rate of

influx of magma from the deeper basanite reservoir will have an impact on the pressurization of the shallow magmatic system with 2 discrete end-members: 1) Increase in flux from the deep reservoir leading to an increase in the pressurization of the magma body and heightened eruptive activity and 2) Decrease in flux from the deep reservoir leading to a decrease in the pressurization of the magma body and minimal eruptive activity. This depressurization would also result in the deflation of the magma body and subsequent subsidence of the ground above, as is currently being seen in the Inner Crater. The surface expression during highly eruptive periods, on the other hand, is much more complex and difficult to predict. The increase in flux would in theory lead to a period of inflation, however in this open-system the increased flux would also lead to heightened eruptive activity which would complicate the pressure dynamics of the near-surface magmatic system.

5.2 Proposed Models for Cyclic Lava Lake Behavior

The TLS measurements also reveal smaller-scale changes, spatially and temporally, in the cyclic rise and fall of the lava lake surface. Cyclic oscillations in lava lake level have been previously proposed based on both theoretical arguments (*Witham and Llewellin*, 2006; *Oppenheimer et al.,* 2009) and laboratory simulations (*Witham et al.,* 2006; *Hubbert and Hallworth*, 2007) and have now not only been observed in this study but also at the lava lake located within the summit vent at Kilauea Volcano in Hawai'i (*Carbone et al.,* 2013). In order to explain the observed cyclic behavior, two distinct models of conduit flow will be examined.

The first model (based on *Witham et al.*, 2006 and *Witham and Llewellyn,* 2006) suggests that changes in pressurization, which are ultimately controlled by the gas bubble behavior in the magma, can cause distinct periods of net upflow and downflow within the conduit (Figure 16). Net upflow is driven by a bubble-rich (and thereby low density) magma traveling up the conduit causing a decrease in the hydrostatic pressure at the base of the conduit. This will continue as long as balance is maintained between the increase in hydrostatic head associated with the rise in lava lake depth and the decrease in hydrostatic head associated with the higher bubble content in the conduit. The transition between net upflow and downflow will then occur when equilibrium is approached (i.e. when the lake approaches a depth such that upflow is decreased due to the higher hydrostatic pressure of the lake). When equilibrium is approached the bubbles rising in the conduit begin to coalesce (forming gas slugs) which are released at the lake surface. The release of these gas slugs can trigger instabilities in the equilibrium causing the gas content of the conduit to decrease and the hydrostatic pressure at the base of the conduit to increase to the point that it exceeds that in the chamber. When this occurs a period of net downflow will begin as the fluid is "pulled" from an area of higher hydrostatic pressure (the conduit) to an area of lower hydrostatic pressure (the shallow magma reservoir). This downflow will continue until the hydrostatic pressure of the reservoir increases and causes the downflow rate to decrease sufficiently enough for net upflow of the bubble-rich magma to begin again.
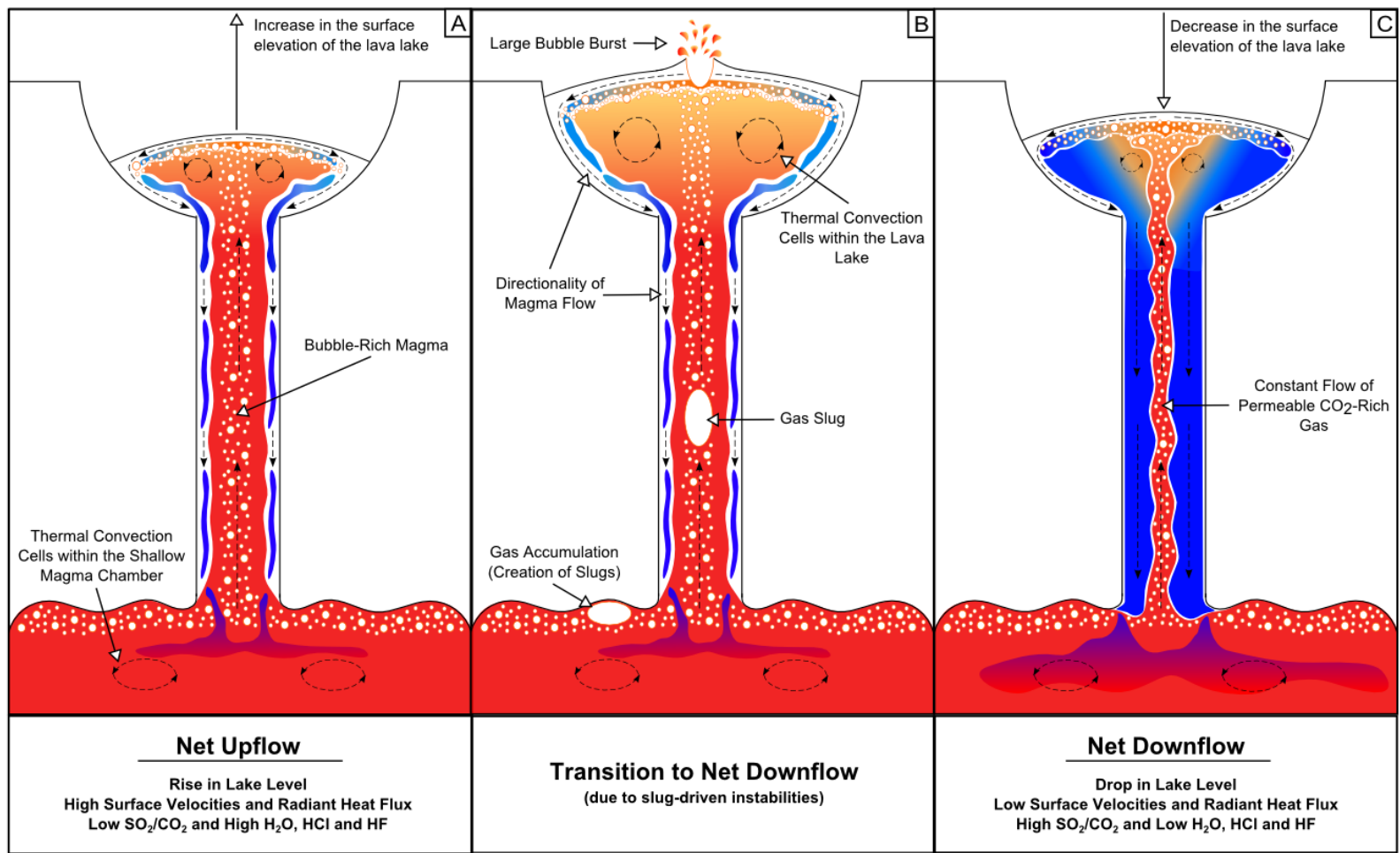
Figure 16 – Schematic drawings of the conduit and lava lake illustrating the flow model (based on *Witham et al.*, 2006 and *Witham and Llewellyn,* 2006) which suggests that changes in pressurization, which are ultimately controlled by the gas bubble behavior in the magma, can cause distinct periods of net upflow and downflow within the conduit. We suggest that this model explains the eruptive behaviors of the Erebus lava lake as well as plays a large role in the overall stability of the system, however does not explain the smaller-scale cyclicity observed. Not to scale.

This bubble-driven model, however, is unlikely to be the primary mechanism which controls the stable small-scale cyclicity as it requires a significant degassing event to occur in order to unbalance the system and trigger net downflow. It is probable though that this model does explain the behaviors of the lake when eruptive events do occur, as was observed in 2010 dataset. Every degassing event observed in 2010 triggered a significant net downflow which eventually (assuming once pressure equilibrium was reached) decreased and a period of net upflow started once again. After the eruptive period ceased, the lake returned to its original level and small-scale cyclicity began once again (Figure 11b). This suggests that pressurization plays a large role in the overall stability of the system, sustaining the steady-state dynamics of the lava lake through decades of documented Strombolian eruptions (*Oppenheimer et al.,* 2011).

The second model of conduit flow (based on *Oppenheimer et al.*, 2009 and *Hubbert and Hallworth*, 2007) suggests that cyclicity is a result of viscosity-based flow instabilities between the upwelling and downwelling magma. In laboratory models (*Hubbert and Hallworth*, 2007) it was seen that varicose flow instabilities can develop between high viscosity upwelling and downwelling magma which are prevented from mixing due to the viscosity contrasts at their boundary (ultimately due to the degassing occurring at the lake surface). This type of flow can even become so unstable that the upwelling magma will break into distinct segments as it travels to the surface. This viscosity-driven segmental flow results in the episodic flux of volatile-rich magma into the lava lake and thereby could explain the oscillatory behavior seen in the lake level (Figure 17). On Erebus, the process begins with the deep-degassing of CO_2 from the parental basanite (starting from pressures of ~8 kbar; *Oppenheimer et al.*, 2011). The

separated flow of permeable CO_2-rich gas then rises through magmatic system and becomes the primary constituent of the persistent plume that is emitted from the lava lake and other active vents (the proportion of CO_2 in the plume has been measured between ~ 36-40 mol% and the flux has been ~ 11.46-15.4 kg/s; *Oppenheimer and Kyle*, 2008; *Oppenheimer et al.*, 2009). The still volatile-rich, though no longer CO_2 saturated, magma then enters the shallow magma chamber and ultimately travels up the conduit towards the lava lake in discrete segments. When a slug of magma enters the lake, the gas bubbles ascend to the surface, the lava lake level rises, surface velocities increase exposing more incandescent magma (thereby increasing the radiative heat flux) and the low pressure degassing of H_2O, SO_2, HCl and HF begins (*Oppenheimer et al.*, 2009; *Calkins et al.*, 2008). Once degassed, the lava lake level falls as the denser (de-volatized) magma sinks down the edge of the lava lake into the conduit and back down into a magma chamber where it mixes and is re-volatized.
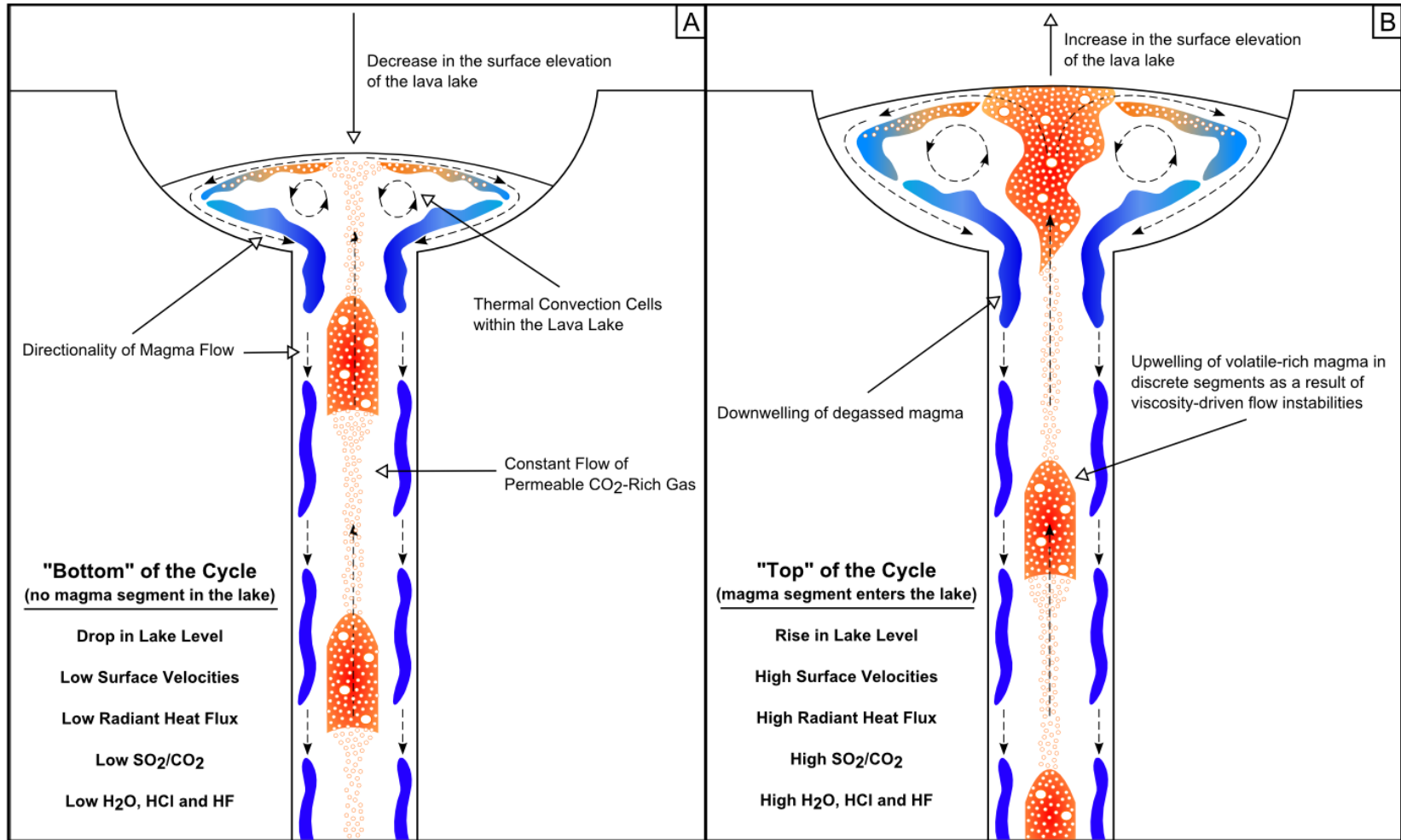
Figure 17 – Schematic drawings of the conduit and lava lake illustrating the flow model (based on *Oppenheimer et al.,* 2009; *Hubbert and Hallworth,* 2007) which suggests that the cyclicity is a result of viscosity-based flow instabilities between the upwelling and downwelling magma which causes the upwelling magma to break into distinct segments as it travels to the surface. This viscosity-driven segmental flow results in the episodic flux of volatile-rich magma into the lava lake and thereby could explain the oscillatory behavior seen in the lake level. Not to scale.

CHAPTER 6 – CONCLUDING REMARKS

TLS is a powerful new volcano monitoring tool which has provided a means for measuring the complex spatial-temporal changes occurring in the summit crater of Erebus volcano. Changes range from the large-scale yearly deformation occurring in the Inner Crater to the smaller minute-scale oscillations of the lava lake. Using these measurements we have been able to provide important new constraints on the dynamics of the conduit and subsurface magmatic system. In terms of its impact on future studies, the magma flux rate alone provides a key missing input into fluid dynamic models which could offer clues to deeper conduit geometries and the processes which govern fluid flow in the conduit. An accurate measurement of lava lake surface area is also critical for both heat and gas flux calculations. Much more work however needs to be done, including the continued yearly acquisition of full crater and lava lake scans, the acquisition of TLS data during highly eruptive periods and the correlation of the TLS data with seismic, gas and heat flux measurements. TLS applications at other active volcanoes can also be envisioned as no other technique has the ability to remotely and continuously measure the surface dynamics associated with volcanic activity at such small spatial and temporal scales.

REFERENCES

Abellán, A., J.M. Vilaplana, J. Calvet, D. Garcia-Sellés, and E. Asensio (2011), Rockfall monitoring by Terrestrial Laser Scanning - case study of the basaltic rock face at Castellfollit de la Roca (Catalonia, Spain), *Nat. Hazards Earth Syst. Sci., 11,* 829-841.

Aster, R., S. Mah, P. Kyle, W. McIntosh, N. Dunbar, J. Johnson, M. Ruiz, and S. McNamara (2003), Very long period oscillations of Mount Erebus volcano, *J. Geophys. Res., 108*, 2522.

Aster, R., D. Zandomeneghi, S. Mah, S. McNamara, D.B. Hendersono, H. Knox, and K. Jones (2008), Moment tensor inversion of very long period seismic signals from Strombolian eruptions of Erebus Volcano, *J. Volcanol. Geotherm. Res., 177*, 635-647.

Avian, M., A. Kellerer-Pirklbauer, and A. Bauer (2009), LiDAR for monitoring mass movements in permafrost environments at the cirque Hinteres Langtal, Austria, between 2000 and 2008, *Nat. Hazards Earth Syst. Sci., 9,* 1087-1094.

Bellian, J.A., C. Kerans, and D.C. Jennette (2005), Digital outcrop models: applications of terrestrial scanning lidar technology in stratigraphic modeling, *J. Sed. Res., 75*, 166-176.

Besl, P.J., and N.D. McKay (1992), A method for registration of 3-D shapes, *IEEE Trans. PRMI*, *14*, 239-255.

Blick, G.H., P.M. Otway, and B.J. Scott (1989), Deformation monitoring of Mt. Erebus, Antarctica, 1980-1985, in: J.H., Latter (ed.), *IAVCEI Proceedings in Volcanology*, vol. 1, *Volcanic Hazards*, Berlin, Heidelberg, Springer-Verlag, 554-560.

Boehler, W., M.B. Vincent, and A. Marbs (2003), Investigating Laser Scanner Accuracy, *The International Archives of Photogrammetry, Remote Sensing and Spatial Information Sciences (ISPRS)*, *34(5)*, 696-701.

Bonaccorso, A., A. Bonforte, G. Currenti, C. Del Negro, A. Di Stefano, and F. Greco (2011), Magma storage , eruptive activity and flank instability: Inferences from ground deformation and gravity changes during the 1993-2000 recharging of Mt. Etna volcano, *J. Volcanol. Geotherm. Res., 200,* 245-254

Calkins, J., C. Oppenheimer, and P. Kyle (2008), Ground-based thermal imaging of lava lakes at Erebus volcano, Antarctica in December 2004. *J. Volcanol. Geotherm. Res., 177,* 695-704.

Carbone, D., M. Poland, M. Patrick, and T. Orr (2013), Continuous gravity measurements reveal a low-density lava lake at Kilauea Volcano, Hawai'i, *Earth Planet. Sci. Lett., in press.*

Carrigan, C.R. (2000), Plumbing systems, in: H. Sigurdsson (ed.), *Encyclopedia of Volcanoes,*
San Diego, Academic, 219–235.

Chaput, J.A., D. Zandomeneghi, R. Aster, H. Know, and P.R. Kyle (2012), Imaging of Erebus volcano using body wave seismic interferometry of Strombolian eruption coda, *Geophys. Res. Lett.*, *39(7),* L07304.

Csatho, B., T. Schenk, P. Kyle, T. Wilson, and W.B. Krabill (2008), Airborne laser swath mapping of the summit of Erebus volcano, Antarctica: applications to geological mapping of a volcano, *J. Volcanol. Geotherm. Res.*, *177*, 531-548.

Dibble, R.R, P.R. Kyle, and M. Skov (1994), Volcanic activity and seismicity of Mount Erebus, 1986-1994, *Antarctic Journal of the U.S., 29*, 11-14.

Dibble, R.R., P.R. Kyle, and C.A. Rowe (2008), Video and seismic observations of Strombolian   eruptions at Erebus volcano, Antarctica, *J. Volcanol. Geotherm. Res.*, *177*, 619-634.

Edmonds, M., I.R. Sides, D. Swanson, C. Werner, R.S. Martin, T.A. Mather, R.A. Herd, R.L. Jones, M.I. Mead, and G. Sawyer (2013), Magma storage, transport and degassing during the 2008-10 summit eruption at Kilauea Volcano, Hawaii, *Geochem. Geophys. Geosys., in press.*

Eschenbacher, A.J. (1998), Pre-eruptive volatile contents of fractionating alkaline magma, Mount Erebus, Ross Island, Antarctica. Unpublished MSc thesis, New Mexico Institute of Mining and Technology, Socorro, NM.

Esser, R.P., P.R. Kyle, and W.C. McIntosh (2004), $^{40}Ar/^{39}Ar$ dating of the eruptive history of Mount Erebus, Antarctica: volcano evolution. *Bull. Volcanol., 66*, 671–686.

Favalli, M., A. Fornaciai, F. Mazzarini, A. Harris, M. Neri, B. Behncke, M.T. Pareschi, S. Tarquini, and E. Boschi (2010), Evolution of an active lava flow field using a multitemporal LIDAR acquisition, *J. Geophys. Res., 115,* B11203.

Finnegan, D.C., L.A. Stearns, G.S. Hamilton, and S. O'Neel (2010), Flow Characteristics of Tidewater Glaciers in Greenland and Alaska using Ground-based LiDAR, American Geophysical Union, *Fall Meeting 2010*, abstract #C21A-0515.

Finotello, M., A. Nyblade, J. Julia, D. Wiens, and S. Anandarkrishnan (2011), Crustal Vp-Vs ratios and thickness for Ross Island and the Transantarctic Mountain front, Antarctica, *Geophy. J. Int., 185(1)*, 85-92.

Francis, P., C. Oppenheimer, and D. Stevenson (1993), Endogenous growth of persistently active   volcanoes, *Nature, 366*, 554-557.

Gerst, A., M. Hort, R.C. Aster, J.B. Johnson, and P.R. Kyle (2013), The first second of volcano eruptions from the Erebus volcano lava lake, Antarctica – Energies, pressures, seismology, and infrasound. *J. Geophys. Res., 118,* 3318-3340.

Giggenbach, W., P. Kyle, and G. Lyon (1973), Present volcanic activity on Mt. Erebus, Ross Island, Antarctica, *Geology* , *1*, 135–156.

Gilbert, J.S., and S.J. Lane (2008), The consequences of fluid motion in volcanic conduits. In: Lane, S. J. and J.S. Gilbert (eds.), *Fluid Motions in Volcanic Conduits: A Source of Seismic and Acoustic Signals*, Geological Society, London, Special Publications, *307*, 1-10.

Gonnermann, H.M., and M. Michael (2007), The fluid mechanics inside a volcano, *Annu. Rev. Fluid Mech.*, *39*, 321-56.

Gudmundsson, A. (2007), Conceptual and numerical models of ring-fault formation, *J. Volcanol. Geotherm. Res., 116*, 142-160.

Gudmundsson, A. (2012), Magma chambers: Formation, local stresses, excess pressures, and compartments, *J. Volcanol. Geotherm. Res., 237-238*, 19-41.

Harpel, C.J., P.R. Kyle, R.P. Esser, W.C. McIntosh, and D.A. Caldwell (2004), [40]Ar/[39]Ar dating of the eruptive history of Mount Erebus, Antarctica: summit flows, tephra, and   caldera collapse, *Bull. Volcanol., 66*, 687-702.

Harris, A.J.L., L.P. Flynn, D.A. Rothery, C. Oppenheimer, and S.B. Sherman (1999), Mass flux measurements at active lava lakes: implications for magma recycling. *J. Geophys. Res, 104*, 7117–7136.

Harris, A.J.L., R. Carniel, and J. Jones (2005), Identification of variable convective regimes at Erta Ale Lava Lake, *J. Volcanol. Geotherm. Res., 142*, 207-223.

Hodgetts, D. (2013), Laser scanning and digital outcrop geology in the petroleum industry: A review, *Mar. Petrol. Geol., in press.*

Holohan, E.P., M.P.J. Schöpfer, and J.J. Walsh (2011), Mechanical and geometric controls on the structural evolution of pit crater and caldera subsidence, *J. Geophys. Res., 116,* B07202.

Hon, K., J. Kauahikaua, R. Denlinger, and K. Mackay (1994), Emplacement and inflation of pahoehoe sheet flows: Observations and measurements of active lava flows on Kilauea Volcano, Hawaii, *Geol. Soc. Amer. Bull., 106*, 351-370.

Huppert, H.E., and M.A. Hallworth (2007), Bi-directional flows in constrained systems, *J. Fluid Mech., 578*, 95-112.

InnovMetric, Inc. (2010). Polyworks v11.0. www.innovmetric.com.

Jaboyedoff, M., T. Oppikofer, A. Abellán, M.-H. Derron, A. Loye, R. Matzger, and A. Pedrazzini (2010), Use of LIDAR in landslide investigations: a review, *Nat. Hazards*, 1-24.

Jones, R.R., S. Kokkalas, and K.J.W. McCaffrey (2009), Quantitative analysis and visualization of non-planar fault surfaces using terrestrial laser-scanning (LiDAR) – The Arkitsa fault, central Greece, as a case study. *Geosphere, 5,* 465-482.

Kelly, P.J., N.W. Dunbar, P.R. Kyle, and W.C. McIntosh (2008a), Refinement of the late Quaternary geologic history of Erebus volcano, Antarctica using ^{40}Ar/^{39}Ar and ^{36}Cl age determinations, *J. Volcanol. Geotherm. Res., 177(3),* 569–577.

Kelly, P.J., P.R. Kyle, N.W. Dunbar, and K.W. Sims (2008b), Geochemistry and mineraology of the phonolite lava lake, Erebus volcano, Antarctica: 1972-2004 and comparison with older lavas, *J. Volc. Geotherm. Res., 177(3),* 589-605.

Kyle, P.R., and W. McIntosh (1978), Observations of volcanic activity at Mt. Erebus, 1978, *Antarctic J. of the U.S., 13*, 32-34.

Kyle, P.R., R.R. Dibble, W.F. Giggenbach, and J. Keys (1982), Volcanic activity associated with the anorthoclase phonolite lava lake, Mt. Erebus, Antarctica, In: C. Craddock (ed.), *Antarctic Geosciences*, University of Wisconsin Press, 735-745.

Kyle, P.R., J.A. Moore, and M.F. Thirlwall (1992), Petrologic evolution of anorthoclase phonolite lavas at Mount Erebus, Ross Island, Antarctica, *J. Petrol., 33*, 849-875.

Lichti, D.D., and S. Jamtsho (2006), Angular resolution of terrestrial laser scanners, *Photogramm. Rec., 21*, 141-160.

Lu, Z., D. Dzurisin, J. Biggs, C. Wicks Jr., and S. McNutt (2010), Ground surface deformation patterns, magma supply, and magma storage at Okmok volcano, Alaska, from InSAR analysis: 1. Intereruption deformation, 1997-2008, *J. Geophys. Res., 115,* B00B02.

Lyon, G.L., and W.F. Giggenbach (1974), Geothermal activity in Victoria Land, Antarctica, *New Zealand J. of Geol. And Geophys., 17*, 511-521.

McCaffrey, K.J., M. Wilkinson, G. Roberts, P.A. Cowie, R. Philips, R.J. Walters, S. Barba, L. La Rocca, E. Vittori, A. Blumetti, L. Guerrieri, F. Guzzetti, G. Lollino, S. Porfido, E. Esposito, L. Piccradi, P. Campedel, S. Cocco, G. Sileo, and A.M. Michetti (2009), Post-seismic slip on 6th April 2009 L'Aquila earthquake surface rupture, measured using a terrestrial laser scanner (tripod-mounted lidar), American Geophysical Union, *Fall Meeting 2009,* abstract #U23A-0023.

Molina, I., A. Burgisser, and C. Oppenheimer (2012), Numerical simulations of convection in crystal-bearing magmas: A case study of the magmatic system at Erebus, Antarctica, *J. Geophys. Res., 117*, B07209.

Murray, M.H., P.R. Kyle, R.C. Aster, and B. Bartel (2006). Continuous GPS measurement of deformation at Erebus Volcano, Antarctica. AGU Fall Mtg Abstract.

NASA Landsat Program, 1999, Landsat ETM+ scenes 06126520, 99962849, 67584342, 13426573, 50623353, 38783157, 89894477, 26856815, 60057154, 30452960, 19409237, 15897761, 12477400, 83252616, SLC-Off, USGS, Sioux Falls, 12/25/1999.

Oppenheimer, C., and P. Francis (1998), Implications of longeval lava lakes for geomorphological and plutonic processes at Erta 'Ale volcano, Afar*, J. Volcanol. Geotherm. Res., 80*, 101–111.

Oppenheimer, C., and P.R. Kyle (2008), Probing the magma plumbing of Erebus volcano, Antarctica, by open-path FTIR spectroscopy of gas emissions, *J. Volcanol. Geotherm. Res., 177*, 743–754.

Oppenheimer, C., A.J.S. McGonigle, P. Allard, M.J. Wooster, and V.I. Tsanev (2004), Sulfur, heat and magma budget of Erta 'Ale lava lake, Ethiopia, *Geology, 32*, 509-512.

Oppenheimer, C., A.S. Lomakina, P.R. Kyle, N.G. Kingsbury, and M. Boichu (2009), Pulsatory magma supply to a phonolite lava lake, *Earth Planet. Sci. Lett., 199*, 173–184.

Oppenheimer, C., R. Moretti, P.R. Kyle, A. Eschenbacher, J.B. Lowenstern, R.L. Hervig, and N.W. Dunbar (2011), Mantle to surface degassing of alkalic magmas at Erebus volcano, Antarctica, *J. Volcanol. Geotherm. Res.*, *306*, 261-271.

Optech (2009), ILRIS Summary Specification Sheet, http://www.optech.ca/pdf/ILRIS_SpecSheet_110309_Web.pdf , accessed on: 11/15/2009.

Otway, P.M., G.H. Blick, and B.J. Scott (1994), Volcanic deformation modeling of Mount Erebus: methods and results of geodetic surveys, 1980-1985, in: Kyle, P.R. (ed.), *Volcanological and Environmental Studies of Mount Erebus, Antarctica*, Antarctic Research Series, *66*, 57-68.

Pavez, A., D. Remy, S. Bonvalat, M. Diament, G. Gabalda, J.-L. Froger, P. Julien, D. Legrand, and D. Moisset (2006), Insight into ground deformations at Lascar volcano (Chile) from SAR interferometry, photogrammetry and GPS data: Implications on volcano dynamics and future space monitoring, *Remote Sens. Environ., 100,* 307-320.

Perroy, R.L., B. Bookhagen, G.P. Asner, and O.A. Chadwick (2010), Comparison of gully erosion estimates using airborne and ground-based LiDAR on Santa Cruz Island, California, *Geomorphology, 118,* 288-300.

Pesci, A., G. Teza, and G. Ventura (2008), Remote sensing of volcanic terrains by terrestrial laser scanner: preliminary reflectance and RGB implications for studying Vesuvius crater (Italy), *Ann. Geophys., 51,* 633-653.

Pesci, A., G. Teza, and E. Bonali (2011), Terrestrial laser scanner resolution: numerical simulations and experiments on spatial sampling optimization, *Remote Sens., 3*, 167-184.

Petrie, G., and C.K. Toth (2008), Introduction to laser ranging, profiling, and scanning, in: Shan, J., and C.K. Toth (eds.), *Topographic Laser Ranging and Scanning: principles and processing*, CRC Press, Taylor & Francis, 590 pp.

Pinkerton, H., L. Wilson, and R. Macdonald (2002), The transport and eruption of magma from volcanoes: a review, *Contemp. Phys.,43*, 197-210.

Puglisi, G., A. Bonforte, and S.R. Maugeri (2001), Ground deformation patterns on Mt. Etna, 1992 to 1994, inferred from GPS data, *Bull. Volcanol., 62*, 371-384.

Salvini, R., M. Francioni, F. Riccucci, and I. Callegari (2013), Photogrammetry and laser scanning for analyzing slope stability and rock fall runout along the Domodossola-Iselle railway, the Italian Alps, *Geomorphology, 185*, 110-122.

Shackleton, E.H. (1908), Aurora Australis - The British Antarctic Expedition, 1907–1909.

Sims, K.W.W., J. Blichert-Toft, P.R. Kyle, S. Pichat, P.-J. Gauthier, J. Blusztajn, P. Kelly, L. Ball, and L. Graham (2008), A Sr, Nd, Hf, Pb, isotope perspective on the genesis and long-term evolution of alkaline magmas from Erebus Volcano, Antarctica, *J. Volcanol. Geotherm. Res.*, *177*, 606-618.

Smithsonian Institution (2013), Erebus, *Global Volcanism Network.*

Sparks, R.S.J. (1978), The dynamics of bubble formation and growth in magmas: A review and analysis, *J. Volcanol. Geotherm. Res.*, *3*, 1-37.

Sparks, R.S.J. (2003), Dynamics of magma degassing, In: C. Oppenheimer, D.M. Pyle and J. Barclay (eds.), *Volcanic Degassing: Special Publications*, Geological Society, London, 5-22.

Swanson, D.A., W.A. Duffield, D.B. Jackson, and D.W. Peterson (1972), The complex filling of Alea crater, Kileauea volcano, *Hawaii. Bull. Volcanol. , 36*, 105–126.

Sweeney, D., P.R. Kyle, and C. Oppenheimer (2008), Sulfur dioxide emissions and degassing behavior of Erebus volcano, Antarctica, *J. Volcanol. Geotherm. Res., 177,* 725-733.

Tazieff, H. (1994), Permanent lava lakes-observed facts and induced mechanisms, *J. Volcanol. Geotherm. Res., 63*, 3–11.

Tilling, R.I. (1987), Fluctuations in surface height of active lava lakes during 1972–1974 Mauna   Ulu Eruption, Kilauea Volcano, Hawaii. *J. Geophys. Res., 92*, 13721–13730.

Wardell, L.J., P.R. Kyle, and C. Chaffin (2004), Carbon dioxide and carbon monoxide emission rates from an alkaline intra-plate volcano: Mt. Erebus, Antarctica, *J. Volcanol. Geotherm. Res.*, *131*, 109-121.

Watson, T., A. Nyblade, D.A. Wiens, S. Anandakrishnan, M. Benoit, P.J. Shore, D. Voigt, and J. VanDecar (2006), P and S velocity structure of the upper mantle beneath the Transantarctic Mountains, East Antarctic craton, and Ross Sea from travel time tomography, *Geochem. Geophys. Geosys., 7*, 1–17.

Witham, F., and E.W. Llewellin (2006), Stability of lava lakes, *J. Volcanol. Geotherm. Res.*, *158*, 321-332.

Witham, F., A.W. Woods, and C. Gladstone (2006), An analogue experiment model of depth fluctuations in lava lakes, *Bull. Volcanol., 69*, 51-56.

Woods, A.W., and H.E. Hubbert (2003), On magma chamber evolution during slow effusive eruptions, *j. Geophys. Res., 108*, B82043.

Wright, R., and E. Pilger (2008), Satellite observations reveal little inter-annual variability in the radiant flux from the Mount Erebus lava lake, *J. Volcanol. Geotherm. Res., 177,* 687-694.

Young, A.P., M.J. Olsen, N. Driscoll, R.E. Flick, R. Gutierrez, R.T. Guza, E. Johnstone, and F. Kuester (2010), Comparison of Airborne and Terrestrial Estimates of Seacliff Erosion in Southern California, *Amer. Soc. Photogramm. Rem. Sens., 76*, 421-427.

Zandomeneghi, D., R. Aster, P. Kyle, A. Barclay, J. Chaput, and H. Knox (2013), Internal structure of Erebus volcano, Antarctica imaged by high-resolution active-source seismic tomography and coda interferometry, *J. Geophys. Res., 118*, 1067-1078.

Zhu, L., Y. Mu, and R. Shi (2008), Study on the resolution of laser scanner point cloud, in: *Proceedings of 2008 IEEE International Geoscience & Remote Sensing Symposium*, July 2008, Boston, MA, USA, vol.2, *IEEE*, Piscataway, NJ, USA, 1136-1139.

Zreda-Gostynska, G., P.R. Kyle, D. Finnegan, and K.M. Prestbo (1997), Volcanic gas emissions from Mount Erebus and their impact on the Antarctic environment. *J. Geophys. Res., 102*, 15039–15055.

APPENDIX A – Root-Mean-Square (RMS) Error Analysis

The Root-Mean-Square Errors (RMSE) for all the lidar scans were derived from "check points" – 0.5x0.5m (inactive) areas along Main Crater and Inner Crater walls which were scanned repeatedly over the total scanning period. The "inactive" areas were sections of the wall that were chosen because they were: 1) Relatively flat with no dramatic dip changes, 2) Had different levels of intensity (in order to measure the error over different types of surfaces) and 3) Displayed minimal change (<10cm) over the 3 years of scanning and no change (<5cm) over the current year's scans. The resulting x, y and z measurements were then extracted and the RMSE calculation was performed in Excel. In this study we are making the assumption that if the measurements were perfect (i.e. had 0 measurement error) that there would be no variability observed within these areas.

Computationally, RMSE is the square root of the mean of the squares of the residuals – the residuals being the difference between the predicted and actual values. In many lidar surveys the "predicted" values are those measured by a GPS on the ground, however in our surveys GPS measurements of the crater were impossible due to active nature of the volcano (and the inherent safety risks which come with it). Instead the "predicted" value used was the average at the check point, making the residual the standard deviation of all the measurements at that check point. 5 check points in total were extracted and analyzed – 2 check points on the Inner Crater Wall and 3 points on the Main Crater Wall. This error analysis is meant to define the error in the measurement derived from the scanner itself - unfortunately this check point scanning was only performed during the 2009 field season.

See the table and graphs below for a summary of the RMSE calculations:

	RMSE (X)	RMSE (Y)	RMSE (Z)
Check Point #1:	3.59 cm	3.32 cm	2.08 cm
Check Point #2:	3.84 cm	3.91 cm	2.71 cm
Check Point #3:	4.89 cm	2.39 cm	1.77 cm
Check Point #4:	3.58 cm	3.03 cm	1.95 cm
Check Point #5:	3.83 cm	3.41 cm	1.84 cm

Average RMSE (X)	Average RMSE (Y)	Average RMSE (Z)
3.98 cm	3.25 cm	2.10

Distribution of Error - Check Point #2

Distribution of Error - Check Point #3

Distribution of Error - Check Point #4

Distribution of Error - Check Point #5
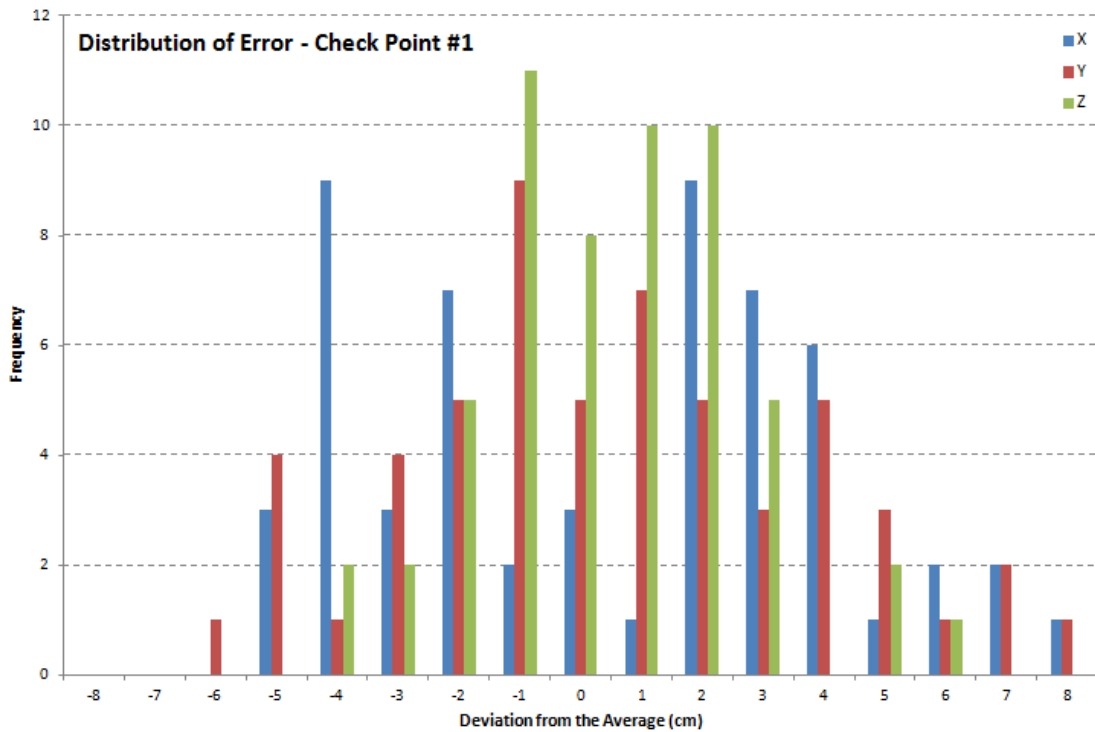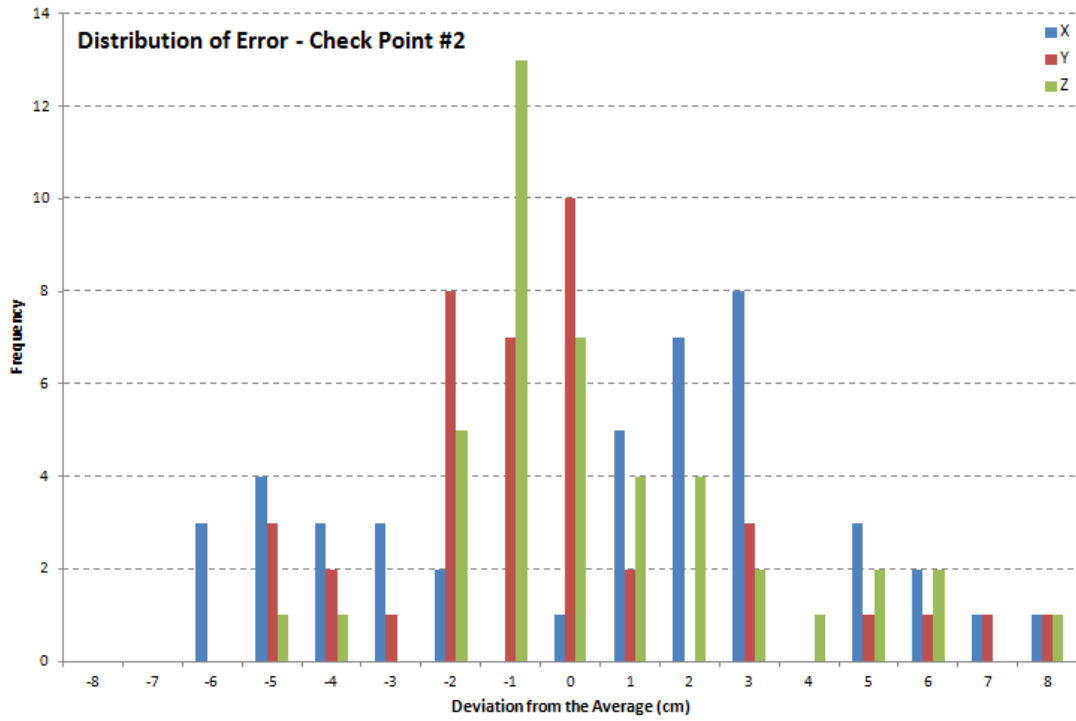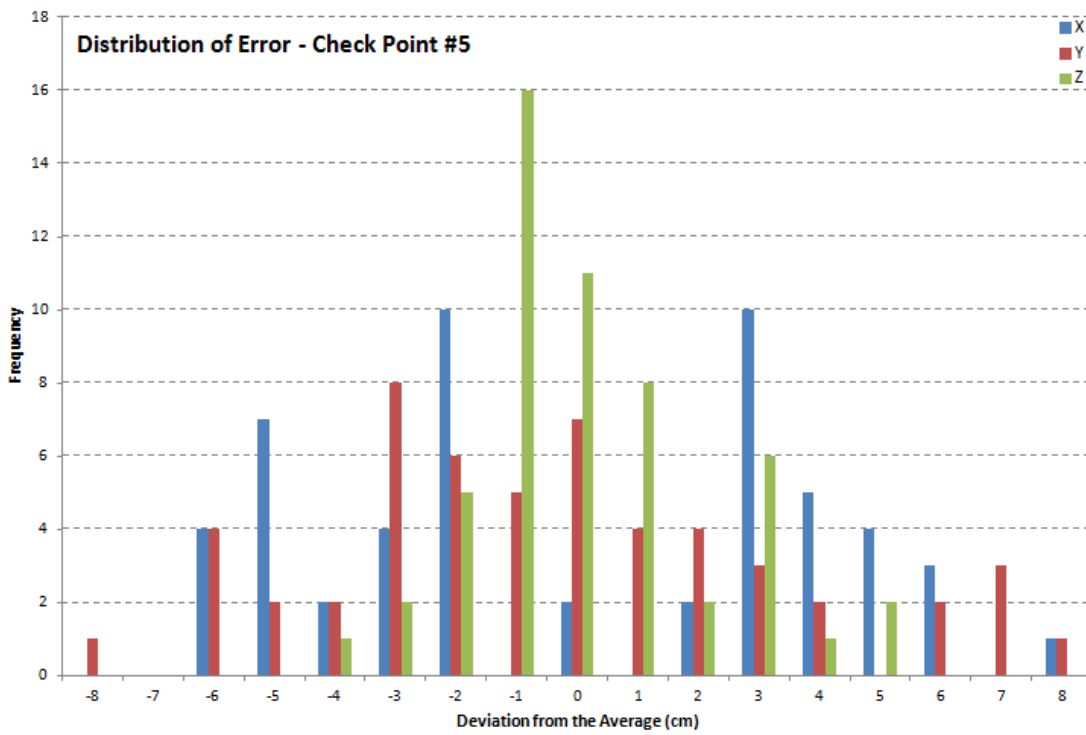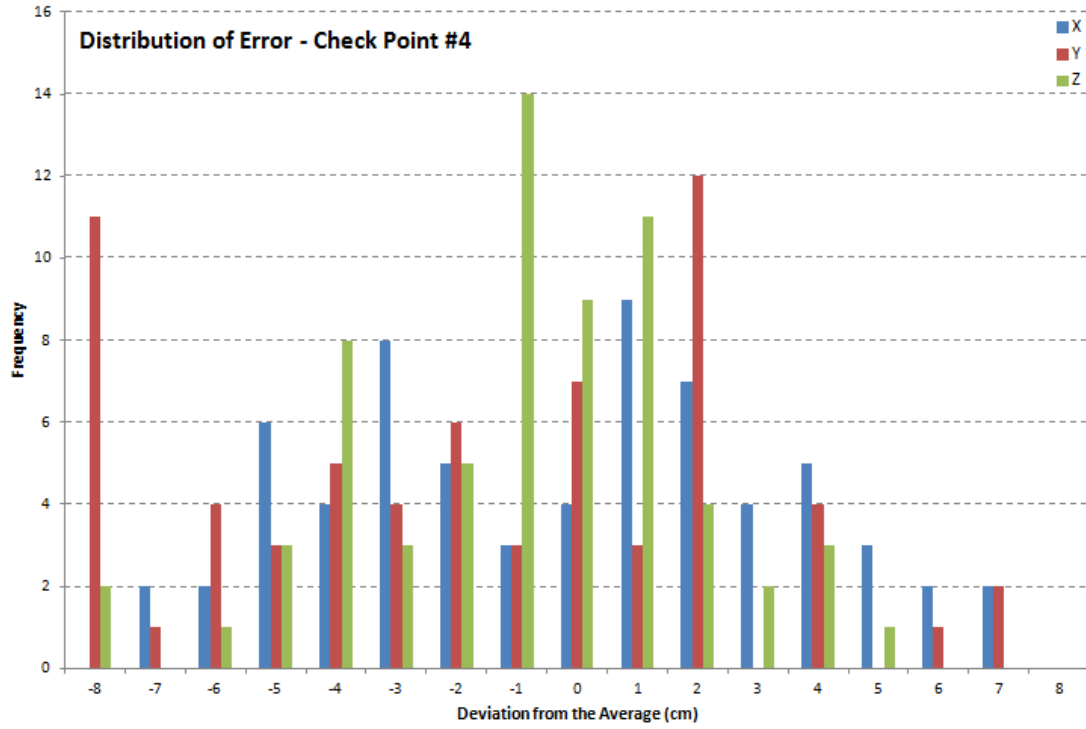
APPENDIX B – Validation of Lava Lake Time Series Sampling

The optimal sampling scheme was determined through the gridding of the lava lakes – starting with a 2x2m grid and then progressing upward in 2m increments until an adequately sampled time series could be extracted. As was mentioned in the text – "the smallest possible sampling region was chosen which was adequately sampled (both spatially and temporally) for an accurate time series." In the 2009 dataset an 8x8m grid was required and only 2 regions were able to be extracted, whereas in the 2010 dataset a 2x2m grid was adequate and almost every grid point could have been extracted – the areas that were extracted were simply chosen based on location, a point in the center of the lake and to the North, South, East and West.

Below is a graph of the raw data extracted from the 2009 lava lake point cloud (Point A – see Figure 3), using a 2x2m, 4x4m and 8x8m extraction area. Both the 2x2 and 4x4m extractions show inadequate sampling of the data which resulted in the inaccurate reconstruction of the lake level (i.e. the truncation of several peaks and troughs). The 8x8m extraction area was required to produce an accurate time series.

2009 Lava Lake Survey - Raw Extracted Data
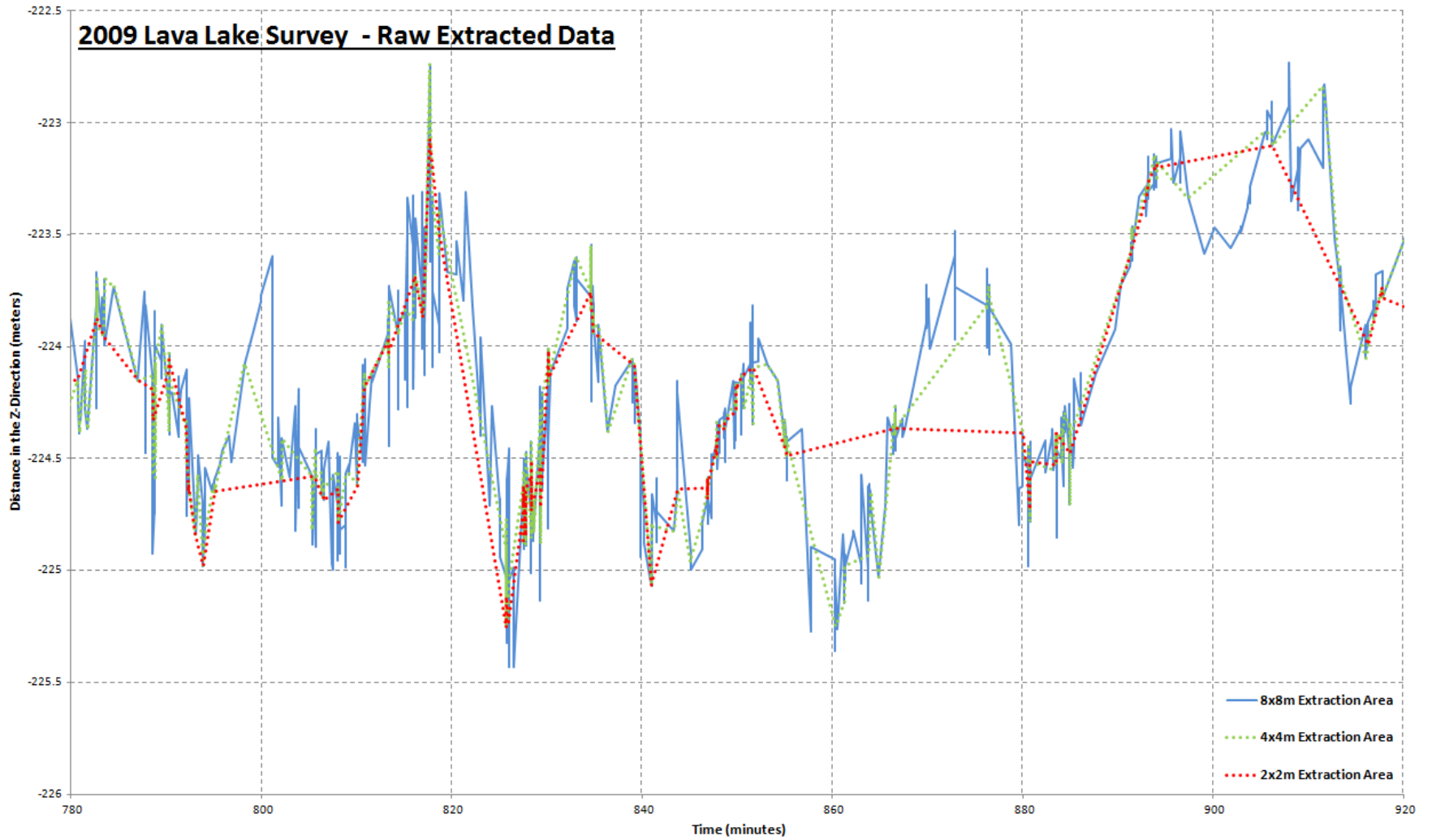
APPENDIX C – Optech ILRIS-3D Parsing Logs and Alignment Statistics

The raw scanner data was initially processed, using the Optech ILRIS-3D Parser, from the original ".i3d" output into an output format that could easily be used for time series analysis (ASCII XYZ format) and could be recognized by the PolyWorks program that was used for the point cloud alignment, visualization and analysis (.pf, PolyWorks PIF format). Also output with the data file is a bitmap image of the scanned area (taken by the Optech ILRIS-3D's internal camera) and a text file ("parsing log") which contains information regarding the scanner settings and Parser settings (see the ILRIS-3D operating manual for further information – which can be found at: http://facility.unavco.org/kb/categories/Geodetic+Imaging/Terrestrial+Laser+Scanning+%28TLS%29/Optech/). The parsing logs of the Erebus crater and lava lake scans were included in this appendix for reference.

Also, a summary of alignment statistics (from the scan alignments performed in the PolyWorks program) between the ALS scans from 2001 and TLS scans from 2008, 2009 and 2010 can be found in the attached CD. Included with the statistics summary is also a histogram of alignment errors for each scan, which will give a sense of the order of magnitude of the errors seen from the alignment process.

C.1   2008 Lava Lake Scan

```
Parser version:                        5.0.1.4
Name of scan project:                  G-081_LAVALAKE_1_Q_346
Time stamp:                            Wed Dec 17 08:20:01 2008 (UTC,1229502001)
Horizontal angle resolution(uRad):     20
Vertical angle resolution(uRad):       20
Meta header version:                   3
Unit title:                            ILRIS-3D
Unit serial number:                    SN010300
Unit software version:                 4.4.10-7B
Controller ID:                         scanner
Controller version:


GRP point:                             (0.000000, 0.000000, 0.000000)

Number of shots:                       30814
Number of scan lines:                  142
Number of points per line:             217
Number of loops:                       400
Scan task mode:                        scan
Scan task id:                          156
Pulse mode:                            Last Pulse
Scan pattern:                          Step Stare
Shot type:                             Shot I3D
Scan start position:                   Lower Left
Scan orientation:                      Horizontal
Scan in ER mode:                       Yes
Roi id:                                156
Roi start point:                       (-16.140083,-14.671692)
Roi stop point:                        (  1.492949, -3.180504)
Scan average range(m):                  260.15
X spot spacing(counts/mm):              71/369.4
Y spot spacing(counts/mm):              71/369.4


Applies asc correction:                Yes
Trims shot Data:                       No (0)
Applies ric correction:                Yes
Smoothes polar shot data:              No
Reduces shot data:                     No
Model-transforms shots:                Yes
Applies pan-tilt correction:           No
Removes outliers:                      No
Smoothes Cartesian shot points:        No
Moves Cartesian origin:                Yes
Range-dynamically scales intensity:    Yes
Scale intensity range(M):              50.0
```

C.2 2009 Lava Lake Scan

```
Parser version:                      5.0.1.4
Name of scan project:                20091216_lake01
Time stamp:                          Wed Dec 16 12:44:10 2009 (UTC,1260967450)
Horizontal angle resolution(uRad):   20
Vertical angle resolution(uRad):     20
Meta header version:                 3
Unit title:                          ILRIS-3D
Unit serial number:                  SN010300
Unit software version:               4.4.10-7B
Controller ID:                       CntrlWin
Controller version:                  4.3.5.4



GRP point:                           (0.000000, 0.000000, 0.000000)

Number of shots:                     10665
Number of scan lines:                45
Number of points per line:           237
Number of loops:                     1000
Scan task mode:                      scan
Scan task id:                        112
Pulse mode:                          Last Pulse
Scan pattern:                        Step Stare
Shot type:                           Shot I4D
Scan start position:                 Lower Left
Scan orientation:                    Horizontal
Scan in ER mode:                     Yes
Roi id:                              112
Roi start point:                     ( -0.080204, -7.647781)
Roi stop point:                      ( 17.800697,  5.725330)
Scan average range(m):                107.53
X spot spacing(counts/mm):            66/141.9
Y spot spacing(counts/mm):            66/141.9
Pan angle (degrees):                  0.000000
Tilt angle (degrees):                 -40.000000


Applies asc correction:              No
Trims shot Data:                     Yes (5)
Applies ric correction:              Yes
Smoothes polar shot data:            No
Reduces shot data:                   No
Model-transforms shots:              Yes
Applies pan-tilt correction:         Yes
Removes outliers:                    Yes
Smoothes Cartesian shot points:      No
Moves Cartesian origin:              Yes
Range-dynamically scales intensity:  Yes
Scale intensity range(M):            50.0
```

C.3   *2010 Lava Lake Scan*

```
Parser version:                      5.0.2.5
Name of scan project:                20101215_lake02
Time stamp:                          Wed Dec 15 02:20:08 2010 (UTC,1292379608)
Horizontal angle resolution(uRad):   20
Vertical angle resolution(uRad):     20
Meta header version:                 3
Unit title:                          ILRIS-3D
Unit serial number:                  SN010300
Unit software version:               4.4.18-7B
Controller ID:                       Cntrlwin-eth
Controller version:                  5.1.0.1



GRP point:                           (0.000000, 0.000000, 0.000000)

Number of shots:                     6201
Number of scan lines:                39
Number of points per line:           159
Number of loops:                     500
Scan task mode:                      scan
Scan task id:                        101
Pulse mode:                          Last Pulse
Scan pattern:                        Step Stare
Shot type:                           Shot I4D
Scan start position:                 Lower Left
Scan orientation:                    Horizontal
Scan in ER mode:                     Yes
Roi id:                              101
Roi start point:                     ( -2.842408,-14.229107)
Roi stop point:                      (  8.040319, -2.527248)
Scan average range(m):                306.81
X spot spacing(counts/mm):            60/368.2
Y spot spacing(counts/mm):            60/368.2
Pan angle (degrees):                  0.000000
Tilt angle (degrees):                 -35.000000


Applies asc correction:              No
Trims shot Data:                     No (0)
Applies ric correction:              Yes
Smoothes polar shot data:            No
Reduces shot data:                   No
Model-transforms shots:              Yes
Applies pan-tilt correction:         Yes
Removes outliers:                    Yes
Smoothes Cartesian shot points:      No
Moves Cartesian origin:              Yes
Range-dynamically scales intensity:  Yes
Scale intensity range(M):            50.0
```

C.4 2010 Main Crater Scans

```
Parser version:                      5.0.2.5
Name of scan project:                20101210-crater01\
Time stamp:                          Thu Dec 09 23:16:31 2010 (UTC,1291936591)
Horizontal angle resolution(uRad):   20
Vertical angle resolution(uRad):     20
Meta header version:                 3
Unit title:                          ILRIS-3D
Unit serial number:                  SN010300
Unit software version:               4.4.18-7B
Controller ID:                       Cntrlwin
Controller version:                  5.1.0.1



GRP point:                           (0.000000, 0.000000, 0.000000)

Number of shots:                     1482217
Number of scan lines:                1397
Number of points per line:           1061
Number of loops:                     2
Scan task mode:                      scan
Scan task id:                        110
Pulse mode:                          Last Pulse
Scan pattern:                        Step Stare
Shot type:                           Shot I4D
Scan start position:                 Lower Left
Scan orientation:                    Horizontal
Scan in ER mode:                     Yes
Roi id:                              110
Roi start point:                     (-10.377502,-20.000000)
Roi stop point:                      ( 20.000000, 20.000000)
Scan average range(m):                67.43
X spot spacing(counts/mm):            25/33.7
Y spot spacing(counts/mm):            25/33.7
Pan angle (degrees):                 -72.000061
Tilt angle (degrees):                -10.000000

Number of shots:                     1951609
Number of scan lines:                1397
Number of points per line:           1397
Number of loops:                     2
Scan task mode:                      scan
Scan task id:                        111
Pulse mode:                          Last Pulse
Scan pattern:                        Step Stare
Shot type:                           Shot I4D
Scan start position:                 Lower Left
Scan orientation:                    Horizontal
Scan in ER mode:                     Yes
Roi id:                              111
Roi start point:                     (-20.000000,-20.000000)
Roi stop point:                      ( 20.000000, 20.000000)
Scan average range(m):                236.36
X spot spacing(counts/mm):            25/118.2
Y spot spacing(counts/mm):            25/118.2
Pan angle (degrees):                 -36.000031
Tilt angle (degrees):                -10.000000
```

```
Number of shots:                       1951609
Number of scan lines:                  1397
Number of points per line:             1397
Number of loops:                       2
Scan task mode:                        scan
Scan task id:                          112
Pulse mode:                            Last Pulse
Scan pattern:                          Step Stare
Shot type:                             Shot I4D
Scan start position:                   Lower Left
Scan orientation:                      Horizontal
Scan in ER mode:                       Yes
Roi id:                                112
Roi start point:                       (-20.000000,-20.000000)
Roi stop point:                        ( 20.000000, 20.000000)
Scan average range(m):                 5526.55
X spot spacing(counts/mm):             25/2763.3
Y spot spacing(counts/mm):             25/2763.3
Pan angle (degrees):                   0.000000
Tilt angle (degrees):                  -10.000000

Number of shots:                       1951609
Number of scan lines:                  1397
Number of points per line:             1397
Number of loops:                       2
Scan task mode:                        scan
Scan task id:                          113
Pulse mode:                            Last Pulse
Scan pattern:                          Step Stare
Shot type:                             Shot I4D
Scan start position:                   Lower Left
Scan orientation:                      Horizontal
Scan in ER mode:                       Yes
Roi id:                                113
Roi start point:                       (-20.000000,-20.000000)
Roi stop point:                        ( 20.000000, 20.000000)
Scan average range(m):                 -1.#J
X spot spacing(counts/mm):             25/-1.$
Y spot spacing(counts/mm):             25/-1.$
Pan angle (degrees):                   36.000031
Tilt angle (degrees):                  -10.000000

Number of shots:                       1810512
Number of scan lines:                  1397
Number of points per line:             1296
Number of loops:                       2
Scan task mode:                        scan
Scan task id:                          114
Pulse mode:                            Last Pulse
Scan pattern:                          Step Stare
Shot type:                             Shot I4D
Scan start position:                   Lower Left
Scan orientation:                      Horizontal
Scan in ER mode:                       Yes
Roi id:                                114
Roi start point:                       (-20.000000,-20.000000)
Roi stop point:                        ( 17.112007, 20.000000)
Scan average range(m):                 8753.10
X spot spacing(counts/mm):             25/4376.6
Y spot spacing(counts/mm):             25/4376.6
Pan angle (degrees):                   72.000061
Tilt angle (degrees):                  -10.000000


Applies asc correction:                No
Trims shot Data:                       No (0)
Applies ric correction:                Yes
Smoothes polar shot data:              No
Reduces shot data:                     No
Model-transforms shots:                Yes
Applies pan-tilt correction:           Yes
Removes outliers:                      Yes
Smoothes Cartesian shot points:        No
Moves Cartesian origin:                Yes
Range-dynamically scales intensity:    Yes
Scale intensity range(M):              50.0
```

- - - - - - - - - -


```
Parser version:                       5.0.2.5
Name of scan project:                 20101214_crater03
Time stamp:                           Tue Dec 14 00:37:53 2010 (UTC,1292287073)
Horizontal angle resolution(uRad):    20
Vertical angle resolution(uRad):      20
Meta header version:                  3
Unit title:                           ILRIS-3D
Unit serial number:                   SN010300
Unit software version:                4.4.18-7B
Controller ID:                        Cntrlwin-eth
Controller version:                   5.0.0.4



GRP point:                            (0.000000, 0.000000, 0.000000)

Number of shots:                      1842643
Number of scan lines:                 1397
Number of points per line:            1319
Number of loops:                      2
Scan task mode:                       scan
Scan task id:                         119
Pulse mode:                           Last Pulse
Scan pattern:                         Step Stare
Shot type:                            Shot I3D
Scan start position:                  Lower Left
Scan orientation:                     Horizontal
Scan in ER mode:                      Yes
Roi id:                               119
Roi start point:                      (-17.762470,-19.972176)
Roi stop point:                       ( 20.000000, 20.024414)
Scan average range(m):                 131.08
X spot spacing(counts/mm):             25/65.5
Y spot spacing(counts/mm):             25/65.5
Pan angle (degrees):                  -36.000031
Tilt angle (degrees):                 -35.024414
```

```
Number of shots:                    1951609
Number of scan lines:               1397
Number of points per line:          1397
Number of loops:                    2
Scan task mode:                     scan
Scan task id:                       120
Pulse mode:                         Last Pulse
Scan pattern:                       Step Stare
Shot type:                          Shot I3D
Scan start position:                Lower Left
Scan orientation:                   Horizontal
Scan in ER mode:                    Yes
Roi id:                             120
Roi start point:                    (-20.000000,-19.972176)
Roi stop point:                     ( 20.000000, 20.024414)
Scan average range(m):               246.79
X spot spacing(counts/mm):           25/123.4
Y spot spacing(counts/mm):           25/123.4
Pan angle (degrees):                 0.000000
Tilt angle (degrees):               -35.024414

Number of shots:                    1951609
Number of scan lines:               1397
Number of points per line:          1397
Number of loops:                    2
Scan task mode:                     scan
Scan task id:                       121
Pulse mode:                         Last Pulse
Scan pattern:                       Step Stare
Shot type:                          Shot I3D
Scan start position:                Lower Left
Scan orientation:                   Horizontal
Scan in ER mode:                    Yes
Roi id:                             121
Roi start point:                    (-20.000000,-19.972176)
Roi stop point:                     ( 20.000000, 20.024414)
Scan average range(m):               274.75
X spot spacing(counts/mm):           25/137.4
Y spot spacing(counts/mm):           25/137.4
Pan angle (degrees):                 36.000031
Tilt angle (degrees):               -35.024414

Number of shots:                    1121791
Number of scan lines:               1397
Number of points per line:          803
Number of loops:                    2
Scan task mode:                     scan
Scan task id:                       122
Pulse mode:                         Last Pulse
Scan pattern:                       Step Stare
Shot type:                          Shot I3D
Scan start position:                Lower Left
Scan orientation:                   Horizontal
Scan in ER mode:                    Yes
Roi id:                             122
Roi start point:                    (-20.000000,-19.972176)
Roi stop point:                     (  2.976555, 20.024414)
Scan average range(m):               184.17
X spot spacing(counts/mm):           25/92.1
Y spot spacing(counts/mm):           25/92.1
Pan angle (degrees):                 72.000061
Tilt angle (degrees):               -35.024414
```

```
Applies asc correction:              Yes
Trims shot Data:                     No (0)
Applies ric correction:              Yes
Smoothes polar shot data:            No
Reduces shot data:                   No
Model-transforms shots:              Yes
Applies pan-tilt correction:         Yes
Removes outliers:                    Yes
Smoothes Cartesian shot points:      No
Moves Cartesian origin:              Yes
Range-dynamically scales intensity:  Yes
Scale intensity range(M):            50.0
```

- - - - - - - - - -

```
Parser version:                      5.0.2.5
Name of scan project:                20101215_crater04
Time stamp:                          Wed Dec 15 08:18:12 2010 (UTC,1292401092)
Horizontal angle resolution(uRad):   20
Vertical angle resolution(uRad):     20
Meta header version:                 3
Unit title:                          ILRIS-3D
Unit serial number:                  SN010300
Unit software version:               4.4.18-7B
Controller ID:                       CntrlWin-eth
Controller version:                  5.1.0.1


GRP point:                           (0.000000, 0.000000, 0.000000)

Number of shots:                     1171240
Number of scan lines:                890
Number of points per line:           1316
Number of loops:                     2
Scan task mode:                      scan
Scan task id:                        119
Pulse mode:                          Last Pulse
Scan pattern:                        Step Stare
Shot type:                           Shot I4D
Scan start position:                 Lower Left
Scan orientation:                    Horizontal
Scan in ER mode:                     Yes
Roi id:                              119
Roi start point:                     (-17.700129,-19.882309)
Roi stop point:                      ( 20.000000,  5.601229)
Scan average range(m):               367.69
X spot spacing(counts/mm):           25/183.8
Y spot spacing(counts/mm):           25/183.8
Pan angle (degrees):                 0.000000
Tilt angle (degrees):                0.000000
```

```
Number of shots:                    1243330
Number of scan lines:               890
Number of points per line:          1397
Number of loops:                    2
Scan task mode:                     scan
Scan task id:                       120
Pulse mode:                         Last Pulse
Scan pattern:                       Step Stare
Shot type:                          Shot I4D
Scan start position:                Lower Left
Scan orientation:                   Horizontal
Scan in ER mode:                    Yes
Roi id:                             120
Roi start point:                    (-20.000000,-19.882309)
Roi stop point:                     ( 20.000000,  5.601229)
Scan average range(m):               401.70
X spot spacing(counts/mm):           25/200.9
Y spot spacing(counts/mm):           25/200.9
Pan angle (degrees):                 36.000031
Tilt angle (degrees):                0.000000

Number of shots:                    1168570
Number of scan lines:               890
Number of points per line:          1313
Number of loops:                    2
Scan task mode:                     scan
Scan task id:                       121
Pulse mode:                         Last Pulse
Scan pattern:                       Step Stare
Shot type:                          Shot I4D
Scan start position:                Lower Left
Scan orientation:                   Horizontal
Scan in ER mode:                    Yes
Roi id:                             121
Roi start point:                    (-20.000000,-19.882309)
Roi stop point:                     ( 17.604996,  5.601229)
Scan average range(m):               252.97
X spot spacing(counts/mm):           25/126.5
Y spot spacing(counts/mm):           25/126.5
Pan angle (degrees):                 72.000061
Tilt angle (degrees):                0.000000


Applies asc correction:             No
Trims shot Data:                    No (0)
Applies ric correction:             Yes
Smoothes polar shot data:           No
Reduces shot data:                  No
Model-transforms shots:             Yes
Applies pan-tilt correction:        Yes
Removes outliers:                   Yes
Smoothes Cartesian shot points:     No
Moves Cartesian origin:             Yes
Range-dynamically scales intensity: Yes
Scale intensity range(M):           50.0
```

- - - - - - - - - -

```
Parser version:                        5.0.2.5
Name of scan project:                  20101217_crater05
Time stamp:                            Fri Dec 17 02:17:51 2010 (UTC,1292552271)
Horizontal angle resolution(uRad):     20
Vertical angle resolution(uRad):       20
Meta header version:                   3
Unit title:                            ILRIS-3D
Unit serial number:                    SN010300
Unit software version:                 4.4.18-7B
Controller ID:                         CntrlWin-eth
Controller version:                    5.1.0.1


GRP point:                             (0.000000, 0.000000, 0.000000)

Number of shots:                       1838452
Number of scan lines:                  1397
Number of points per line:             1316
Number of loops:                       2
Scan task mode:                        scan
Scan task id:                          103
Pulse mode:                            Last Pulse
Scan pattern:                          Step Stare
Shot type:                             Shot I3D
Scan start position:                   Lower Left
Scan orientation:                      Horizontal
Scan in ER mode:                       Yes
Roi id:                                103
Roi start point:                       (-17.698212,-19.996586)
Roi stop point:                        ( 20.000000, 20.000000)
Scan average range(m):                  169.59
X spot spacing(counts/mm):              25/84.8
Y spot spacing(counts/mm):              25/84.8
Pan angle (degrees):                   -36.000031
Tilt angle (degrees):                  -35.000000

Number of shots:                       1951609
Number of scan lines:                  1397
Number of points per line:             1397
Number of loops:                       2
Scan task mode:                        scan
Scan task id:                          104
Pulse mode:                            Last Pulse
Scan pattern:                          Step Stare
Shot type:                             Shot I3D
Scan start position:                   Lower Left
Scan orientation:                      Horizontal
Scan in ER mode:                       Yes
Roi id:                                104
Roi start point:                       (-20.000000,-19.996586)
Roi stop point:                        ( 20.000000, 20.000000)
Scan average range(m):                  257.39
X spot spacing(counts/mm):              25/128.7
Y spot spacing(counts/mm):              25/128.7
Pan angle (degrees):                    0.000000
Tilt angle (degrees):                  -35.000000
```

```
Number of shots:                        1825879
Number of scan lines:                   1397
Number of points per line:              1307
Number of loops:                        2
Scan task mode:                         scan
Scan task id:                           105
Pulse mode:                             Last Pulse
Scan pattern:                           Step Stare
Shot type:                              Shot I3D
Scan start position:                    Lower Left
Scan orientation:                       Horizontal
Scan in ER mode:                        Yes
Roi id:                                 105
Roi start point:                        (-20.000000,-19.996586)
Roi stop point:                         ( 17.435501, 20.000000)
Scan average range(m):                   118.64
X spot spacing(counts/mm):               25/59.3
Y spot spacing(counts/mm):               25/59.3
Pan angle (degrees):                     36.000031
Tilt angle (degrees):                   -35.000000


Applies asc correction:                 Yes
Trims shot Data:                        No (0)
Applies ric correction:                 Yes
Smoothes polar shot data:               No
Reduces shot data:                      No
Model-transforms shots:                 Yes
Applies pan-tilt correction:            Yes
Removes outliers:                       Yes
Smoothes Cartesian shot points:         No
Moves Cartesian origin:                 Yes
Range-dynamically scales intensity:     Yes
Scale intensity range(M):               50.0




- - - - - - - - - -




Parser version:                         5.0.2.5
Name of scan project:                   20101217_crater06
Time stamp:                             Fri Dec 17 04:34:03 2010 (UTC,1292560443)
Horizontal angle resolution(uRad):      20
Vertical angle resolution(uRad):        20
Meta header version:                    3
Unit title:                             ILRIS-3D
Unit serial number:                     SN010300
Unit software version:                  4.4.18-7B
Controller ID:                          Cntrlwin-eth
Controller version:                     5.1.0.1
```

```
GRP point:                          (0.000000, 0.000000, 0.000000)

Number of shots:                    1331180
Number of scan lines:               1010
Number of points per line:          1318
Number of loops:                    2
Scan task mode:                     scan
Scan task id:                       130
Pulse mode:                         Last Pulse
Scan pattern:                       Step Stare
Shot type:                          Shot I3D
Scan start position:                Lower Left
Scan orientation:                   Horizontal
Scan in ER mode:                    Yes
Roi id:                             130
Roi start point:                    (-17.741562,-19.460917)
Roi stop point:                     ( 20.000000,  9.465185)
Scan average range(m):               178.20
X spot spacing(counts/mm):           25/89.1
Y spot spacing(counts/mm):           25/89.1
Pan angle (degrees):                -72.000061
Tilt angle (degrees):                0.000000

Number of shots:                    1410970
Number of scan lines:               1010
Number of points per line:          1397
Number of loops:                    2
Scan task mode:                     scan
Scan task id:                       131
Pulse mode:                         Last Pulse
Scan pattern:                       Step Stare
Shot type:                          Shot I3D
Scan start position:                Lower Left
Scan orientation:                   Horizontal
Scan in ER mode:                    Yes
Roi id:                             131
Roi start point:                    (-20.000000,-19.460917)
Roi stop point:                     ( 20.000000,  9.465185)
Scan average range(m):               448.28
X spot spacing(counts/mm):           25/224.1
Y spot spacing(counts/mm):           25/224.1
Pan angle (degrees):                -36.000031
Tilt angle (degrees):                0.000000

Number of shots:                    1410970
Number of scan lines:               1010
Number of points per line:          1397
Number of loops:                    2
Scan task mode:                     scan
Scan task id:                       132
Pulse mode:                         Last Pulse
Scan pattern:                       Step Stare
Shot type:                          Shot I3D
Scan start position:                Lower Left
Scan orientation:                   Horizontal
Scan in ER mode:                    Yes
Roi id:                             132
Roi start point:                    (-20.000000,-19.460917)
Roi stop point:                     ( 20.000000,  9.465185)
Scan average range(m):               382.26
X spot spacing(counts/mm):           25/191.1
Y spot spacing(counts/mm):           25/191.1
Pan angle (degrees):                 0.000000
Tilt angle (degrees):                0.000000
```

```
Tilt angle (degrees):               0.000000

Number of shots:                    1327140
Number of scan lines:               1010
Number of points per line:          1314
Number of loops:                    2
Scan task mode:                     scan
Scan task id:                       133
Pulse mode:                         Last Pulse
Scan pattern:                       Step Stare
Shot type:                          Shot I3D
Scan start position:                Lower Left
Scan orientation:                   Horizontal
Scan in ER mode:                    Yes
Roi id:                             133
Roi start point:                    (-20.000000,-19.460917)
Roi stop point:                     ( 17.639053,  9.465185)
Scan average range(m):               197.60
X spot spacing(counts/mm):           25/98.8
Y spot spacing(counts/mm):           25/98.8
Pan angle (degrees):                 36.000031
Tilt angle (degrees):                0.000000


Applies asc correction:             No
Trims shot Data:                    No (0)
Applies ric correction:             Yes
Smoothes polar shot data:           No
Reduces shot data:                  No
Model-transforms shots:             Yes
Applies pan-tilt correction:        Yes
Removes outliers:                   Yes
Smoothes Cartesian shot points:     No
Moves Cartesian origin:             Yes
Range-dynamically scales intensity: Yes
Scale intensity range(M):           50.0
```

APPENDIX D – Data Processing Codes

D.1   *Point Extraction Code (for Lava Lake Time Series)*

The updated version of this script can be found at: http://sourceforge.net/projects/tlspy/

```
#------------------------------------------------------------------------
------
#
# Copyright (C) 2009 University of New Mexico Board of Regents
#
# Written by Jed Frechette
#
# This file is part of TLSpy.
#
# TLSpy is free software: you can redistribute it and/or modify
# it under the terms of the GNU General Public License as published by
# the Free Software Foundation, either version 3 of the License, or
# (at your option) any later version.
#
# TLSpy is distributed in the hope that it will be useful,
# but WITHOUT ANY WARRANTY; without even the implied warranty of
# MERCHANTABILITY or FITNESS FOR A PARTICULAR PURPOSE.  See the
# GNU General Public License for more details.
#
# You should have received a copy of the GNU General Public License
# along with TLSpy.  If not, see <http://www.gnu.org/licenses/>.
#
#------------------------------------------------------------------------
------


"""Ingest a text file containing continuous scans of a target and split
it into individual images.

Execution is controlled by a configuration file that is specified on
the command line. For an example of the configuration file syntax look
at the file data/optech/looped/lake.cfg provided with TLSpy"""

__author__ = "Jed Frechette <jdfrech@unm.edu>"
__date__ = "Oct 24, 2009"
```

```python
# TLSpy imports
# from tlspy.version import __version__

__version__ = 'laura'

# Standard library imports
import os
from datetime import datetime, timedelta
from glob import glob
from os import mkdir
from os.path import basename, isdir, join, split
from optparse import OptionParser

# Sci imports
from numpy import apply_along_axis, allclose, arange, column_stack,
copy, dot, \                            flipud, fromfile, genfromtxt, ma,
ones_like, repeat

# Other imports
from configobj import ConfigObj

def parse_options():
    """Parse commandline options."""
    parser = OptionParser(usage='%prog CFG_FILE',
                          description=__doc__,
                          version=__version__)
    (opts, args) = parser.parse_args()
    if os.name == 'nt':
        args = glob(args[0])

    if len(args) < 1:
        exit(parser.print_help())
    return args

def parse_config(config_file):
    """Parse configuration file and return ConfigObj dictionary after
proper
    type conversions."""
    config = ConfigObj(config_file)
    working_dir = split(config.filename)[0]
    config['input_file']['data_file'] = join(working_dir,

config['input_file']['data_file'])
    config['input_file']['n_cols'] =
int(config['input_file']['n_cols'])
    config['input_file']['n_rows'] =
int(config['input_file']['n_rows'])
    config['input_file']['n_loops'] =
int(config['input_file']['n_loops'])
    config['input_file']['images_per_group'] =

int(config['input_file']['images_per_group'])
    config['input_file']['start_time'] =

        datetime.strptime(config['input_file']['start_time'],
                          '%Y-%m-%dT%H:%M:%S')
```

```python
    if config['input_file']['end_time'] == 'None':
        config['input_file']['end_time'] = None
    else:
        config['input_file']['end_time'] =

datetime.strptime(config['input_file']['end_time'],
                                '%Y-%m-%dT%H:%M:%S')
    if config['edits']['matrix_file'] == 'None':
        config['edits']['matrix_file'] = None
    else:
        config['edits']['matrix_file'] = join(working_dir,

config['edits']['matrix_file'])
    if config['edits']['huge_translation'] == 'None':
        config['edits']['huge_translation'] = None
    else:
        config['edits']['huge_translation'] = [float(v) for v in

config['edits']['huge_translation']]

    if config['edits']['x_min'] == 'None':
        config['edits']['x_min'] = None
    else:
        config['edits']['x_min'] = float(config['edits']['x_min'])
    if config['edits']['x_max'] == 'None':
        config['edits']['x_max'] = None
    else:
        config['edits']['x_max'] = float(config['edits']['x_max'])

    if config['edits']['y_min'] == 'None':
        config['edits']['y_min'] = None
    else:
        config['edits']['y_min'] = float(config['edits']['y_min'])
    if config['edits']['y_max'] == 'None':
        config['edits']['y_max'] = None
    else:
        config['edits']['y_max'] = float(config['edits']['y_max'])

    if config['edits']['z_min'] == 'None':
        config['edits']['z_min'] = None
    else:
        config['edits']['z_min'] = float(config['edits']['z_min'])
    if config['edits']['z_max'] == 'None':
        config['edits']['z_max'] = None
    else:
        config['edits']['z_max'] = float(config['edits']['z_max'])

    if config['output_files']['output_txt'] == 'None':
        config['output_files']['output_txt'] = None
    else:
        config['output_files']['output_txt'] = join(working_dir,

config['output_files']['output_txt'])

    if config['output_files']['compress'] == 'True':
        config['output_files']['compress'] = True
    else:
```

```python
        config['output_files']['compress'] = False

    if config['output_files']['video_dir'] == 'None':
        config['output_files']['video_dir'] = None
    else:
        config['output_files']['video_dir'] = join(working_dir,
config['output_files']['video_dir'])
        if not isdir(config['output_files']['video_dir']):
            mkdir(config['output_files']['video_dir'])
    return config

def load_data(data_file, file_cfg):
    """Load data file and return as structured array.

    The members of the the array are 'x', 'y', 'z', 'intensity',
'time',
    'image_number', and 'group_number'. The coordinates for points with
x=y=z=0 are        masked."""

    n_shots = file_cfg['n_cols'] * file_cfg['n_rows'] *
file_cfg['n_loops']

    if file_cfg['data_format'] == 'xyzi':
        data = fromfile(data_file, sep=' ')
        n_points = data.size/4
        data = data.reshape(n_points, 4)
        scan = ma.empty(n_points,
                        dtype={'names':('x', 'y', 'z',
                                        'intensity', 'time',
                                        'image_number',
'group_number'),
                               'formats':('float64','float64',
'float64',
                                          'int32', 'object',
                                          'int32', 'int32')})
        if n_points != n_shots:
            raise IOError("The number of points (%s) in %s does not
equal " \
            "the predicted number of shots (%s). It is impossible to
infer " \
            "accurate time-stamps for this data set." % (n_points,
                                                         data_file,
                                                         n_shots))
        else:
            scan['image_number'] = repeat(range(file_cfg['n_loops']),
                                          file_cfg['n_cols'] *
file_cfg['n_rows'])
            scan['group_number'] = repeat(range(file_cfg['n_loops']),
                                          file_cfg['n_cols'] \
                                          * file_cfg['n_rows'] \
                                          *
file_cfg['images_per_group'])
            [:len(scan['x'])]

        scan_time = file_cfg['end_time'] - file_cfg['start_time']
        shot_time = scan_time / n_points
```

```
        time = shot_time * arange(n_points) + file_cfg['start_time']
        s_col = 0
        e_col = file_cfg['n_cols']
        for ll in xrange(file_cfg['n_loops']):
            for rr in xrange(file_cfg['n_rows']):
                if rr % 2 == 1:
                    time[s_col:e_col] = flipud(time[s_col:e_col])
                s_col += file_cfg['n_cols']
                e_col += file_cfg['n_cols']
        scan['time'] = time
        scan['x'] = ma.masked_values(data[:, 0], 0)
        scan['y'] = ma.masked_values(data[:, 1], 0)
        scan['z'] = ma.masked_values(data[:, 2], 0)
        scan['intensity'] = data[:, 3]
    elif file_cfg['data_format'] == 'txyzi':
        data = fromfile(data_file, sep=' ')
        n_points = data.size/5
        data = data.reshape(n_points, 5)
        scan = ma.empty(n_points,
                    dtype={'names':('x', 'y', 'z',
                                    'intensity', 'time',
                                    'image_number',
'group_number'),
                                'formats':('float64','float64',
'float64',
                                    'int32', 'object',
                                    'int32', 'int32')})
        if n_points != n_shots:
            print "WARNING: The number of points (%s) in %s does not
equal " \
            "the predicted number of shots (%s)." % (n_points,
                                                     data_file,
                                                     n_shots)
            scan['image_number'] = repeat(-99,
scan['image_number'].size)
            scan['group_number'] = repeat(-99,
scan['group_number'].size)
        else:
            scan['image_number'] = repeat(range(file_cfg['n_loops']),
                                          file_cfg['n_cols'] *
file_cfg['n_rows'])
            scan['group_number'] = repeat(range(file_cfg['n_loops']),
                                          file_cfg['n_cols'] \
                                          * file_cfg['n_rows'] \
                                          *
file_cfg['images_per_group'])
            [:len(scan['x'])]

        delta_s = data[:, 0] - data[0, 0]
        scan['time'] = [file_cfg['start_time'] + timedelta(0, s) for s
in delta_s]

        scan['x'] = ma.masked_values(data[:, 1], 0)
        scan['y'] = ma.masked_values(data[:, 2], 0)
        scan['z'] = ma.masked_values(data[:, 3], 0)
        scan['intensity'] = data[:, 4]
    else:
```

```python
        exit('Unknown file format: %s.' % file_cfg['data_format'])

    mask = scan['x'].mask & scan['y'].mask & scan['z'].mask
    scan['x'].mask = mask
    scan['y'].mask = mask
    scan['z'].mask = mask

    return scan

def transform_data(scan, matrix_file=None, huge_translation=None):

    """Transform coordinates using 4x4 transform matrix and/or huge
    translation.
    The transform matrix is applied before any huge translation."""

    if matrix_file:
        t_matrix = genfromtxt(matrix_file, skiprows=2)
        coords = column_stack((scan['x'],
                               scan['y'],
                               scan['z'],
                               ones_like(scan['x'])))
        transform = lambda c: dot(t_matrix, c)
        coords = apply_along_axis(transform, 1, coords)

        # Make a copy of the mask so we can reapply later.
        mask = copy(scan.mask)
        scan['x'] = coords[:, 0]
        scan['y'] = coords[:, 1]
        scan['z'] = coords[:, 2]
        scan.mask = mask
    if huge_translation:
        scan['x'] = scan['x'] + huge_translation[0]
        scan['y'] = scan['y'] + huge_translation[1]
        scan['z'] = scan['z'] + huge_translation[2]
    return scan

def clip_data(scan, x_min=None, x_max=None,
                    y_min=None, y_max=None,
                    z_min=None, z_max=None):
    """Clip scan to specified data bounds."""
    if x_min or x_max:
        if x_min:
            scan['x'] = ma.masked_less(scan['x'], x_min)
        if x_max:
            scan['x'] = ma.masked_greater(scan['x'], x_max)

    if y_min or y_max:
        if y_min:
            scan['y'] = ma.masked_less(scan['y'], y_min)
        if y_max:
            scan['y'] = ma.masked_greater(scan['y'], y_max)

    if z_min or z_max:
        if z_min:
            scan['z'] = ma.masked_less(scan['z'], z_min)
        if z_max:
            scan['z'] = ma.masked_greater(scan['z'], z_max)
```

```
        mask = scan['x'].mask | scan['y'].mask | scan['z'].mask
        scan['x'].mask = mask
        scan['y'].mask = mask
        scan['z'].mask = mask
        scan['intensity'].mask = mask

        return scan

def write_txt_file(scan, output_file, compress=False):
    """Write scan to output text file.

    The data is written to a space separated file with the first line
listing
    column names."""
    f_handle = open(output_file, 'wb')
    try:
        f_handle.write('#x y z intensity time image_number
group_number\n')
        #TODO: There is probably a faster way to do this.
        if compress:
            for row in scan.filled(0):
                if not allclose((row['x'], row['y'], row['z']), 0):
                    f_handle.write('%.06f %.06f %.06f %i %s %i %i\n' %
(row['x'],
                                                          row['y'],
                                                          row['z'],

row['intensity'],

row['time'].isoformat(),

row['image_number'],

row['group_number']))
        else:
            for row in scan.filled(0):
                f_handle.write('%.06f %.06f %.06f %i %s %i %i\n' %
(row['x'],
                                                      row['y'],
                                                      row['z'],

row['intensity'],

row['time'].isoformat(),

row['image_number'],

row['group_number']))
    except:
        raise
    finally:
        f_handle.close()
        print 'Saved %s' % output_file

def plot_image_map(image, start_time, end_time, output_file,
                   title='', vmin=None, vmax=None):
```

```python
    """Plot scan image map as 2D array."""

    from matplotlib import pyplot

    fig = pyplot.figure(1, figsize=(6.08, 3.84))
    ax = fig.add_subplot(111)
    ax.set_axis_off()
    img = ax.imshow(image, vmin=vmin, vmax=vmax, cmap=pyplot.cm.Accent)

    ax.set_title(title)
    txt = ax.text(0, -0.05,
                  'Scan start time: %s\n' \
                  'Scan end time: %s' % (start_time.strftime('%Y-%m-
%dT%H:%M:%S'),
                                         end_time.strftime('%Y-%m-
%dT%H:%M:%S')),
                  transform = ax.transAxes,
                  verticalalignment='top')
    cb = fig.colorbar(img)
    cb.set_label('z elevation, m')
    fig.savefig(os.path.join(output_file),
                dpi = 100)
    fig.clear()


def main():
    args = parse_options()

    for config_file in args:

        # Load data
        cfg = parse_config(config_file)
        scan = load_data(cfg['input_file']['data_file'],
                         cfg['input_file'])

        # Transform data
        scan = transform_data(scan,
                              cfg['edits']['matrix_file'],
                              cfg['edits']['huge_translation'])
        scan = clip_data(scan,
                         cfg['edits']['x_min'],
                         cfg['edits']['x_max'],
                         cfg['edits']['y_min'],
                         cfg['edits']['y_max'],
                         cfg['edits']['z_min'],
                         cfg['edits']['z_max'],)

        # Save output data
        n_rows = cfg['input_file']['n_rows']
        n_cols = cfg['input_file']['n_cols']
        scan_size = n_rows * n_cols

        # Write data to text file.
        if cfg['output_files']['output_txt']:
            write_txt_file(scan, cfg['output_files']['output_txt'],
                           cfg['output_files']['compress'])
```

```
        if cfg['output_files']['video_dir']:
            for ni in xrange(cfg['input_file']['n_loops']):
                # Save video frame images.
                img_mask = ma.masked_not_equal(scan['image_number'],
ni).mask
                z = scan['z'][~img_mask]
                time = scan['time'][~img_mask]
                z = z.reshape(n_rows, n_cols)
                if ni % 2 == 0:
                    z = flipud(z)
                plot_image_map(z,
                               start_time=time.compressed()[0],
                               end_time=time.compressed()[-1],

output_file=join(cfg['output_files']['video_dir'],
                                            'frame-%04i.png' % ni),

title=basename(cfg['input_file']['data_file']),
                               vmin=scan['z'].min(),
                               vmax=scan['z'].max())

                if ni % 100 == 0:
                    print 'Saved %s' %
join(cfg['output_files']['video_dir'],
                                            'frame-%04i.png' %
ni)

if __name__ == '__main__':
    main()
```

D.2 Configuration Files for Point Extraction

D.2.1 2009 Lava Lake Scan (Extraction Size = 8x8x6m)

```
[input_file]
# Name = TS09_Point_1_8x8x6
# Input data file.
    data_file = 20091216-lake01-all.xyz
# Format of input text file. Known formats are:
# xyzi: x y z intensity
# txyzi: time x y z intensity
    data_format = txyzi
# Number of rows per scan image.
    n_rows = 177
```

```
# Number of columns per scan image.
      n_cols = 237
# Number of scan images in the scan.
      n_loops = 1000
# The number of scan images per group. Specifying a value other
that 1 allows multiple images to be combined for analysis or
output.
      images_per_group = 2
# Start time of scan in ISO 8601 format: yyyy-mm-ddTHH:MM:SS
# Can be determined from the Optech parsing log.
      start_time = 2009-12-16T12:44:06
# End time of scan in ISO 8601 format: yyyy-mm-ddTHH:MM:SS
# Can be determined from the .bmp screen shoot of the scanner's
LCD.
      end_time = None


# Edits are applied in the following order:
# 1.) Matrix transform
# 2.) Huge translation
# 3.) Clipping.


[edits]
# Apply the 4x4 transformation matrix in the specified file to
all point coordinates. If None is specified no transformation
will be applied.
      matrix_file = None
# Huge translation applied to all point coordinates. Values are
added to the x, y, and z values of all points in the input file.
If the value is None no translation is applied.
      huge_translation = None
# Minimum and maximum values to clip data to. If values are None
no clipping will be performed.


Point A:
      x_min = -40.587978
      x_max = -32.587978
      y_min = -238.180424
      y_max = -230.180424
```

```
            z_min = -227.345911
            z_max = -221.345911



Point B:
            x_min = -47.014325
            x_max = -39.014325
            y_min = -223.469656
            y_max = -215.469656
            z_min = -227.243253
            z_max = -221.243253



[output_files]
# Directory in which video frames should be saved. If the value
is None now frames will be saved.
            video_dir = None
# Output text file that points should be saved to.  If the value
is None no file will be saved. The format of the output file is x
y z intensity time loop_number
            output_txt = 20091216-lake01-ts1-8-out.xyz
# Should ouput txt file be compressed to remove all null data
points. If the value is True all null points will be excluded
from the output file. If set to any other value all null points
will be filled with 0
            compress = True
```

D.2.2   *2010 Lava Lake Scan (Extraction Size = 2x2x12m)*

```
[input_file]
# Input data file.
            data_file = 20101215_lake02_all.xyz
# Format of input text file. Known formats are:
# xyzi: x y z intensity
# txyzi: time x y z intensity
            data_format = txyzi
# Number of rows per scan image.
```

```
      n_rows = 39
# Number of columns per scan image.
      n_cols = 159
# Number of scan images in the scan.
      n_loops = 500
# The number of scan images per group. Specifying a value other
that 1 allows multiple images to be combined for analysis or
output.
      images_per_group = 2
# Start time of scan in ISO 8601 format: yyyy-mm-ddTHH:MM:SS
# Can be determined from the Optech parsing log.
      start_time = 2010-12-15T02:20:08
# End time of scan in ISO 8601 format: yyyy-mm-ddTHH:MM:SS
# Can be determined from the .bmp screen shoot of the scanner's
LCD.
      end_time = None


# Edits are applied in the following order:
# 1.) Matrix transform
# 2.) Huge translation
# 3.) Clipping.

[edits]
# Apply the 4x4 transformation matrix in the specified file to
all point coordinates. If None is specified no transformation
will be applied.
      matrix_file = 20101215_lake02_task101_section1.txt
# Huge translation applied to all point coordinates. Values are
added to the x,y, and z values of all points in the input file.
If the value is None no translation is applied.
      huge_translation = 553043, 1398563, 2781
# Minimum and maximum values to clip data to. If values are None
no clipping will be performed.

Point A:
      x_min = 552193.430679
      x_max = 552195.430679
      y_min = 1393457.252953
```

```
        y_max = 1393459.252953
        z_min = 3482.836119
        z_max = 3494.836119


Point B:
        x_min = 552200.542518
        x_max = 552202.542518
        y_min = 1393472.652736
        y_max = 1393474.652736
        z_min = 3483.331637
        z_max = 3495.331637


Point C:
        x_min = 552204.554543
        x_max = 552206.554543
        y_min = 1393457.204353
        y_max = 1393459.204353
        z_min = 3483.283213
        z_max = 3495.283213


Point D:
        x_min = 552201.780693
        x_max = 552203.780693
        y_min = 1393443.170937
        y_max = 1393445.170937
        z_min = 3483.355635
        z_max = 3495.355635


Point E:
        x_min = 552198.996415
        x_max = 552200.996415
        y_min = 1393457.151691
        y_max = 1393459.151691
        z_min = 3483.250877
        z_max = 3495.250877



[output_files]
```

```
        # Directory in which video frames should be saved. If the value
        is None now frames will be saved.
            video_dir = None
        # Output text file that points should be saved to.  If the value
        is None no file will be saved. The format of the output file is x
        y z intensity time loop_number
            output_txt = 20101215-lake02-2x2A-out.xyz
            output_txt = 20101215-lake02-2x2B-out.xyz
            output_txt = 20101215-lake02-2x2C-out.xyz
            output_txt = 20101215-lake02-2x2D-out.xyz
            output_txt = 20101215-lake02-2x2E-out.xyz
        # Should ouput txt file be compressed to remove all null data
        points. If the value is True all null points will be excluded
        from the output file. If set to any other value all null points
        will be filled with 0
            compress = True
```

D.3   Calculation of Surface Area from a Point Cloud

```
////////////////////////////////////////////////////////////////////////
////////
//
// Point_Cloud_Area
//
// Copyright (C) Nial Peters 2011
//
// This file is part of pyR.
//
// pyR is free software: you can redistribute it and/or modify
// it under the terms of the GNU General Public License as published by
// the Free Software Foundation, either version 3 of the License, or
// (at your option) any later version.
//
// pyR is distributed in the hope that it will be useful,
// but WITHOUT ANY WARRANTY; without even the implied warranty of
// MERCHANTABILITY or FITNESS FOR A PARTICULAR PURPOSE.  See the
// GNU General Public License for more details.
//
// You should have received a copy of the GNU General Public License
// along with pyR.  If not, see <http://www.gnu.org/licenses/>.
//
////////////////////////////////////////////////////////////////////////
////////
////////////////////////////////////////////////////////////////////////
////////
```

```
/*
 * Program to estimate the area of a point cloud. The program works by
 * converting all the points in the cloud to polar coordinates, with
 * the pole situated at the approximate centre of the cloud. It then
 * splits the cloud into segments, each containing a fixed number of
 * points. For each segment it chooses the point which is farthest from
 * the pole and assumes that this is on the boundary of the cloud. The
 * boundary points are used to create a bounding contour, and the area
 * of this is used as the estimate of the cloud area.
 *
 * The number of points per segment must be chosen carefully. Too few,
 * and points in the centre of the cloud will be included in the
 * boundary. Too many, and the boundary will be a poor approximation of
 * the cloud shape. Some trial and error will probably be needed! To
 * help with this, the program will output a file containing the points
 * in the estimated boundary which can be plotted to evaluate the
 * estimate.
 *
 * Associated variables: pyr_error
 *                       pyr_mem
 *
 * Compilation:
 * The program must be linked to the OpenCV and highGUI libraries. On
 * linux the command should be something like:
 *
 * $ gcc lidar.c cpyR/pyr_error.c -o lidar -lcv -lm –
 * I/usr/local/include/opencv - lhighgui
 */

//Edit these macros to change program operation.
//Use forward slashes as path separators (even on Windows!)
#define POINT_CLOUD_FILE "/home/nialp/PhD/Lava Lake Point
Clouds/2010_point_cloud"
#define POINTS_PER_SEGMENT 100
#define BOUNDARY_ESTIMATE_FILE "/home/nialp/boundary_estimate"

////////////////////////////////////////////////////////////////////////
////////
#include<stdio.h>
#include"cv.h"
#include"highgui.h"
#include"cpyR/pyr_mem.h"
#include"cpyR/pyr_error.h"

//struct to hold a polar point
typedef struct PolPt{
    double r;
    double angle;
} PolPt;

//struct to hold a sequence of polar points
typedef struct PolSeq{
    CvSeq *seq;
    CvPoint2D32f pole;
} PolSeq;

//macro for calculating the distance between two CvPoints
```

```c
#define DST_BTW_PTS(a,b) sqrt(((b.x-a.x)*(b.x-a.x))+((b.y-a.y)*(b.y-
a.y)))

//NOTE - not same macro as in stabilization.h, since coordinates are
not reversed.
#define PTS_TO_ANGLE(a,b) atan2((double)(b.y - a.y), (double)(b.x -
a.x))

CvSeq * loadPointCloud(char *filename, CvMemStorage *storage){
        // Function loads a point cloud file into a CV Sequence object.
        // The file should have three columns x,y,z of floating point
        // values in meters. Note that the returned sequence will be
        // in integer numbers of mm.

        FILE *ifp;
        double x,y,z;
        CvSeqWriter writer;
        CvSeq *points;
        CvPoint cur_pt;

        if((ifp = fopen(filename, "r"))==NULL){
                SET_ERR("Failed to open file for reading", IO_ERR);
                return NULL;
        }
        cvStartWriteSeq(CV_SEQ_ELTYPE_POINT, sizeof(CvSeq),
sizeof(CvPoint), storage,                        &writer);
        while(fscanf(ifp,"%lf %lf %lf",&x,&y,&z) == 3){
                cur_pt = cvPoint(1000*x,1000*y); //coordinates in mm
                CV_WRITE_SEQ_ELEM(cur_pt,writer);
        }
        fclose(ifp);
        points = cvEndWriteSeq(&writer);
        return points;

}

int polSortAngle(const void *a, const void *b, void *userdata){
        // Comparator function for sorting a sequence of polar points
        // into angle order.

        if(((PolPt*)a)->angle > ((PolPt*)b)->angle){
                return 1;
        }
        if(((PolPt*)a)->angle < ((PolPt*)b)->angle){
                return -1;
        }
        return 0;

}

int polSortDist(const void *a, const void *b, void *userdata){
        // Comparator function for sorting a sequence of polar points
        // into distance order

        if(((PolPt*)a)->r > ((PolPt*)b)->r){
                return 1;
        }
```

```c
        if(((PolPt*)a)->r < ((PolPt*)b)->r){
              return -1;
        }
        return 0;

}

PolSeq * convertToPolar(CvSeq *points, CvMemStorage *storage){
        // Converts a sequence of Cartesian points into a sequence of
polar points with        // their pole at the approximate centre of the
point cloud. The sequence will       // be sorted by angle.

        CvSeqReader reader;
        CvSeqWriter writer;
        CvPoint2D32f centre;
        CvBox2D bbox;
        int i;
        PolPt cur_pol_pt;
        CvPoint cur_pt;
        PolSeq *pol_seq;

        //find approximate center of point cloud
        bbox = cvFitEllipse2(points);

        centre = bbox.center;

        printf("Centre of point cloud at %0.2lf,%0.2lf (meters)\n",
centre.x/1000.0,                      centre.y/1000.0);

        //convert to a sequence in polar coordinates
        cvStartWriteSeq(0, sizeof(CvSeq), sizeof(PolPt), storage,
&writer);
        cvStartReadSeq(points, &reader,0);

        for(i=0; i<points->total;i++){
              CV_READ_SEQ_ELEM(cur_pt, reader);
              cur_pol_pt.r = DST_BTW_PTS(centre, cur_pt);
              cur_pol_pt.angle = PTS_TO_ANGLE(centre, cur_pt);
              CV_WRITE_SEQ_ELEM(cur_pol_pt,writer);
        }
        MEM_ALLOC(pol_seq, sizeof(PolSeq));
        pol_seq->seq = cvEndWriteSeq(&writer);
        pol_seq->pole = centre;

        //sort the sequence into angle order
        cvSeqSort(pol_seq->seq, polSortAngle, NULL);

        return pol_seq;

}

CvPoint polToCart(PolPt pt, CvPoint2D32f pole){
        // Converts a polar point into a Cartesian point.

        double x,y;

        x = (pt.r * cos(pt.angle)) + pole.x +0.5;
```

```
        y = (pt.r * sin(pt.angle)) + pole.y +0.5;

        return cvPoint((int)x,(int)y);
}

CvSeq * outerEdge(PolSeq *points, int num_pts, CvMemStorage *storage){
        // Estimates the outer boundary of a sequence of points by
splitting the points     // into segments each containing "num_pts"
points and then finding the point   // farthest from the pole in each
segment.

        int pts_per_pt;
        int i;
        CvSeq *current_slice;
        CvMemStorage *temp_storage;
        CvSeq outer_edge;
        CvSeqWriter writer;
        CvPoint cur_pt;
        PolPt cur_pol_pt;
        CvSeq *s;

        temp_storage = cvCreateMemStorage(0);


        pts_per_pt = (int)((points->seq->total / (float)num_pts)+0.5);

        cvStartWriteSeq(CV_SEQ_ELTYPE_POINT | CV_SEQ_KIND_CURVE
,sizeof(CvSeq),                                  sizeof(CvPoint), storage,
&writer);
        for(i=0; i<points->seq->total+pts_per_pt; i+=pts_per_pt){
                current_slice = cvSeqSlice(points->seq, cvSlice(i,
i+pts_per_pt),
temp_storage, 1);
                cvSeqSort(current_slice,polSortDist, NULL);
                cvSeqPop(current_slice,&cur_pol_pt);
                cur_pt = polToCart(cur_pol_pt, points->pole);
                CV_WRITE_SEQ_ELEM(cur_pt, writer);
        }
        cvReleaseMemStorage(&temp_storage);
        s =  cvEndWriteSeq(&writer);
        return cvApproxPoly(s, sizeof(CvContour), storage,
CV_POLY_APPROX_DP,0,0);

}

int main(void){
        CvSeq *seq;
        CvMemStorage *storage;
        PolSeq *pol_seq;
        CvSeqReader reader;
        PolPt pt;
        CvSeq *edge;
        int i;
        CvPoint cur_pt;
        FILE *ofp;

        storage = cvCreateMemStorage(0);
```

```c
        seq = loadPointCloud(POINT_CLOUD_FILE, storage);
        if(seq == NULL){
                printf("%s\n",GET_ERR_MES());
                cvReleaseMemStorage(&storage);
                exit(1);
        }

        printf("Read %d points from point cloud file\n", seq->total);
        pol_seq = convertToPolar(seq, storage);

        edge = outerEdge(pol_seq, POINTS_PER_SEGMENT, storage);

        printf("Edge has %d pts\n", edge->total);

        cvStartReadSeq(edge, &reader,0);
        ofp = fopen(BOUNDARY_ESTIMATE_FILE,"w");

        if(ofp == NULL){
                printf("Unable to open boundary estimate file for
writing.\n");
                cvReleaseMemStorage(&storage);
                free(pol_seq);
                exit(1);
        }

        for(i=0;i<edge->total;i++){
                CV_READ_SEQ_ELEM(cur_pt, reader);
                fprintf(ofp, "%d %d\n",cur_pt.x, cur_pt.y);
         }
         fclose(ofp);
         printf("Boundary estimate written to %s\n",
BOUNDARY_ESTIMATE_FILE);

         printf("Contour area =
%lf\n",cvContourArea(edge,CV_WHOLE_SEQ,0)/1000000.0);

        cvReleaseMemStorage(&storage);
        free(pol_seq);

}
```

```c
////////////////////////////////////////////////////////////////////
////////
//
// pyr_error
//
// Copyright (C) Nial Peters 2011
//
// This file is part of pyR.
//
////////////////////////////////////////////////////////////////////
////////
////////////////////////////////////////////////////////////////////
////////

#ifndef PYR_ERROR_H
#define PYR_ERROR_H

#ifdef PYTHON_BUILD
#include"Python.h"
#endif

#include<stdlib.h>
#include<stdio.h>

#define LOCATION "(%s:%d) ",__FILE__ ,__LINE__

enum pyr_err_type {NO_ERR=0, ERR=1, IO_ERR=2, VALUE_ERR=3, TYPE_ERR=4,
RUN_ERR=5, MEM_ERR=6};

typedef struct Error{
        const char *message;
        enum pyr_err_type type;

} pyr_error_t;

extern pyr_error_t pyr_error;

#define FATAL(s) printf(LOCATION); printf("%s\n",s); exit(1)
#define WARN(s) printf(LOCATION); printf("%s\n",s)

#define RESET_ERR() pyr_error.type=NO_ERR
#define ERR_OCCURRED() ((int)pyr_error.type)

#define SET_ERR(m,t) pyr_error.message=m; pyr_error.type=t

#define GET_ERR_MES() pyr_error.message
#define GET_ERR_TYPE() ((int)pyr_error.type)

#ifdef PYTHON_BUILD
inline PyObject * GET_PYTHON_EXC(void);
#define RAISE_PYTHON_EXC()
PyErr_SetString(GET_PYTHON_EXC(),GET_ERR_MES()); return NULL
#endif //PYTHON_H


#endif //PYR_ERROR_H
```

```
/////////////////////////////////////////////////////////////////////
////////
//
// pyr_mem
//
// Copyright (C) Nial Peters 2011
//
// This file is part of pyR.
//
/////////////////////////////////////////////////////////////////////
////////
/////////////////////////////////////////////////////////////////////
////////


#ifndef PYR_MEM_H_
#define PYR_MEM_H_

#include"pyr_error.h"

#define MEM_ERROR() FATAL("Failed to allocate memory!")

#define MEM_ALLOC(p,s) if((p = malloc(s))==NULL){ MEM_ERROR();}

#endif /* PYR_MEM_H_ */
```

APPENDIX E – Archival of Raw TLS and Time Series Data

The raw TLS point clouds (Level 0 – following NASA's EOSDIS data processing levels) and raw aligned TLS point clouds (Level 1B) have been archived in the Data Coordination Center for the U.S. Antarctic Program (USAP-DCC). The DCC is "funded by the NSF Division of Polar Programs to coordinate the management of data collected by U.S. funded scientists in Antarctica and the Southern Ocean." The data has been logged under NSF Grant #1142083.

The link to access the archived data is:

http://www.usap-data.org/entry/NSF-ANT11-42083

The raw extracted time series data of the lava lake have also been placed onto a CD and attached to this thesis.